Hard coatings on cemented carbide cutting tools: process technology and application

Dipl.-Ing. Martina Gassner

being a thesis in partial fulfillment of the requirements for the degree of a
Doktor der montanistischen Wissenschaften (Dr. mont.)
at the Montanuniversität Leoben

Leoben, October 2018

Financial support by the Austrian Federal Government (in particular from the Bundesministerium für Verkehr, Innovation und Technologie (BMVIT) and the Bundesministerium für Digitalisierung und Wirtschaftsstandort (BMDW)), represented by Österreichische Forschungsförderungsgesellschaft mbH FFG, within the research activities in the project HEC³T (grant number 851894) related to the „Basisprogramm“ is gratefully acknowledged.

Affidavit

I declare in lieu of oath, that I wrote this thesis and performed the associated research myself, using only literature cited in this volume.

Leoben, October 2018

Martina Gassner

Acknowledgments

My sincerest gratitude is due to Prof. Dr. Christian Mitterer for the opportunity to compose this thesis at the Chair for Functional Materials and Materials Systems. I am grateful for his supervision, advice, guidance and patience. *Thank you for letting me be part of your group!*

Also, I would like to express my gratitude to Dr. Christoph Czettl, Dr. Markus Pohler and DI (FH) Christian Storf from CERATIZIT Austria for their support and the fruitful discussions.

Especially I would like to thank my friend and supervisor Dr. Nina Schalk. *Nina, thank you for all your support, patience and friendship!*

I also would like to express my sincerest gratitude to all my colleagues of the "Thin Film Group" for valuable discussions in all matters and cheering me up during one or two entertaining coffee breaks. Thanks to my colleague Dr. Birgit Großmann for accompanying me on the numerous business trips to Reutte. Special thanks go to my office mate Dr. Michael Tkadletz for the pleasurable working atmosphere. *Sharing an office with you was great!*

I would like to thank Bernhard Sartory from the MCL for the support and fruitful discussions and his outstanding work he conducts on the REM-FIB.

I would like to thank my parents for their love and support. *Without you that would never have been possible.*

Last but not least, I would like to thank the most important person in my life my husband Gert. *Thank you for your encouraging me, for giving me the support in all possible ways, the trust you place in me, your endless patience and above all, for your love!*

Content

1. Introduction

Cutting tools coated with thin hard coatings offer protection against wear and oxidation; consequently, they provide the basis for increased tool life and improved cutting performance [1,2]. Today, the majority of cutting tools (> 70 %) are cemented carbide tools and in total more than 50 % are coated cemented carbide tools. The synthesis of these thin hard coatings is either done by chemical vapor deposition (CVD) or physical vapor deposition (PVD with main methods sputtering and cathodic arc evaporation) techniques [1,3]. Here, CVD is dominating with more than half of the coated cemented carbide cutting inserts; about a quarter of the inserts is coated by PVD, and the rest remains uncoated [1,3–5].

Coatings synthesized using CVD or PVD offer high hardness, oxidation and wear resistance, thermal stability, and diffusion barrier properties [6]. The combination of these properties offers the basis for the advances in machining technology achieved during the last decades. The respective demands on cutting inserts for different industrial applications are addressed by tailoring properties of hard coating, cemented carbide substrate and the interface between them. Depending on the chosen deposition technique and the used synthesis conditions, coating structure and properties can be adjusted [6]. Implementation and further improvement of these coating systems allows turning at increased cutting speeds and, consequently, enhanced cutting performance.

For the production of wear resistant cemented carbide cutting tools, good adhesion of the deposited hard coating and, consequently, the prior removal of substrate surface contaminations are essential. Pretreatment by means of ion etching prior to PVD coating offers an in-situ removal of contaminations like surface oxides, modifies the surface and its roughness, and provides the basis for an improved adhesion of the hard coatings [7]. Beyond a suitable pretreatment before coating deposition, also the post-treatment is of major impact on tool performance. Blasting removes the deposition process inherent droplets typical for cathodic arc evaporated coatings. Besides surface smoothing, the impact of blasting material can be used to tailor the stresses within the coating [8]. A frequently used coating system deposited by CVD is TiCN/Al_2O_3, with TiCN is representing the base-layer and Al_2O_3 the top-layer. The deposition by CVD is accompanied by the development of a thermal tensile crack network formed during cooling after coating deposition due to mismatches of the thermal expansion coefficients of cemented carbide and the hard coating layers. The formed cracks offer a pathway for

diffusion of species from the ambience through the coating's bulk, but also from the coating layers and the cemented carbide substrate towards the surface. These diffusion processes foster oxidation of the cemented carbide, but also of the TiCN base-layer at machining conditions [9–11].

Besides considerations about the tool performance, also the resources needed for coating deposition have to be considered for environmental but also commercial reasons. There, a suitable approach is the use of Sankey diagrams, as the respective contributions to the energy and material fluxes needed for the individual process steps can be visualized separately [5,12]. Consequently, for the first time such Sankey diagrams are introduced for CVD and PVD processes within this thesis. As an important step in coating deposition, pretreatment by means of ion etching represents a remarkable contribution to the energy consumed by PVD processes. Within this thesis, the influence of ion etching on substrate roughness and blunting of sharp edges of cutting inserts, dependent on etching time and applied ion energy, was investigated. The findings generated contribute to the understanding of ion bombardment induced changes of surface composition and topography and might be helpful for the optimization of ion etching processes for tools with delicate geometries.

Furthermore, the thermal tensile crack network in TiCN/Al_2O_3 bilayer coatings grown by CVD on cemented carbide inserts was examined in detail. Investigations of coating cross-sections provide a new insight into the crack extension within the coating. In addition, turning experiments with different steels as workpiece materials served to illuminate the tool wear mechanisms.

In summary, the findings reported within this thesis contribute to a better understanding of the process technology needed to deposit hard coatings on cemented carbide cutting inserts and of their application behavior.

2. Deposition techniques

2.1 Physical vapor deposition

Physical vapor deposition (PVD) processes are atomistic deposition processes, where material is vaporized from a solid or liquid source. The mechanisms are evaporation and sputtering, whereby condensed species are transferred to the vapor phase [13]. The vapor-phase material can consist of ions or plasma. The solid materials can either be metals and alloys or compounds like nitrides or oxides. The vapor is transported from the source to the substrate, with or without collisions of the vapor phase species with molecules and atoms of the gas atmosphere, with subsequent condensation on the substrate surface [13–16].

The PVD processes can also be conducted as reactive deposition. This means that a reactive gas (e.g. nitrogen) is injected into the vacuum deposition chamber; together with the evaporated or sputtered material a new compound is formed [16,17]. The big advantage of using PVD is that there is a huge range of potential substrates to be coated, as the substrate temperatures can be varied within a wide range, allowing also the use of temperature sensitive substrates [13,14]. Typical batch sizes for industrial used deposition plants are 2,000 - 10,000 inserts in half inch size. The applied coatings have typical a thickness in the range of ≤ 10 µm [5,8,13,14]. In this section, the PVD techniques sputter deposition and cathodic arc evaporation will be introduced in more detail.

2.1.1 Sputter deposition

In sputter deposition, the solid material, the so called target, is transferred into the vapor phase by bombarding the target surface with energetic ions. Energy and momentum transfer from impinging ions result in direct ejection of surface atoms or the formation of a collision cascade, finally also leading to indirect ejection of surface atoms if the scattered atoms have a higher energy than the surface binding energy, as schematically shown in Fig. 1.

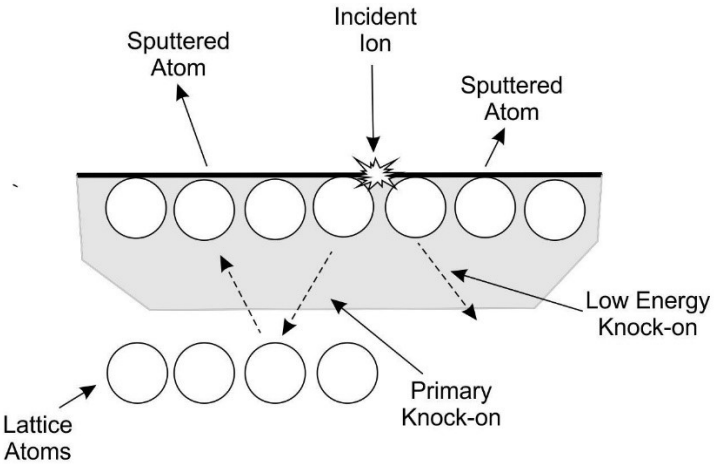

Fig. 1: Illustration of the basic momentum transfer processes during sputtering. Redrawn after [15,18]

A schematic cross-section of a typical magnetron sputter process is shown in Fig. 2.

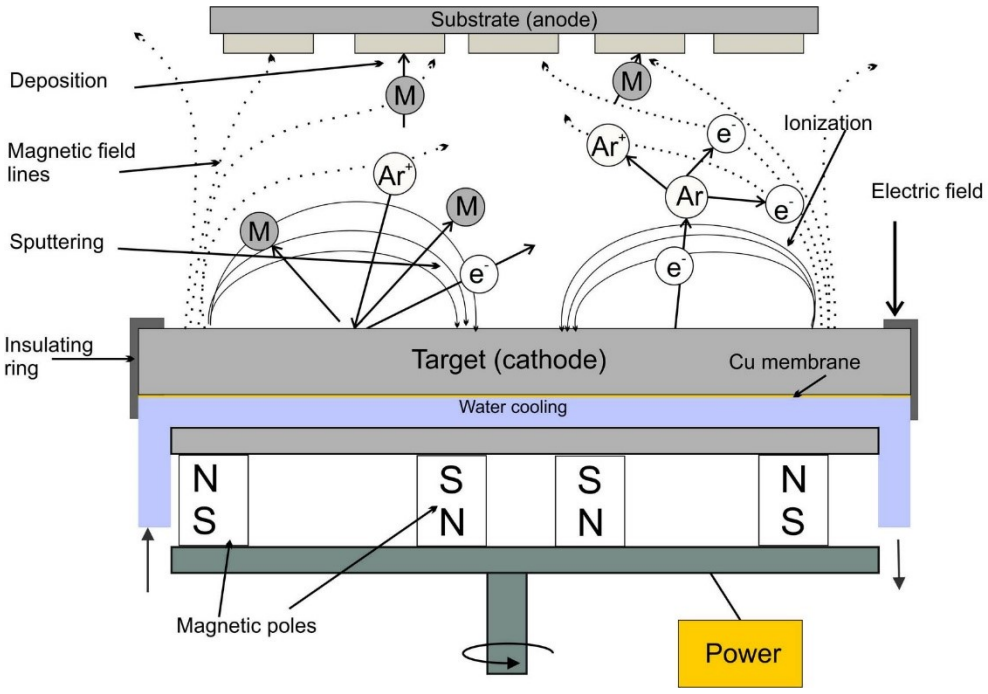

Fig. 2: Schematic illustration of a direct current unbalanced magnetron sputtering system, redrawn after [6].

The used vacuum chamber is typically evacuated to a base pressure of ≤ 10^{-3} Pa. During the sputter deposition process, a voltage between the target (cathode) and the substrate holder (anode) is applied, after an inert working gas (e.g. Ar) is introduced into the vacuum chamber. The creation of the so called plasma is done by the ionization of a working gas by igniting a glow discharge. Having a

planar magnetron, the magnetic fields confine the plasma above the cathode in angular rings, producing the typical erosion profile found on the target [13,15,16].

The sputter deposition process allows to deposit almost any complex composition of materials onto any type of substrate; also electrically nonconductive materials can be deposited and ceramic substrates can be coated by applying a radio frequency (RF) discharge. If not required, the direct current (DC), or pulsed DC sputter mode is preferred for industrial applications due to economic reasons [13]. Oxide and nitride films are often deposited using reactive sputtering. Here a reactive gas, e.g. oxygen or nitrogen, is introduced with the inert gas, e.g. Ar, into the deposition camber. The reactive gas undergoes reactions with the sputtered target material and allows the deposition of a film with composition different from the target material. The disadvantage of the reactive sputtering technique is the so called poisoning of the target, which means that the sputter yield is decreased because of compound formation on the target surface (e.g. formation of a nitride when sputtering in a combined Ar and N_2 atmosphere). The sputter yield is given by the number of sputter-ejected atoms per incident ion. It depends on the target species, the bombarding species, their kinetic energy and their angle of incidence. The target temperature has also an influence on the sputter yield [16].

By employing permanent magnetic fields, the ionization efficiency near the target can be significantly increased. This technique is called magnetron sputter deposition (MSD). MSD can be divided into unbalanced and balanced MSD, depending on the field lines looping between the central and outer magnets. Advanced deposition system are usually unbalanced MSD systems, where the field lines are opened partially and the plasma expands away from the target area towards the substrate, resulting in a higher ionization efficiency and dense plasma also towards the substrate [19]. One advantage of sputter deposition in contrast to cathodic arc evaporation is that a smooth film is obtained. However, the ionization rate is with values below 1 % considerably lower than for cathodic arc evaporation. One approach to enhance the ionization rate is the application of pulses in the megawatt and microsecond range, i.e. the so-called *high power impulse magnetron sputtering* (HiPIMS) or *high power pulsed magnetron sputtering* (HPPMS) technique. This technique enables reaching a higher charge state of target ions and significantly higher ionization rates up to 30 % [6,14].

2.1.2 Cathodic arc evaporation

In cathodic arc evaporation (CAE), the evaporation of the target material is realized using a high current, low voltage electrical discharge, the so-called arc. It is ignited between the anode, typically the grounded chamber wall, and the cathode (target) to be evaporated [20]. Arc discharges occur at low voltages in a range from 20 to 100 V and high currents in the range from 30 A to some kA. The initiation of the arc takes place by a short contact of a metal trigger finger (mechanical igniter) at the cathode. The point of high current density, with typical size of 10^{-8} to 10^{-4} m, where the arc meets the target, is called cathode spot. At this point the surface temperature rises quickly, resulting in an explosive evaporation of target material. A typical setup of a CAE system is schematically illustrated in Fig. 3a. Depending on the material, ionization rates of up to 100 % are possible. At the cathode spot the plasma is generated, which contains a great quantity of ions of the cathode material [6,20,21].

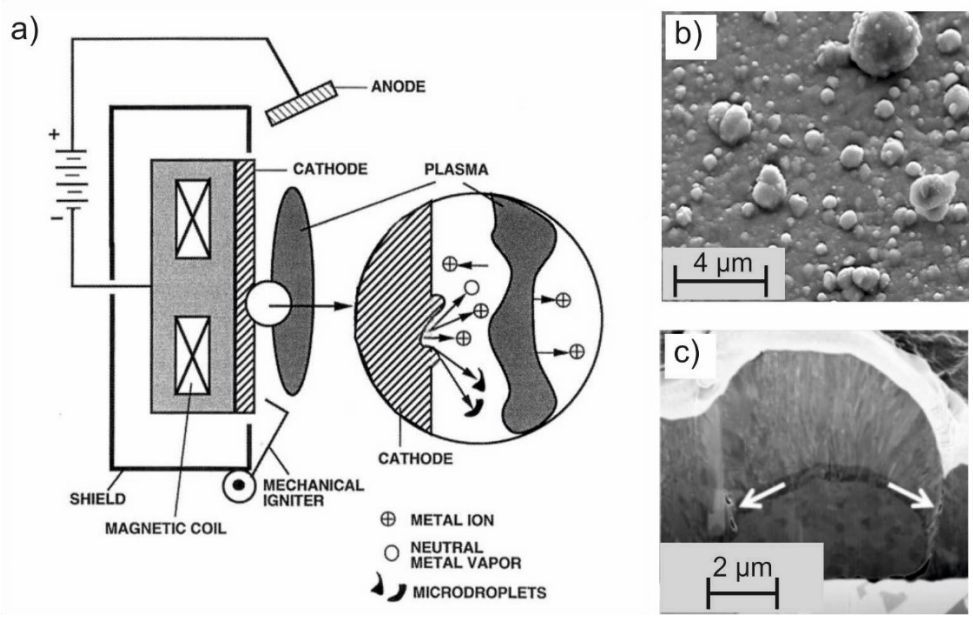

Fig. 3: a) Schematic illustration (cross-section) of a cathodic arc evaporation system including a magnification of the cathode spot [22]*. Secondary electron SEM micrograph of: b) the surface of a TiAlTaN coated cutting insert [own work] and c) a FIB cross-section of a droplet* [23]*.*

A drawback of cathodic arc evaporation is the production of maroparticles, the so called “droplets” consisting of molten target material from the cathode spot. Such droplets are incorporated as defects in the deposited films. Fig. 3b shows a scanning electron microscope (SEM) micrograph of a CAE TiAlTaN coated cutting insert near the cutting edge. There, numerus droplets with different sizes on

the coating surface can be observed. Droplets disturb film growth, since they on the one hand offer renucleation sites and on the other hand they lead to voids beneath the droplets. Such voids act as pathways for diffusion and provide mechanically weak spots [24]. Droplets are also of major impact on the surface roughness of the deposited film, as evidenced in Fig. 3b and c. The focused ion beam (FIB) prepared cross-section of a CAE deposited hard coating shows in SEM micrograph in Fig. 3c clearly how growth is affected by the presence of a droplet [24]. One approach to improve the surface quality is the use of macroparticle filters to separate particles from the cathodic arc plasma stream [21] using curved magnetic filters.

2.1.3 Pretreatment – ion etching

Ion etching has become a standard for substrate cleaning in addition to previous chemical (e.g. etchants) or mechanical (e.g. polishing) pretreatments, for the removal of contaminations, e.g. surface oxides, from substrates. Nowadays pretreatment by ion etching is implemented into PVD systems, since a clean surface is required to achieve the required film properties and especially a good coating adhesion [7,25]. This has proofed necessary, e.g. for wear-resistant coatings for cutting tools, as evidenced by the reported correlation between tool life and microchemistry of the interface [26,27]. As ion etching is done *in situ* immediately prior to deposition within the vacuum chamber, a further contamination after cleaning can be excluded provided that a sufficiently low level of residual gases within the vacuum chamber is used [13]. For the deposition on cemented carbide substrates, two different approaches are commonly applied: inert gas ion etching (e.g. Ar ions) and metal ion etching (e.g. Cr ions) [15,28]. The bombardment with energetic ions leads to changes in surface chemistry, topography, microstructure and morphology of the substrate material. Further formation of defects in the surface near zone of the substrate, substrate heating, desorption of volatile species and implantation of energetic ions has been reported. The implantation of Ar or Cr ions leads to undesired impurities within the surface near zone of the substrate [27]. For multi-component materials, preferential sputtering may result in changes of surface composition and topography [13,15,25]. This effect is caused by different sputter yields of the different components of the substrate [15]. Also the angle of incidence has a remarkable impact on cone formation on the substrate, caused by low yield sputtering material covering material which is eroded at higher rates, but this effect could also be minimized through sample rotation using substrate carousels in industrial deposition plants. Besides the mentioned criteria also the bias voltage is of remarkable impact for the

ion etching pretreatment. As reported by Schönjahn *et al*. [27], Ar ion etching at high substrate bias voltage results in a low density interface region, leading to competitive growth of the coating with a small column width. Since randomly oriented grains nucleate, fibrous columns separated by open grain boundaries are formed, which leads to reduced hardness of the coating and thus inferior tool performance and tool life [13,27]. Cr ion etching at high bias voltages has been reported to provide a clean substrate surface, where implantation of Cr can lead to local epitaxial growth [27]. Also the exposure times to energetic ions are of major impact as local substrate overheating may occur, especially using metal ion etching on small tools, where the tool geometry has also to be considered [26]. The crucial region for cutting inserts are their cutting edges, where during etching and coating deposition the ion flux is concentrated due to electrical field effects, compared to a flat surface [29]. The second publication of this thesis concentrates on Ar ion etching of cemented carbide cutting inserts. The focus was set on different etching times and substrate bias voltages, as well as the influence of etching on modifications of sharp edges of the cutting inserts.

2.2 Chemical vapor deposition

Chemical vapor deposition (CVD) is usually activated thermally, e.g. by high temperatures or by laser-assistance, however a kinetic activation by plasmas in plasma-assisted CVD is also possible. Gaseous precursors (e.g. N_2, Cl_2) are introduced into the deposition reactor, where the coating is deposited from the precursor mixture applied at elevated temperatures [30]. The precursors can be initially solid, liquid or gaseous. Solid precursors like Al, Zr or Ti have to be primarily evaporated to be transported into the reaction chamber; this can be achieved e.g. by chlorination. Fig. 4 illustrates the main steps of a CVD process.

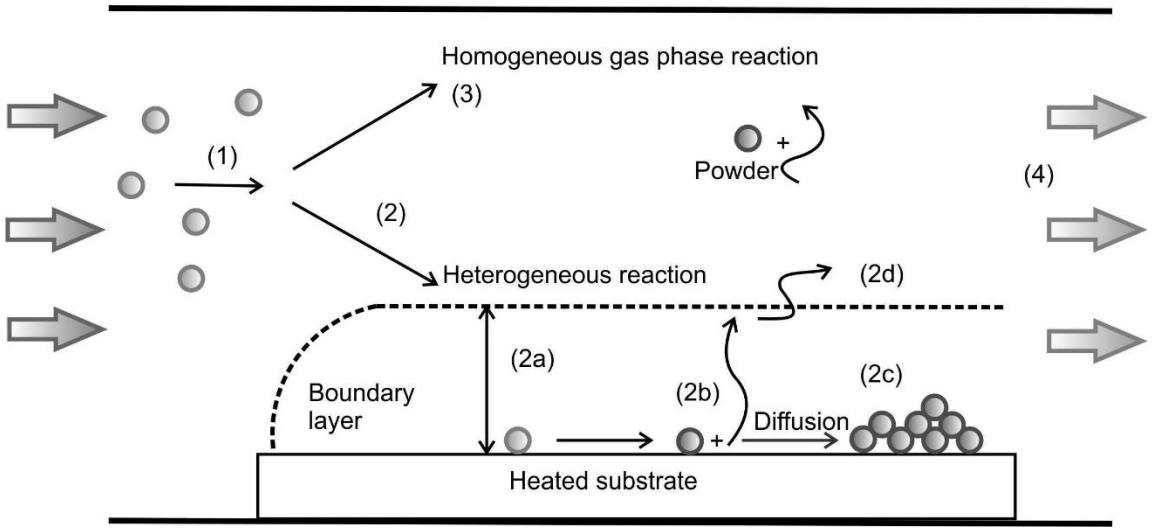

Fig. 4: Schematic illustration of the basic process steps within CVD: (1) gas feed; (2) heterogeneous reaction, (3) homogeneous reaction, (4) gas exhaust. The heterogeneous reaction can be divided into the following steps: (2 a) Transport of the reactants through the boundary layer and adsorption, (2 b) chemical reactions at the substrate surface, (2 c) nucleation and growth, (2 d) desorption of by-products and diffusion through the boundary layer. Redrawn after [6,31].

For example for the deposition of TiCN coatings, $TiCl_4$ which is a liquid at room temperature is used. Synthesis of TiCN with methane is carried out at temperatures of about 1,000 °C.

$$TiCl_4 + xCH_4 + ½(1-x)\ N_2 + 2(1-x)\ H_2 \rightarrow TiC_xN_{1-x} + 4\ HCl$$

Alternately to chlorination, metal-organic compounds can be used [30]. Metal-organic compounds are in most cases less stable precursor materials, which react at lower temperatures. Nowadays, many CVD coatings are synthesized by application of alternative precursor materials. Using CH_3CN instead of CH_4 enables deposition of TiCN at lower temperatures (the so-called moderate-temperature CVD (MT-CVD) process), which prevents formation of the brittle η-phase in cemented carbide substrates [32,33].

$$y\ TiCl_4 + 2\ CH_3CN + 9\ H_2 \rightarrow y\ TiC_xN_{1-x} + 2y(x-0.5)\ CH_4 + 4y\ HCl$$

CVD processes can be classified in *(i)* hot-wall CVD, where the reactor wall is heated and the substrate is placed into a heated furnace for indirect heating, here the reactor wall is also coated, and *(ii)* cold-wall CVD, where only the substrate is heated (either inductively or resistively). The coatings investigated within this thesis were deposited using a hot-wall reactor to reach the necessary deposition temperatures of 700 up to about 1,100 °C. Beside the heating, also the deposition pressure

is of major impact, since it affects also the internal gas stream velocities and as a consequence the dwell time of the components and the diffusion of the reactants to the substrate surface [30,31]. In low pressure CVD (LPCVD), the boundary layer thickness, defined as the region in which the flow velocity changes from zero at the wall to essentially that of the bulk gas away from the wall, decreases due to increased gas velocities and decreasing molecular density, which results in a faster diffusion of reactants and by-products. In general, diffusion rates respond to Arrhenius law, with increased diffusion for increased temperature [30].

In contrast to PVD, CVD has the ability to coat substrate regions, which are not in the line-of-sight, and consequently also irregularly shaped substrates caused by the high so-called throwing power. Further, CVD offers the possibility to achieve high coating thicknesses in the range of 10 to 20 µm and coat great quantities of substrates (e.g. 15,000 half inch inserts) within a single deposition run [5,15,23,34,35].

2.3 Thin film growth

Growth of thin films by PVD or CVD methods, where material transferred from the vapor phase condensates on a substrate, can be summarized by three steps. First, incident atoms impinge on the substrate surface, they are either reflected or, if they lose enough energy to the substrate lattice, they become loosely bonded “adatoms”. Second, the adatoms diffuse over the surface and exchange energy with the lattice and other atoms or molecules, until they are either desorbed or trapped at low energy sites. In the third step of film growth, incorporated atoms readjust their positions within the lattice by bulk diffusion. This process strongly depends on the applied conditions, e.g. the substrate temperature or the pressure during deposition. Surface roughness and defects in the surface near zone of the substrate are of major impact on film growth, since nuclei are preferably formed on lattice defects, atomic steps or scratches in the surface [13,15,17,18].

Subsequent film formation proceeds in three basic growth modes as illustrated in Fig. 5: *(i)* island or Volmer-Weber growth, *(ii)* layer by layer or Frank-Van der Merve growth and *(iii)* mixed layer-island growth or Stransky-Krastanov growth. Island growth occurs when the smallest stable clusters nucleate on the substrate and grow in three dimensions to form islands. This happens when atoms or molecules are more strongly bound to each other than to the substrate. This is in contrast to layer by layer growth, where the smallest stable nucleus expands in two dimensions, resulting in the formation of planar sheets. In this growth mode, the atoms are more strongly bound to the substrate than to

each other. The first complete monolayer is then covered with a rather less tightly bound second layer. The layer plus island growth is a combination of the preceding two modes. In this case, after forming one or more monolayers, subsequent layer growth becomes unfavorable and islands form. Film growth by the layer plus island mode has been observed in metal-metal and metal-semiconductor systems [22]. Hard coatings, as investigated within this thesis, usually grow in the island mode [6,36].

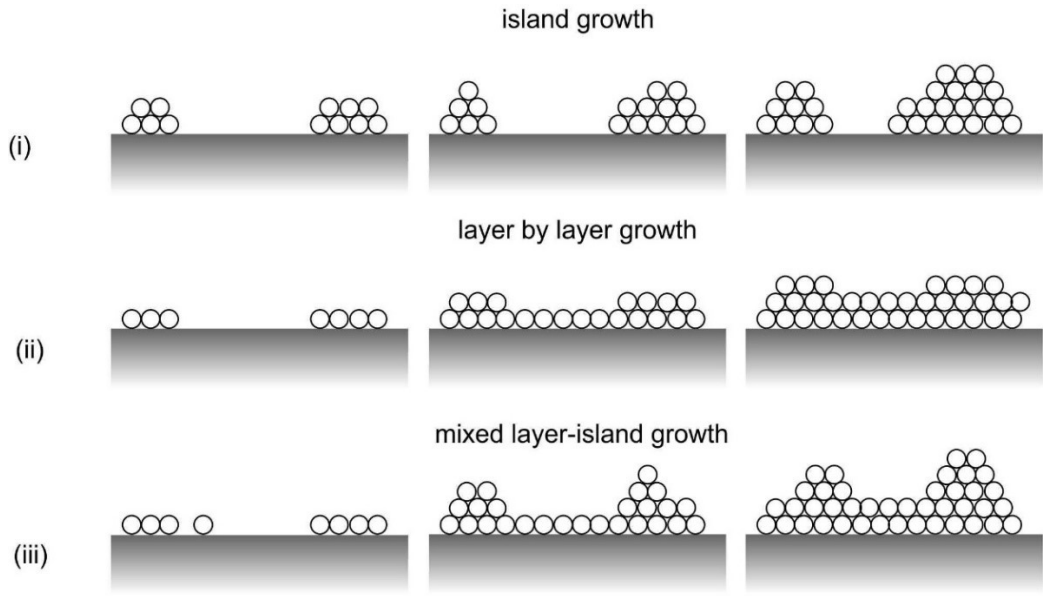

Fig. 5: Thin film growth modes: (i) island, (ii) layer by layer and (iii) mixed layer-island growth, redrawn after [22].

Film growth depends on both nucleation and growth kinetics, determining the coating structure. Structure zone models (SZM) have been developed in the last decades, providing a link between the observed structure and growth parameters. Movchan and Demchishin were the first to introduce a SZM for thermally evaporated films, relating the observed structures to the homologous temperature (i.e. substrate temperature (T_s) divided by the melting temperature (T_m)). Their model distinguishes between three different zones. In zone 1, for metals at temperatures below 0.3 × T_m, the mobility of condensing atoms is very low, resulting in porous columnar structures caused by shadowing effects. Film deposition in zone 2, ranging from temperatures from 0.3 to 0.45 × T_m, is governed by surface diffusion processes. Such films exhibit a smooth surface and a columnar dense structure. Zone 3, 0.45 to 0.50 × T_m, exhibits a recrystallized structure, developed by bulk diffusion [6,15,37].

An extended model was proposed by Thornton [15]; by including the partial pressure of the inert working gas, the original model became suitable also for sputtered coatings. A fourth zone, the so-called transition zone T, which is formed between the zone 1 and 2, was introduced. In zone T, the surface diffusion is more pronounced and competitive growth develops, characterized by a dense and fibrous structure and a continuous change in morphology, texture, and surface topography as a function of film thickness [6,15,38,39]. Further extension of this model was made by Messier *et al.* by including the substrate bias potential instead of the applied partial pressure [40]. In 2010, Anders proposed an extended SZM, illustrated in Fig. 5a, still based on the original three zones and the transition zone T, changing the homologous temperature T_s/T_m into the generalized temperature T*. T* (see Fig. 6, y-axes), which includes the homologous temperature plus a temperature shift caused by the potential energy of particles arriving on the surface [41]. Instead of the partial pressure, the kinetic energy E* (energy flux associated with arriving particles) and the net film thickness t* was introduced. E* describes the displacement and heating effects due to the kinetic energy of bombarding particles. The net film thickness t* is shown on a third axis and enables also to visualize the thickness reduction by sputtering or densification; it also allows to include a negative film thickness, stemming from a higher erosion rate due to ion etching than film growth rate [42].

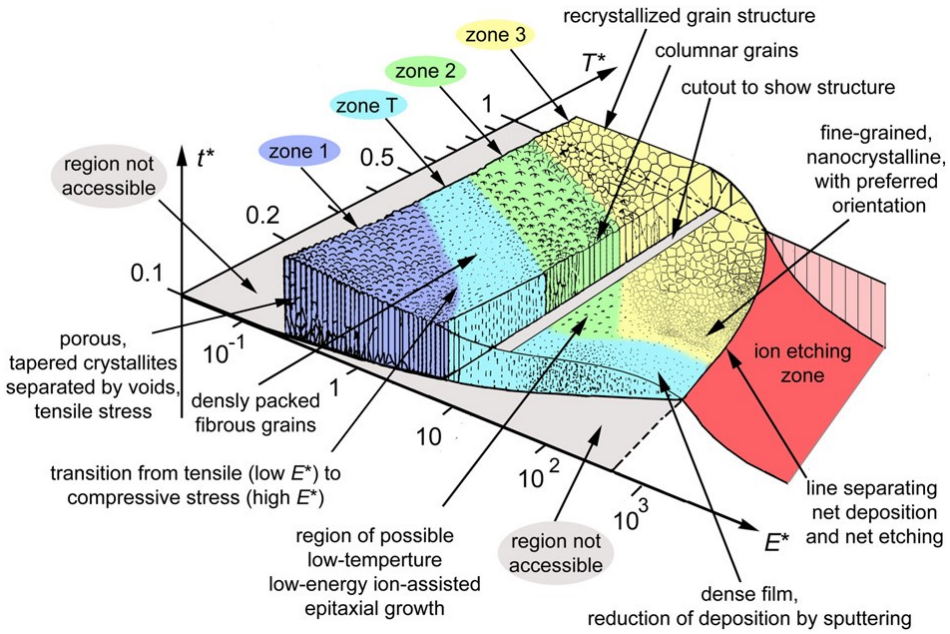

Fig. 6: Structure zone model applicable to energetic deposition introduced by Anders [42].

The structure of a CVD film can be classified in three major types, which are shown schematically in Fig. 7 [30]. In zone 1, the film structure consists of columnar grains, which are capped by a domelike top. This structure is a result of film growth at high temperatures; additionally higher film thicknesses aggravate this effect. To exemplify, the grain size increases and the columnar grains become more pronounced with increasing film thickness. In zone 2, the structure is also columnar but more faceted and angular. In zone 3, the film consists of fine equiaxed grains. Fine-grained structures can be obtained at low temperature, high supersaturation of the vapor phase and at low pressures, i.e. at conditions where diffusion processes are minimized [30].

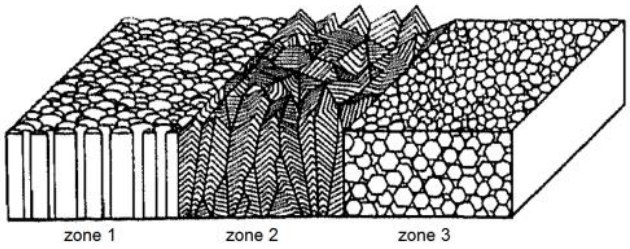

Fig. 7: Three zone model for hard coatings grown via CVD, after Pierson [30].

2.4 Mass and energy balance of deposition processes

The first appearance of flow charts – in a very similar way to the later introduced Sankey diagrams – was noticed on a map of Napoleon's disastrous Russian campaign 1812 – 1813 stated by Charles Minard (1869). Within the field of process engineering, Sankey suggested a diagram (see Fig. 8) to illustrate the efficiency of steam engines in 1898; his approach illustrates the energy flow by arranging arrows standing for the contributions within the process [43,44]. There, the flow of heat is represented as a stream, the width shows the amount of heat fed into the system and leaving it again per unit of time. The heat losses are indicated by the branches. Consequently, the useful energy, in this case the mechanically performed work, is shown graphically in comparison with the original input. The figures are given in absolute quantities. Furthermore, the representation shows the processes involved, here the boiler and the engine [45].

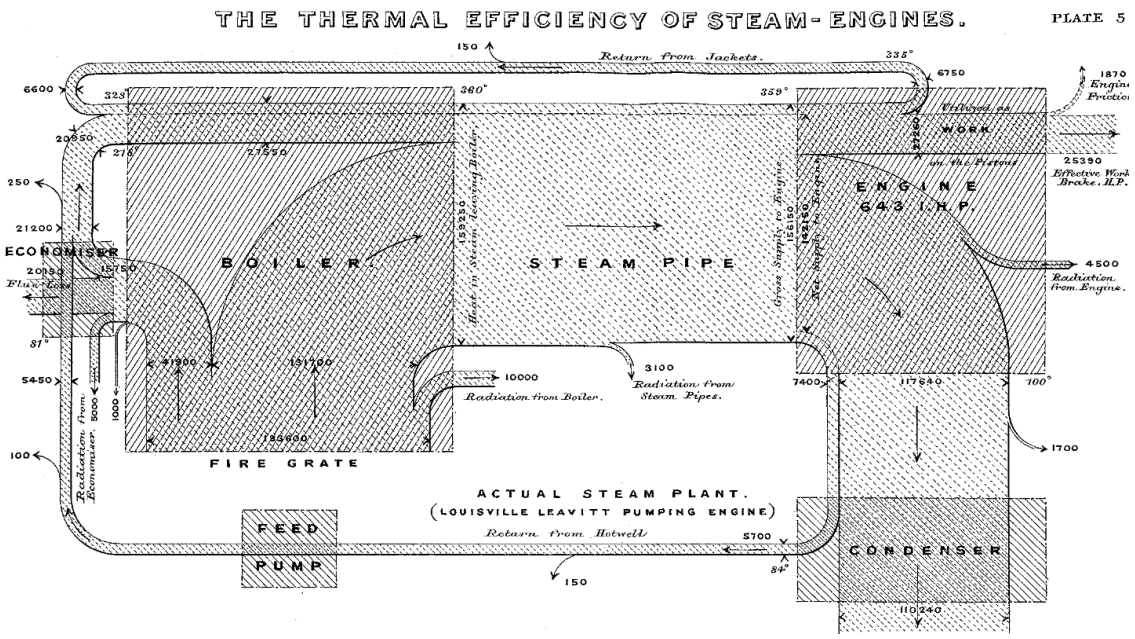

Fig. 8: Flow diagram according to Sankey (1898), visualizing the thermal efficiency of steam engines [43].

Visualization by using Sankey diagrams has the big advantage that the data is normalized and so the quantity of all flows can be summed up; consequently, the respective arrow width corresponds to the total flow within a defined system. With help of the direction of the drawn arrows and branches it can be seen easily if the flow is an incoming flow or leaves the system and also the intensity of the individual flow can be recognized. At the beginning of the 1900s, Riedler used Sankey diagrams to compare the efficiency of diesel and gas engines [46]. Actually, they are used in very different fields like the energy efficiency of cars, monitoring biomass streams [47], or the global hydrogen supply and demand [48], but the possibilities for using Sankey diagrams are nearly unlimited. Today, Sankey diagrams offer the possibility for identifying inefficiencies and potential for savings when dealing with resources.

Hard coatings for cemented carbide inserts are nowadays manufactured by various deposition techniques, in particular PVD and CVD, see sections 2.1 and 2.2. However, these deposition techniques are often used for different coating systems and substrates. Also their energy consumption and mass balance varies, because of the different deposition conditions, throughput, and typically applied coating thicknesses. Considering the input of raw material and the potential of saving energy, Sankey diagrams could be a valuable tool to identify the energy and mass consuming

process steps during a deposition run. Thus, the aim of publication 1 was to introduce the concept of Sankey diagrams for the evaluation of thin film deposition processes.

2.5 Post-treatment

Depending on the deposition process, post-treatment has to be applied to obtain a higher reliability in the cutting operation and an enlarged field of applications. While thermal post-treatments are used to improve microstructure, mechanical post-treatments smoothen the surface and modify residual stresses [11,34,49]. As mechanical post-treatment, wet- or dry blasting are state of the art. While in case of CVD coated cutting tools, the blasting process is applied to reduce surface roughness and residual tensile stresses, in case of PVD droplets stemming from the cathodic arc deposition process are removed [8,34,49–51]. An often used blasting medium is corundum, but also metallic blasting materials are applied. Metal-blasting media, e.g. AlSi, influence the wear behavior through their transfer to the blasted cutting insert [52]. Beside composition, particle size, angle of incidence and blasting pressure, also the shape of the blasting media affect the surface of the blasted tool. Investigations of TiCN/Al_2O_3 coated cemented carbide cutting inserts with respect to the blasting pressure using globular and edged blasting material evidence that the friction behavior and the thermal stress relaxation of the coated insert differ [11,49]. The introduced compressive stresses could be modified by the choice of the shape of the blasting media [49]. Besides the shape and the composition, also the grain size and the blasting pressure is of major impact on the cutting performance. Selecting the appropriate blasting parameters is important since micro-blasting - here a small nozzle diameter between 0.25 and 1.5 mm is used - could also lead to a local coating thickness reduction. The effect is more pronounced for the cutting edge radius and the cutting wedge as stated by Bouzakis *et al.* [53,54]. The inserts examined within this work (paper 3 and 4) were post-treated by wet-blasting using an Al_2O_3 slurry.

3. Hard coatings

3.1 TiN

The first TiN coatings were deposited by CVD in the 1970s and later in the 1980s by means of PVD, representing the first coating material applied for the reduction of tool wear. TiN coatings have a face-centered cubic (fcc) B1 rocksalt (NaCl) structure, see Fig. 9. The main reasons for the excessive use of TiN coatings for cutting applications in the these early years are their good thermal stability and better resistance to crater wear compared to the at that time, also commonly applied TiC. However, TiN coatings suffer from oxidation in ambient air already at temperatures above 550 °C by forming a porous rutile-type TiO_2 scale. Nevertheless, TiN-coated cemented carbide turning tools exhibit an up to eight times increased tool lifetime compared to TiC and uncoated WC, due to the reduced solubility of TiN in iron at elevated temperature. Because of the golden to brownish color, TiN is also used as decorative coating since the 1970s, e.g. for the production of watches often in combination with a very thin top layer of gold [13,17,18,55,56]. The exact color of the coating depends on its stoichiometry [1]. Overstoichiometric TiN with an excess of nitrogen is bronze to brown, while substoichiometric TiN is brightly yellow colored [57]. In addition, TiN is of major importance as base layer below e.g. $TiCN/Al_2O_3$ or TiB_2 coatings on cemented carbide cutting tools to prevent diffusion of carbon. Further, TiN is applied as diffusion barrier in microelectronics [58–60]. Within this work, TiN deposited via sputter deposition was used for the visualization of the material flux and energy consumption by Sankey diagrams (paper 1).

3.2 TiAlN

Due to the ever inreasing industrial demand for higher machining speeds and higher feed rates in combination with longer service times of the tools, TiN coatings have been widely replaced by $Ti_{1-x}Al_xN$ based coatings in cutting applications. $Ti_{1-x}Al_xN$ based coatings exhibit outstanding mechanical properties at room and at elevated temperatures; further, $Ti_{1-x}Al_xN$ has an improved oxidation resistance, with an initiation temperature of approximately 700 °C [55]. They are currently mainly deposited by PVD methods. Deposition using CVD is still very challenging, although there have been several approaches introduced within the last years [61]. The stable form of AlN is the hexagonal wurtzite structure [62–64]. Since PVD of $Ti_{1-x}Al_xN$ yields a thermodynamically non-equilibrium

material, the compositional range is basically unlimited and enables synthesis of metastable solid solutions [62,65]. These metastable $Ti_{1-x}Al_xN$ solid solutions are formed by the substitution of Ti atoms by Al atoms in the fcc-TiN lattice [66]. Metastabile fcc-$Ti_{1-x}Al_xN$ is formed up to x values of about 0.65 to 0.75 (Fig. 9). Within this regime, alloying of Al to the TiN system leads to enhanced mechanical and tribological properties such as hardness and wear resistance. The formation of a stable Al_2O_3 layer at temperatures above 600 °C at the surface remarkably increases the oxidation and wear resistance by reducing the diffusion and the adhesion wear. For films with an x value in the range of 0.60 – 0.70, the oxidation temperature can even be shifted up to 950 °C [63,67,68]. At even higher x values, the formation of a wurtzite (w) structure results in decreasing hardness and wear resistance [24,67–70].

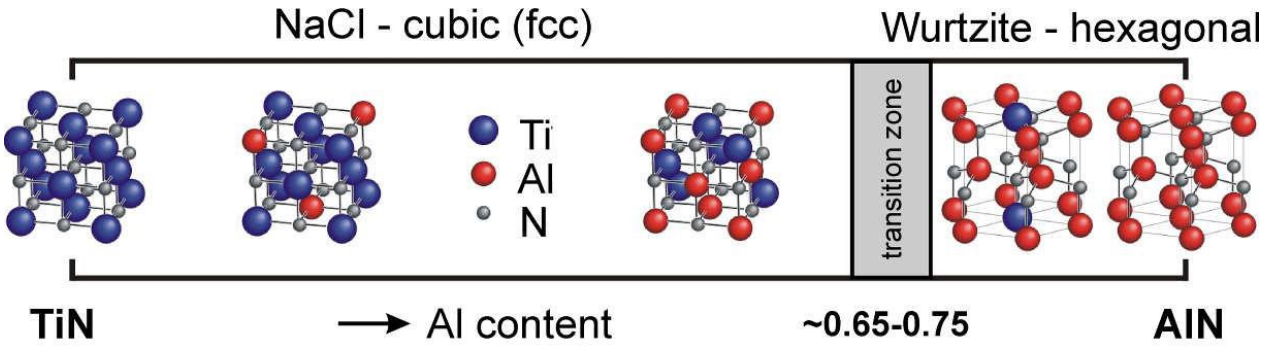

Fig. 9: Structural development of $Ti_{1-x}Al_xN$ with increasing Al content after [71]*, redrawn by* [72]*.*

Decomposition of the metastable $Ti_{1-x}Al_xN$ solid solution into fcc-TiN and fcc-AlN domains takes place at elevated temperatures (≥ 800 °C). Spinodal decomposition is accompanied by the phenomenon of age hardening, as a result of coherency strains between the matrix and the small coherent domains which are formed during annealing. Going to higher temperatures (≥ 950 °C), transformation of the metastable fcc-AlN into the stable w-AlN takes place, resulting in a hardness loss [24,70,73,74].

Besides the variation of the Al content, alloying of transition metals as additional components has been investigated in the last years [75]. Potential transition-metal-nitride candidates for alloying, considering their relative lattice mismatch with respect to a fcc-$Ti_{1-x}Al_xN$ reference and the desired properties, are Hf, Nb and Ta [76]. Alloying with Ta results in increased hardness at room temperature. Already small additions of Ta result in significantly improved oxidation protection [76] and enhanced tribological behavior. Recently, it was reported that an increasing Ta content enhances the thermal

stability of the fcc solid solution by shifting the spinodal decomposition to higher temperatures, thus maintaining the initial high coating hardness up to 1,000 °C [77]. Due to the positive effect of Ta, TiAlTaN coatings are nowadays applied for cutting applications. TiAlN deposited using cathodic arc evaporation was used for paper 2 of this thesis, where it served as model coating system to study the influence of ion etching and subsequent coating deposition on blunting of sharp-edged cutting inserts.

3.3 TiCN

TiCN coatings have been used in the cutting tool industry since the 1970s, providing an improved flank wear resistance – i.e. resistance to abrasion - compared to TiN, due to its higher hardness. TiCN coatings are synthesized by PVD as well as by CVD [78–80]. TiCN forms a single-phase fcc solid solution. Using PVD, depending on the growth conditions, $TiC_{1-x}N_x$ can be synthesized in a broad compositional range (x from 0 to 1). The commonly good adhesion and toughness of TiN compensates for the brittleness of TiC, while the latter provides for the required hardness. TiCN coatings have also a good chemical resistance [78,81,82]. Most commercial coatings do not consist of a single layer of TiCN with a fixed composition, but show a gradient of the composition from the interface to the coating surface. Clearly, there is considerable scope for varying the properties of the coating by changing its composition in this manner [81]. While for PVD coatings a dense and fine-columnar morphology is reported, MT-CVD TiCN coatings have a coarse columnar structure, with columns perpendicular to the substrate surface and typically, a carbon to nitrogen atomic ratio of 0.5 - 0.7 [33,83]. In the past, TiCN as well as TiN and TiC were grown at high temperatures of 950 – 1,050 °C via CVD, resulting in decarburizing of the cemented carbide substrate, which leads to the undesired and brittle η-phase at the substrate/coating interface [6,32,84]. In the MT-CVD process at 800 – 900 °C, CH_3CN and $TiCl_4$ are used as precursor materials instead of CH_4, N_2 and $TiCl_4$, (see section 2.2), where higher temperatures are needed to break the C-H bonds of CH_4. Due to the reduced temperature, decarburization can almost be avoided [32,33,85]. TiCN is commonly used as base-layer for the further deposition of alumina coatings, where it provides the necessary mechanical support and toughness. For papers 1, 3 and 4, TiCN deposited via CVD was used as base-layer for the deposition of α-Al_2O_3 coatings. In addition, TiCN deposited via PVD served as one of the case studies for the visualization of energy consumption and mass flux in paper 1.

3.4 Al_2O_3

Al_2O_3 in combination with a TiCN base-layer is a frequently applied coating for turning applications. These hard coatings are commercially produced by CVD, since deposition of the required thick coatings via PVD is challenging, due to the electrically insulating nature of Al_2O_3 [10,32,86].

Alumina exists as the thermodynamically stable α-Al_2O_3 phase (corundum) and as metastable allotropic modifications such as γ, δ, η, χ, θ and κ [87]. α-Al_2O_3 belongs to the trigonal crystal system and has a rhombohedrally centered hexagonal lattice. The crystal structure of the stabile α-Al_2O_3 is described as approximately hexagonal close-packed (ABAB…); it involves six oxygen layers with Al ions occupying two-thirds of the octahedral sites [87,88].

Crystalline γ-Al_2O_3 with a fcc structure can be deposited using CVD at temperatures of about 800 °C and using PVD at temperatures between 350 and 550 °C, making them accessible for a wide range of substrates. Al_2O_3 PVD coatings deposited at lower temperatures are described to be X-ray amorphous [89–91]. For the synthesis of the desired stable α-Al_2O_3, deposition temperatures of ~700 °C are necessary using PVD [92,93].

The coatings discussed within this thesis have been grown by CVD (papers 1, 3 and 4). For the growth of alumina by CVD, the κ- or the α-phase are prevalent. However, the deposition temperatures are in the range of ~1,000 °C and thus remarkable higher compared to PVD, limiting the choice of substrate materials. Generally, CVD alumina coatings develop a crack network due to the mismatch of the thermal expansion coefficients of substrate and the individual coating layers. In the past the deposition of κ-Al_2O_3 was dominating, because synthesis of the desired stable α-Al_2O_3 was not possible [32,87,94,95]. The drawback of using the metastable κ-Al_2O_3 is that it transforms at elevated temperatures into the stable α-Al_2O_3, resulting in a volume shrinkage of about 7 %. As consequence of this shrinkage, a so-called secondary crack network is formed, resulting in loss of coating cohesion and performance during machining [11,35,85,87,88]. Several authors have shown that also precursor gas mixture, deposition time, doping agents and mechanical activation strongly influence the κ→α transformation [10,96]. As mentioned above, typically a TiCN base-layer, which matches the properties of the cemented carbide substrate and provides mechanical support for the Al_2O_3 top-layer, is applied, whereas the alumina top-layer provides chemical inertness, thermal stability, low thermal conductivity and hardness [6,10,86,88]. However, it is not straightforward to nucleate and grow α-Al_2O_3 if the nucleation surface is TiC, TiCN or TiN, which is typically the case when cemented carbide substrates are considered. The reason for this is that the nucleation of κ-Al_2O_3 is favorably

occurring on non-oxidized surfaces of TiC, TiCN or TiN [88]. The implementation of different kinds of interlayers and oxidizing treatments leads to the formation of nucleation layers between TiCN and Al_2O_3. This approach offers the possibility to directly grow α-Al_2O_3 without transformation and thus, without the development of additional thermal cracks [87,88,97–99]. Commercial processes apply TiCN, Ti(C,O) or Ti(C,O,N) interlayers or combinations of these followed by a Ti_xO_y template-nucleation of α-Al_2O_3 [88,99]. To prevent micro-chipping during application, the cutting edge or the complete rake face undergo post-treatment processes to smoothen the surface and to modify the tensile stress gradient within the Al_2O_3 layer [34,51]. The influence of post-treatment on the thermal crack network was investigated in paper 3.

4. Cutting operations and wear phenomena

Machining and research on this topic has been carried out for more than 100 years. The development of cutting machines, tools and tool materials led to an immense increase in cutting performance and consequently machining efficiency within the last century [100,101]. With respect to cutting tools, the improved cutting performance is owned to the development and enhancement of cemented carbides, ceramics and hard coatings deposited on the cutting tools. Accompanied with the development of tools, the understanding of wear mechanisms is of great importance to reach this improved cutting behavior [100]. Here, useful approaches like the model introduced by Taylor [102] for uncoated steel tools established the relationship between cutting speed and wear [103,104]. This model was later extended for coated cutting tools by Astakov [101,105]. Such models should be helpful for tool producers as well as for industrial users for the choice of suitable cutting tools and cutting parameters without intense investigations. In the following sections, emphasis was set on turning operations and the occurring wear mechanisms [101].

During machining, coated cemented carbide cutting inserts have to survive highly interrupted cutting conditions in combination with high temperatures, the latter in particular in continuous cutting operations. Machining of steels in a great variety of workpiece compositions as well as heat-treated states has to be covered with suitable cutting inserts. Cutting can be conducted dry or with the use of coolants and lubricants. The use of lubricants is today necessary for precise turning operations, here mostly oil in water emulsions with high water content for a proper cooling effect are applied. Primarily the use of lubricants is necessary to avoid oxidation of the uncoated insert, the coating and the workpiece. Typically tool tip temperatures during machining exceed 900 °C, which is beyond the possibilities of formerly applied coatings like TiN starting to oxidize at temperatures of about 500 °C, which leads to deterioration of the mechanical properties [8]. Today, the use of lubricants is reduced by the development of more oxidation resistant coatings based on nitrides, carbides, borides and oxides [23].

Depending on the machining process, cutting can be continuous or interrupted. In contrast to turning, where cutting is often continuous, in milling the cutting operation is interrupted, and accompanied by the occurrence of thermal cyclic stresses, since each cutting edge of a tool equipped with multiple inserts is only for a short time in contact with the workpiece material [100]. The interrupted tool/workpiece contact leads to thermal fatigue. The occurring thermo-shock – which is even more

pronounced using air-cooling or lubricants - leads to surface material shrinkage and fosters formation of tensile residual stress and thus crack formation [100,106].

The metal treading industry requires for turning high feed rates and high cutting speeds of up to 500 m/min. For such cutting applications, the use of CVD-coated cutting inserts with TiCN/Al_2O_3 hard coatings is common. Typically, cemented carbides used for turning have cobalt contents of 5 up to 12 wt% [8,35].

4.1 Turning

During turning the workpiece material is rotating while the cutting insert remains stationary. The tool holder moves continuous towards or along the workpiece axis, depending on the turning operation. An image of an industrial turning process is shown in Fig. 10a, whereas Fig. 10b presents a typical cutting insert for this cutting operation.

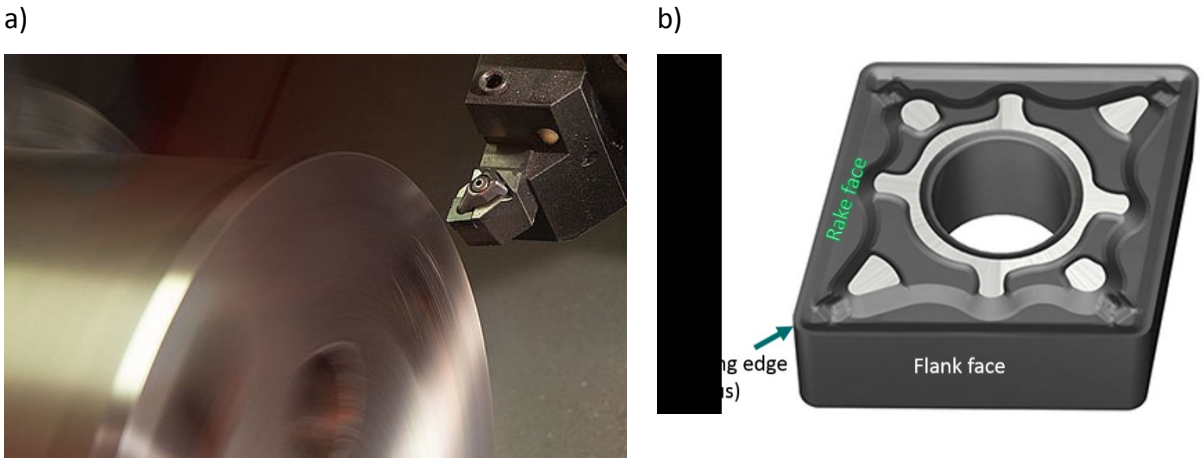

Fig. 10: a) Turning: The cylindrical workpiece is rotating. The cutting insert attached to the tool holder cuts the workpiece material in a certain depth. [107] *b) Schematic of a cemented carbide cutting insert in CNMG geometry as used within this thesis, adapted from* [107].

Within this thesis, the influence of cutting speed and workpiece material on wear and resulting tool life of CVD TiCN/Al_2O_3 coated cemented carbide cutting inserts was characterized. Thus, face, longitudinal and segmented turning tests (i.e. a combination of the two before mentioned) were conducted. The test setup for longitudinal turning tests is schematically shown in Fig. 11. In longitudinal turning, the cut is performed parallel to the rotation axis, in contrast to face turning, where the tool operates radially in direction to the center of the workpiece material. Longitudinal

turning can be operated as external as well as internal turning; both represent frequently applied industrial cutting processes. The experiments within this thesis are focused on external turning. Observations of the cutting inserts are often performed by light optical microscopy. For observation of wear on the cutting insert and the determination of the end of tool life, inspections were conducted recurrently after a defined number of cuts (e.g. 25) or a defined interval of time (e.g. one minute). For turning besides the choice of the suitable cutting insert with the required geometry, chip breaker, coating and surface condition, several cutting parameters such as *(i)* cutting speed v_c in m/min, defined as the product of workpiece circumference and its rotational speed in revolutions per minute (rpm); *(ii)* the feed rate f (rate of movement of the tool towards the rotating workpiece, the direction is depending on the applied cutting test, in mm/rev); *(iii)* depth of cut in mm; *(iv)* setting angle χ (angle the insert is in contact with the workpiece material) [100,108] have to be considered. Within this thesis, emphasis was set on the effect of a variation of the cutting speed (paper 4).

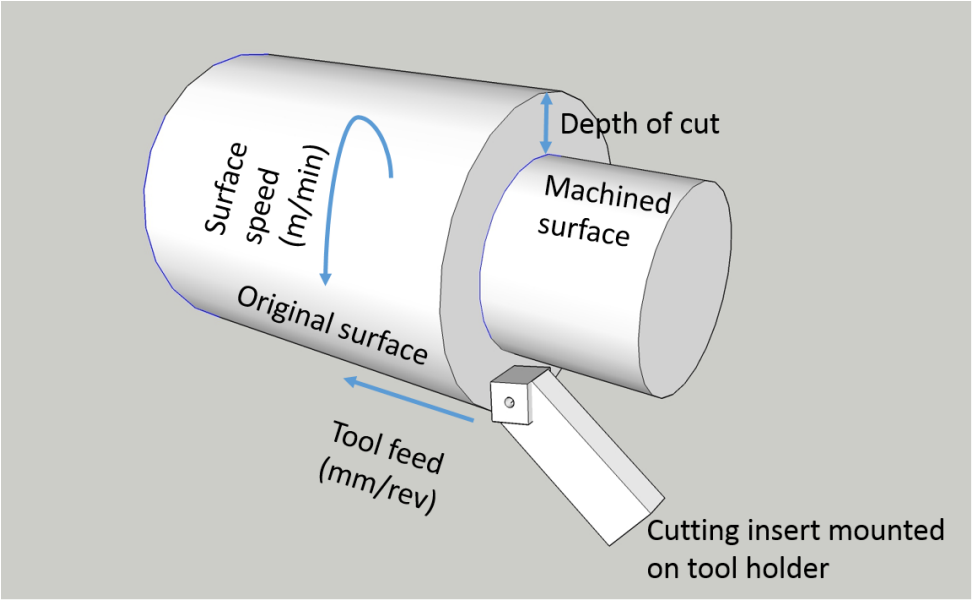

Fig. 11: Schematic of longitudinal turning for a cylindrical workpiece material, redrawn after [100,104].

Generally the chip-formation differs depending on the workpiece material and its properties. When turning steel, typically a continuous chip is formed, while when turning cast iron short chips are generated. The formation of the chip is further affected by the geometry of the cutting insert. Therefore, cutting inserts with several types of chip breakers are available, to ensure a controlled transport of the formed chip [100].

4.1.1 Wear criteria

Tool life for cutting is defined by the following wear criteria (see the schematic of a cutting insert shown in Fig. 10b): *(i)* flank wear reaching a defined value either at the flank face or on the nose radius of the insert; *(ii)* rake face crater wear. Generally, the flank wear is the wear at a certain stage of tool life and can be visualized in a tool life chart, were the operating time is plotted against the cutting speed [100]. For turning investigated within this thesis, a flank wear of 0.3 mm was defined as the end of tool life criterion. Beyond this limit, the insert becomes considerably weakened and will fail by plastic deformation and/or fracture. Accordingly, it is the tool wear that limits the overall performance of the cutting operation [100,108].

Wear can be caused by thermal, mechanical and/or chemical stresses. Mechanical stresses are caused by loads introduced via the contact of chip and the flank and/or rake face of the insert [104]. Most of the applied mechanical energy is transformed into heat, leading to additional thermal stresses. Only a part of the heat is transferred to the chips, the remaining heat is transferred to the workpiece material and the cutting tool and further transported to the environment and the eventually used cutting fluid. The resulting temperature gradient in the cutting insert is of importance for the subsequent wear [100].

On the rake face, wear can be observed by formation of a wear crater, as evidenced in Fig. 12. The breakthrough of the coating material takes place in the region were temperature reaches a maximum value [108]. Once the coating is damaged, the size of the crater, where the coating is removed, enlarges with further increasing cutting time. At the trailing edge of the crater (i.e. the position were the chip leaves the crater), coating material continuously breaks away, leading to a rapid increase of crater wear. When the crater wear reaches higher depths, cutting edge fracture and final tool failure occurs.

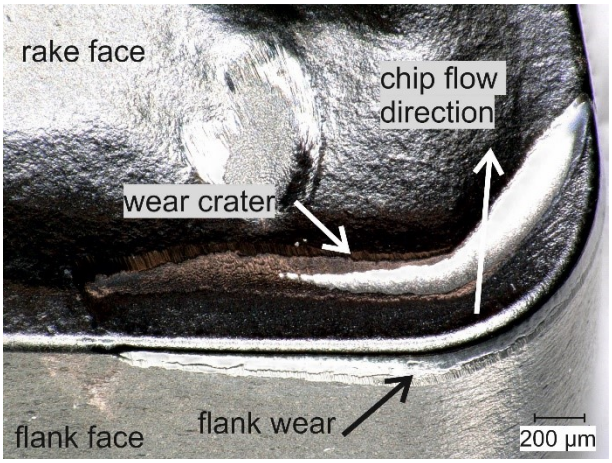

Fig. 12: Optical light micrograph of a TiCN/α-Al_2O_3 coated cutting insert after longitudinal turning [own work].

On the flank face, the end of tool life is typically defined by reaching the wear criteria of a flank wear of 0.3 mm. On the insert shown in Fig. 12, the end of tool life was reached by flank wear. Flank wear is strongly influenced by the radius of the cutting insert. Additionally the setting angle, i.e. the angle where the tool is in contact with the workpiece material, influences the flank wear. It may lead to a complete removal of the coating and to exposure of the cemented carbide substrate underneath to the contact to the chip [108]. Besides material removal, also plastic deformation plays a major role with respect to flank wear, since the occurring high temperatures of about 1,000 °C and the softening of the cemented carbide insert may lead to plastic deformation, as evidenced in paper 4 [109,110].

4.2 Wear characterization on coated cemented carbide cutting inserts

While in industrial application tool wear and tool failure is mostly characterized by screening with the naked eye, a more detailed insight into wear mechanisms is obtained by light-optical microscopy or SEM examinations. The evolution of wear on cutting inserts, which have been used to cut steel or cast iron workpiece materials, can be examined in more detail after removal of the adhered workpiece material. This can be easily done by immersion in HCl solution with a concentration of 30 – 50 % and slightly elevated temperatures up to 50 °C [108]. Subsequently to this cleaning procedure, a more detailed observation of tool failure, crater wear etc. is possible. Also the preparation of cross sections through worn areas by FIB could be an important approach for observation of tool wear, plastic deformation and crack propagation.

Besides characterization of inserts after turning, in tool development annealing tests under vacuum conditions or in a chosen atmosphere are frequently conducted, either for tailoring of the properties by modification of the microstructure of the insert or for the investigation of the effects of thermal loads and atmospheres on material degradation. For example, using this procedure, the stress changes due to high temperature exposure and diffusion processes can be studied. Within this thesis, annealing in ambient air was conducted to investigate the thermal crack network in CVD coated inserts (paper 3).

4.2.1 Wear mechanisms

The occurring wear mechanisms depend on the conditions applied for turning and are characteristic for the workpiece material to be cut and the used tool material [104]. During turning, the cutting inserts undergo different types of impact stresses. They can be caused by mechanical, thermal or chemical loads. Further, wear can be affected by constant or alternating stresses for different turning applications and by continuous or interrupted turning. The resulting wear modes are abrasion, adhesion, plastic deformation and fracture, crack formation, delamination, diffusion and oxidation [104].

Abrasion is caused by slipping between workpiece material and cutting tool, more precisely the component with a high hardness ploughs the softer counterpart. Thus, it is strictly caused by mechanical processes. Abrasive wear is present on the rake and on the flank face of the insert. It can be caused by sub-micrometer-sized particles, e.g. by Fe_3C (cementite) particles, present in hardened and tempered low allowed steels. This so-called micro-abrasion wear is the reason for formation of flat, smooth surfaces on worn Al_2O_3 coated cutting inserts, occurring at moderate cutting speeds (~200m/min), feed rates (~0.25/rev) and temperatures (~900 °C) [108]. Such a formation of a smooth flank face was observed in paper 4 of this thesis for cutting of quenched and tempered, ball-bearing and carbon steels.

Wear caused by adhesion occurs when components of the cutting tool are transferred to the chip or the machined surface caused by atomistic binding forces. Adhesion further leads to the formation of build-up edges. The formation of such build-up edges could be reduced by the application of hard coatings on cemented carbide inserts, which are not only reducing wear but also reduce the chemical affinity of workpiece material to stick on the insert surface [100]. Beside the application of hard

coatings, the formation of build-up edges can further be minimized by increasing the cutting speed or the application of lubricants.

Additionally to the plastic deformation of the insert, where the substrate deforms plastically, already in the early 1980s the effect of discrete plastic deformation occurring within the hard coating was reported. This form of plastic deformation or plastic material flow is characteristic for TiC, TiN, α- and κ-Al_2O_3 as well as for uncoated cutting inserts after turning. Here, the formation of ridges aligned parallel to the direction of the chip flow was observed. Initial deformation of asperities, formation of ridges, and appearance of ductile fracture represent the three stages characteristic for plastic deformation [108,111–113]. Fig. 13 exemplifies the effect of discrete plastic deformation on a TiCN/α-Al_2O_3 coated cutting insert used in face turning; the chip flow direction is indicated by the red arrows parallel to the characteristic ridges.

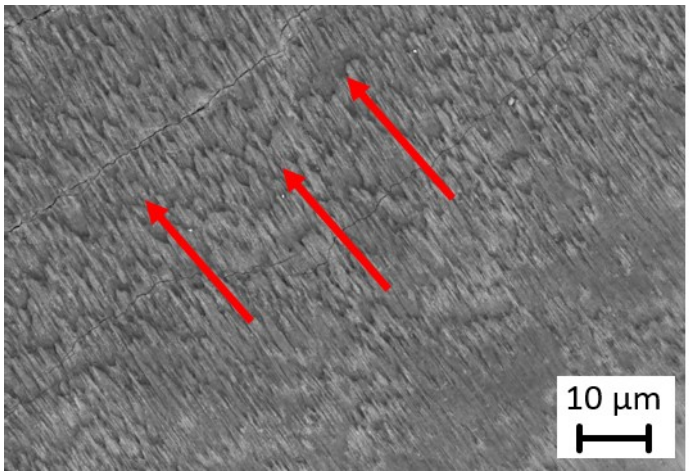

Fig. 13: SEM image taken in backscattered mode of the surface of a worn CVD TiCN/α-Al_2O_3 cutting insert after face turning. The chip flow direction is indicated with red arrows [own work].

Tribochemical wear is caused by diffusion. At elevated temperatures, the mobility of atoms and molecules increases. Thermally activated migration of species of the workpiece into the cutting tool and vice versa is promoted. Characteristic for the cutting of a carbon steel using a cemented carbide cutting tool, the following diffusion phenomena occur. On the one hand, Fe diffuses into the cobalt binder and consequently Fe-Co mixed solid solutions are formed. On the other hand, cobalt binder diffuses out of the cemented carbide tool. Carbon diffuses into the cemented carbide resulting in formation of Fe-W mixed carbides [104]. To minimize the effect of diffusion and prevent dissolution of the substrate material, TiC, TiN and Al_2O_3 coatings to protect cemented carbide tools and other

tool materials are used. Depending on the solubility of the tool material within the workpiece material, some cutting tool materials (e.g. high-speed steels) are essentially only useable when applying a protective hard coating [108].

Oxidation takes place within and near the chip contact zones. The raising temperatures during cutting promote the oxidation process. In this context, the workpiece material – or more precisely – the temperature were the workpiece material softens is of major impact. In the case the workpiece material softens at low temperatures, the influence of oxidation can be neglected [104]. Oxidation is most pronounced for TiC coatings, whereas TiN and – inherently – α-Al_2O_3 exhibit a much better resistance against oxidation. Dearnley *et al.* reported that the effect of notch formation (localized wear on both the rake and flank face of the insert at the depth-of-cut line) is oxidation driven or due to fretting fatigue [108].

Cracks can be observed as a result of turning, where cracks parallel and normal to the cutting edge are formed. Cracks parallel to the cutting edge are often called lateral cracks, while cracks normal to the cutting edge are called comb cracks, preferentially observed in milling. These cracks are caused by the heat transfer during turning, where the subsequent cooling and the resulting tensile stresses in the surface near zone promote crack formation. Typically, comb cracks appear in regular distances, since they depend on the volume change stemming from the heating and cooling cycles. A connection of both cracks - lateral and comb cracks – by degradation of the surrounding areas can also be observed [114].

In general, it can be stated that the wear of coated cemented carbide tools occurring during turning strongly depends on the combination of the tool material, the applied coating material(s) and the workpiece material. In addition, the cutting parameters have to be taken into account. Depending on the tool material – either the coating and the substrate or only the substrate in case of an uncoated tool – one of the mentioned tool wear mechanism is predominant, although in the most cases the reason for tool failure is an accumulation of differing wear mechanisms [108].

5. Summary and conclusions

Within this thesis, two important main topics the deposition of hard coatings on cemented carbide cutting tools and the application of such tools are addressed: first, the deposition technology with emphasis on the most relevant single contributions to the different deposition techniques and a special focus on the pretreatment of substrates before coating deposition; second, another focus was set on the application of coated cutting inserts by the examination of the thermal crack network within the coatings and the wear occurring during turning tests.

In particular, one aim of the presented thesis was to evaluate different deposition processes and the contribution of the individual process steps for giving space for possible improvements. Since deposition processes differ in energy and material consumption, the description of the respective contributions of the commonly used individual process steps heating, eventual pretreatment, deposition and cooling to the overall consumption of resources offers opportunities for possible savings. Depending on the used deposition process, batch size and substrate temperature, these contributions differ immensely. Both material flux and energy consumption for all process steps during batch coating of cutting tools by CVD and PVD were illuminated using Sankey diagrams within this thesis. This approach enables to calculate the consumed energy and material per coated cutting tool, but also to visualize each process step in terms of material consumption and energy flux and – in further consequence – to identify possible energy and material but also time saving potential. In PVD coating, the ion etching represents an important process step with valuable impact on the mentioned contributions. Hence, the influence of the variation of etching time and ion energy was investigated in detail, offering space for process optimization. Further, ion etching results in an efficient removal of material from the cemented carbide surface, and consequently also in an increase of surface roughness. This is most pronounced on the surfaces of sharp cutting edges, which poses challenges for the ion etching of tools with delicate sharp cutting geometries.

Within the second part of this thesis, emphasis was set on the behavior of CVD TiCN/Al_2O_3 coated cutting inserts during turning application. Thermal cracks represent weaknesses, since they enable diffusion and oxidation processes. A further contribution to tool wear is, that workpiece material is pressed into these cracks promoting crack extension. Tool life is also governed by the choice of cutting speed and workpiece material, as evidenced for turning of various steels. The wear patterns formed

on flank and rake face strongly depend on the tool/workpiece combination. For optimization of turning operations, the basic findings on tool wear, cutting speed and workpiece properties have to be correlated, to identify the optimum combination for best cutting performance.

For future work, the challenge of elaborating and referencing the obtained findings with respect to the effect of pretreatment steps of the chosen deposition technique on the particular tool performance arises and has to be addressed. Additionally, since for industrial use optimized cutting performance is of great importance, the further investigation of wear mechanisms during cutting taking into account additional cutting parameter variations could further enhance the present understanding of tool wear and provide the basis for an improved tool performance.

6. References

[1] P.H. Mayrhofer, C. Mitterer, L. Hultman, H. Clemens, Microstructural design of hard coatings, Prog. Mater. Sci. 51 (2006) 1032–1114.

[2] B. North, Six issues for the hard coatings community, Surf. Coat. Technol. 106 (1998) 129–134.

[3] Handbuch der Gewindetechnik und Frästechnik EMUGE-Franken, EMUGE-Franken, Erlangen, 2004.

[4] H. Holzschuh, Verschleißschutzschichten in der Werkzeugindustrie, in: Pulvermetallurgie für Hochpräzise Bauteile Und Dichte Hochleistungswerkstoffe, Fachverband Pulvermetallurgie, Hagen, 2007.

[5] M. Gassner, M. Rebelo de Figueiredo, N. Schalk, R. Franz, C. Weiß, H. Rudigier, et al., Energy consumption and material fluxes in hard coating deposition processes, Surf. Coat. Technol. 299 (2016) 49–55.

[6] C. Mitterer, PVD and CVD Hard Coatings, in: V.K. Sarin (Ed.), Compr. Hard Mater., Elsevier, Oxford, 2014: pp. 449–467.

[7] J. Faber, G. Hötzsch, C. Metzner, Sputter etching of steel substrates using DC and MF pulsed magnetron discharges.pdf, Vacuum. 64 (2002) 55–63.

[8] U. Schleinkofer, C. Czettl, C. Michotte, Coating Applications for Cutting Tools, in: V.K. Sarin (Ed.), Compr. Hard Mater., Elsevier, Oxford, 2014: pp. 453–469.

[9] D. Hochauer, C. Mitterer, M. Penoy, S. Puchner, C. Michotte, H.P. Martinz, et al., Carbon doped α-Al_2O_3 coatings grown by chemical vapor deposition, Surf. Coat. Technol. 206 (2012) 4771–4777.

[10] D. Hochauer, C. Mitterer, M. Penoy, C. Michotte, H.P. Martinz, M. Kathrein, Titanium doped CVD alumina coatings, Surf. Coat. Technol. 203 (2008) 350–356.

[11] N. Schalk, C. Mitterer, C. Czettl, B. Sartory, M. Penoy, C. Michotte, Dry-blasting of α- and κ-Al_2O_3 CVD hard coatings: Friction behaviour and thermal stress relaxation, Tribol. Lett. 52

(2013) 147–154.

[12] M. Rebelo de Figueiredo, TiCN hard coatings: tribological performance and deposition process analysis, 2011.

[13] R.F. Bunshah, S.M. Rossnagel, Handbook of Hard Coatings, Deposition Techonologies, Properties and Applications, Noyes Publications, New Jersey, 2001.

[14] D.M. Mattox, Handbook of Physical Vapor Deposition (PVD) Processing, Second edi, Oxford, 2010.

[15] R.F. Bunshah, J.M. Blocher, T.D. Bonifield, J.G. Fish, B.E. Jacobson, D.M. Mattox, et al., Deposition Technologies for Films and Coatings, Noyes Publications, New Jersey, 1982.

[16] P.M. Martin, Handbook of Deposition Technologies for Films and Coatings, 3rd ed., Elsevier Inc., 2010.

[17] R.A. Haefer, Oberflächen- und Dünnschicht-Technologie, Springer-Verlag, Berlin, 1987.

[18] J. Rother, B. Vetter, Plasmabeschichtungsverfahren und Hartstoffschichten, Deutscher Verlag für Grundstoffindustrie, Leipzig, 1992.

[19] P.J. Kelly, R.D. Arnell, Magnetron sputtering : a review of recent developments and applications, Vacuum. 56 (2000) 159–172.

[20] A. Anders, Cathodic arcs: From fractal spots to energetic condensation, Springer, New York, 2008.

[21] D. Sanders, A. Anders, Review of cathodic arc deposition technology at the start of the new millennium, Surf. Coat. Technol. 133-134 (2000) 78–90.

[22] M. Ohring, Materials Science of Thin Films, second, Academic Press, San Diego, 2002.

[23] M. Tkadletz, Advanced characterization techniques for the knowledge-based design of hard coatings, Montanuniversität Leoben, 2015.

[24] A. Hörling, L. Hultman, M. Odén, J. Sjölén, L. Karlsson, Thermal stability of arc evaporated high aluminum-content $Ti_{1-x}Al_xN$ thin films, J. Vac. Sci. Technol. A. 20 (2002) 1815.

[25] E. Taglauer, Surface cleaning using sputtering, Appl. Phys. A. 51 (1990) 238–251.

[26] C. Schönjahn, A.P. Ehiasarian, D.B. Lewis, R. New, W.D. Münz, Optimization of in situ subtrate surface treatment in a cathodic arc plasma: A study by TEM and plasma diagnostics, J. Vac. Sci. Technol. A. 19 (2001) 1415–1420.

[27] C. Schönjahn, D.B. Lewis, W.D. Münz, I. Petrov, Substrate ion etching in combined steered cathodic arc–ubm deposition system: effects on interface architecture, adhesion, and tool performance, Surf. Eng. 16 (2000) 176–180.

[28] C. Schönjahn, M. Bamford, L.A. Donohue, D.B. Lewis, S. Forder, W.D. Münz, The interface between TiAlN hard coatings and steel substrates generated by high energetic Cr+ bombardment, Surf. Coat. Technol. 125 (2000) 66–70.

[29] E.B. Macak, W.D. Münz, J.M. Rodenburg, Electron microscopy studies of hard coatings deposited on sharp edges by combined cathodic arc / unbalanced magnetron PVD, Surf. Coat. Technol. 152 (2002) 349–354.

[30] H.O. Pierson, Handbook of chemical vapor deposition (CVD), second edi, Noyes Publications, Park Ridge, 1999.

[31] K. Choy, Chemical vapour deposition of coatings, Prog. Mater. Sci. 48 (2003) 57–170.

[32] S. Ruppi, Advances in chemically vapour deposited wear resistant coatings, J. Phys. IV. 11 (2001) 847–859.

[33] A. Larsson, S. Ruppi, Microstructure and properties of Ti(C,N) coatings produced by moderate temperature chemical vapour deposition, Thin Solid Films. 402 (2002) 203–210.

[34] N. Schalk, Synthesis and Post-treatment of Hard Coatings for Cemented Carbide Cutting Tools, Montanuniversität Leoben, 2013.

[35] C. Czettl, Design of CVD Coatings for Cutting Tools, Montanuniversität Leoben, 2013.

[36] P.B. Barna, M. Adamik, Fundamental structure forming phenomena of polycrystalline films and the structure zone models, Thin Solid Films. 317 (1998) 27–33.

[37] B.A. Movchan, A. V. Demchishin, Study of the structure and properties of thick vacuum condensates of nickel, titanium, tungsten, aluminium oxide and zirconium dioxide, Phys. Met. Met. 28 (1969) 653–660.

[38] J.A. Thornton, Influence of apparatus geometry and deposition conditions on the structure and topography of thick sputtered coatings, J. Vac. Sci. Technol. 11 (1974) 666–670.

[39] I. Petrov, P.B. Barna, L. Hultman, J.E. Greene, Microstructural evolution during film growth, J. Vac. Sci. Technol. A. 21 (2003) S117.

[40] R. Messier, A.P. Giri, R.A. Roy, Revised structure zone model for thin film physical structure, J. Vac. Sci. Technol. A. 2 (1984) 500–503.

[41] R. M'Saoubi, O. Alm, J.M. Andersson, H. Engström, T. Larsson, M.P. Johansson-Jõesaar, et al., Microstructure and wear mechanisms of texture-controlled CVD α-Al_2O_3 coatings, Wear. 376-377 (2017) 1766–1778.

[42] A. Anders, A structure zone diagram including plasma-based deposition and ion etching, Thin Solid Films. 518 (2010) 4087–4090.

[43] H.P.R. Sankey, Minutes of Proceedings of the Institution of Civil Engineers, Minutes Proc. Inst. Civ. Eng. 125 (1896) 182–242.

[44] H.P.R. Sankey, Introductory Note on the Thermal Efficiency of Steam-Engines, Minutes Proc. Inst. Civ. Eng. 134 (1898) 278–283.

[45] M. Schmidt, The Sankey Diagram in Energy and Material Flow Management Part II. Methodology and Current Applications, J. Ind. Ecol. 12 (2008) 173–185.

[46] A. Riedler, S. Löffler, Energiefluss der Maschine, in: Oelmaschinen, Berlin, 1916: pp. 124–127.

[47] G. Kalt, Biomass streams in Austria: Drawing a complete picture of biogenic material flows within the national economy, Resour. Conserv. Recycl. 95 (2015) 100–111.

[48] A. Bakenne, W. Nuttall, N. Kazantzis, Sankey-Diagram-based insights into the hydrogen economy of today, Int. J. Hydrogen Energy. 41 (2016) 7744–7753.

[49] M. Tkadletz, J. Keckes, N. Schalk, I. Krajinovic, M. Burghammer, C. Czettl, et al., Residual stress gradients in α- Al_2O_3 hard coatings determined by pencil-beam X-ray nanodiffraction: The influence of blasting media, Surf. Coat. Technol. 262 (2015) 134–140.

[50] H. Holzschuh, M. Klaus, C. Genzel, Influence of the residual stress state on the toughness of CVD - Coated cemented carbide cutting tools, in: Adv. Powder Metall. Part. Mater. Mater. PowderMet 2008, Washington D.C., 2008: p. 100

[51] M. Klaus, C. Genzel, H. Holzschuh, Residual stress depth profiling in complex hard coating systems by X-ray diffraction, Thin Solid Films. 517 (2008) 1172–1176.

[52] A. Riedl, N. Schalk, C. Czettl, B. Sartory, C. Mitterer, Tribological properties of Al_2O_3 hard coatings modified by mechanical blasting and polishing post-treatment, Wear. 289 (2012) 9–16.

[53] K.-D. Bouzakis, G. Skordaris, G. Gerardis, G. Katirzoglou, S. Makrimallakis, F. Klocke, et al., The Effect of Micro-Blasting on the Cutting Performance of Coated Tools, FME Trans. 37 (2009) 71–82.

[54] K.D. Bouzakis, E. Bouzakis, G. Skordaris, S. Makrimallakis, A. Tsouknidas, G. Katirtzoglou, et al., Effect of PVD films wet micro-blasting by various Al_2O_3 grain sizes on the wear behaviour of coated tools, Surf. Coat. Technol. 205 (2011) S128–S132.

[55] W.D. Münz, Titanium aluminium nitride films: A new alternative to TiN coatings, J. Vac. Sci. Technol. A. 4 (1986) 2717–2725.

[56] E. Bergmann, F. Dupont, S. Steiger, The use of system theory for the tibological optimisation of decorative coatings, in: Conf. Ion an Plasma Assist. Tech., CEP Consultants Edinburgh, Brussels, 1991: pp. 256–260.

[57] N. Savvides, B. Window, Unbalanced magnetron ion-assisted and property modificatiob of thin films, J. Vac. Sci. Technol. A. 4 (1986) 504–508.

[58] C. Czettl, C. Mitterer, U. Mühle, D. Rafaja, S. Puchner, H. Hutter, et al., CO addition in low-pressure chemical vapour deposition of medium-temperature TiC_xN_{1-x} based hard coatings, Surf. Coat. Technol. 206 (2011) 1691–1697.

[59] M. Mühlbacher, G. Greczynski, B. Sartory, F. Mendez-Martin, N. Schalk, J. Lu, et al., TiN diffusion barrier failure by the formation of Cu_3Si investigated by electron microscopy and atom probe tomography, J. Vac. Sci. Technol. B, Nanotechnol. Microelectron. Mater. Process. Meas. Phenom. 34 (2016) 022202–(1–7).

[60] M. Mühlbacher, F. Mendez-Martin, B. Sartory, N. Schalk, J. Keckes, J. Lu, et al., Copper diffusion into single-crystalline TiN studied by transmission electron microscopy and atom probe tomography, Thin Solid Films. 574 (2015) 103–109.

[61] C. Czettl, U. Schleinkofer, F. Schedle, C. Wolf, M. Lechleitner, H. Holzschuh, et al., CVD TiAlN – Development and challenges for use in mass production, in: 19th Plansee Semin. 2017, 2017.

[62] H.A. Jehn, B. Rother, Preparation and concentration distribution of multicomponent hard coatings, Int. J. Refract. Met. Hard Mater. 14 (1996) 87–95.

[63] S. PalDey, S.C. Deevi, Single layer and multilayer wear resistant coatings of (Ti,Al)N: a review, Mater. Sci. Eng. A. 342 (2003) 58–79.

[64] M. Durandurdu, Pressure-induced phase transition of zinc-blende AlN: An ab initio molecular dynamics study, J. Phys. Chem. Solids. 69 (2008) 2894–2897.

[65] J. Kohlscheen, H.R. Stock, P. Mayr, Substoichiometric titanium nitride coatings as machinable surfaces in ultraprecision cutting, Surf. Coat. Technol. 120-121 (1999) 740–745.

[66] H. Holleck, Metastable coatings - prediction of compositionn and structure, Surf. Coat. Technol. 36 (1988) 151–159.

[67] I.W. Park, D.S. Kang, J.J. Moore, S.C. Kwon, J.J. Rha, K.H. Kim, Microstructures, mechanical properties, and tribological behaviors of Cr-Al-N, Cr-Si-N, and Cr-Al-Si-N coatings by a hybrid coating system, Surf. Coat. Technol. 201 (2007) 5223–5227.

[68] E. Spain, J.C. Avelar-Batista, M. Letch, J. Housden, B. Lerga, Characterisation and applications of Cr-Al-N coatings, Surf. Coat. Technol. 200 (2005) 1507–1513.

[69] K. Kutschej, P.H. Mayrhofer, M. Kathrein, P. Polcik, R. Tessadri, C. Mitterer, Structure, mechanical and tribological properties of sputtered $Ti_{1-x}Al_xN$ coatings with $0.5 \leq x \leq 0.75$, Surf. Coat. Technol. 200 (2005) 2358–2365.

[70] A. Hörling, L. Hultman, M. Odén, J. Sjölén, L. Karlsson, Mechanical properties and machining performance of $Ti_{1-x}Al_xN$-coated cutting tools, Surf. Coat. Technol. 191 (2005) 384–392.

[71] M. Kawate, A. Kimura, T. Suzuki, Microhardness and lattice parameter of $Cr_{1-x}Al_xN$ films, J. Vac. Sci. Technol. A. 20 (2002) 569–571.

[72] H. Willmann, Al-Cr-N thin film design for high temperature applications, Montanuniversität Leoben, 2007.

[73] P.H. Mayrhofer, F.D. Fischer, H.J. Böhm, C. Mitterer, J.M. Schneider, Energetic balance and kinetics for the decomposition of supersaturated $Ti_{1-x}Al_xN$, Acta Mater. 55 (2007) 1441–1446.

[74] P.H. Mayrhofer, A. Hörling, L. Karlsson, J. Sjölén, T. Larsson, C. Mitterer, et al., Self-organized nanostructures in the Ti-Al-N system, Appl. Phys. Lett. 83 (2003) 2049–2051.

[75] M. Pfeiler, G.A. Fontalvo, J. Wagner, K. Kutschej, M. Penoy, C. Michotte, et al., Arc evaporation of Ti-Al-Ta-N coatings: The effect of bias voltage and Ta on high-temperature tribological properties, Tribol. Lett. 30 (2008) 91–97.

[76] P.H. Mayrhofer, R. Rachbauer, D. Holec, F. Rovere, J.M. Schneider, Protective Transition Metal Nitride Coatings, Elsevier, 2014.

[77] B. Grossmann, A. Jamnig, N. Schalk, C. Czettl, M. Pohler, C. Mitterer, Tailoring age hardening of $Ti_{1-x}Al_xN$ by Ta alloying, J. Vac. Sci. Technol. A. A35(6) (2017).

[78] L. Karlsson, L. Hultman, M.P. Johansson, J.-E. Sundgren, H. Ljungcrantz, Growth, microstructure, and mechanical properties of arc evaporated TiC_xN_{1-x} ($0 \leq x \leq 1$) films, Surf. Coat. Technol. 126 (2000) 1–14.

[79] T. Polcar, R. Novák, P. Široký, The tribological characteristics of TiCN coating at elevated temperatures, Wear. 260 (2006) 40–49.

[80] H.G. Prengel, W.R. Pfouts, A.T. Santhanam, State of the art in hard coatings for carbide cutting tools, Surf. Coat. Technol. 102 (1998) 183–190.

[81] S.J. Bull, D.G. Bhat, M.H. Staia, Properties and performance of commercial TiCN coatings. Part 1: Coating architecture and hardnes modelling, Surf. Coat. Technol. 163-164 (2003) 499–506.

[82] M. Rebelo De Figueiredo, J. Neidhardt, R. Franz, C. Mitterer, Low-friction mechanisms active for carbon containing coatings: Ti-C-N as a model system, Berg- und Hüttenmännische Monatshefte. 153 (2008) 263–267.

[83] A.T. Santhanam, D.T. Quinto, G.P. Grab, Comparison of the steel-milling performance of carbide inserts with MTCVD and PVD TiCN coatings, Int. J. Refract. Met. Hard Mater. 14 (1996) 31–40.

[84] W. Schintlmeister, O. Pacher, Titankarid und -nitride für hochverschleißfeste und dekorative Schichten, Metall. (1974) 690–695.

[85] J. Skogsmo, M. Halvarsson, Microstructural study of the κ-Al_2O_3 - α-Al_2O_3 transformation in CVD κ-Al2O3, (1992) 186–192.

[86] A. Osada, E. Nakamura, H. Homma, T. Hayahi, T. Oshika, Wear mechanism of thermally transformed CVD Al_2O_3 layer, Int. J. Refract. Met. Hard Mater. 24 (2006) 387–391.

[87] S. Vuorinen, L. Karlsson, Phase transformation in chemically vapour-deposited κ-alumina, Thin Solid Films. 214 (1992) 132–143.

[88] S. Ruppi, Deposition, microstructure and properties of texture-controlled CVD α-Al_2O_3 coatings, Int. J. Refract. Met. Hard Mater. 23 (2005) 306–316.

[89] A. Schütze, D.T. Quinto, Pulsed plasma-assisted PVD sputter-deposited alumina thin films, Surf. Coat. Technol. 162 (2003) 174–182.

[90] R. Cremer, M. Witthaut, D. Neuschütz, G. Erkens, T. Leyendecker, M. Feldhege, Comparative characterization of alumina coatings deposited by RF, DC and pulsed reactive magnetron sputtering, Surf. Coat. Technol. 120-121 (1999) 213–218.

[91] M. Astrand, T.I. Selinder, F. Fietzke, H. Klostermann, PVD-Al_2O_3-coated cemented carbide cutting tools, Surf. Coat. Technol. 188-189 (2004) 186–192.

[92] O. Zywitzki, G. Hoetzsch, Correlation between structure and properties of reactively deposited Al_2O_3 coatings by pulsed magnetron sputtering, Surf. Coat. Technol. 94-95 (1997) 303–308.

[93] T. Kohara, H. Tamagaki, Y. Ikari, H. Fujii, Deposition of α-Al_2O_3 hard coatings by reactive magnetron sputtering, Surf. Coat. Technol. 185 (2004) 166–171.

[94] S. Ruppi, A. Larsson, A. Flink, Nanoindentation hardness, texture and microstructure of α-Al_2O_3 and κ-Al_2O_3 coatings, Thin Solid Films. 516 (2008) 5959–5966.

[95] S. Ruppi, A. Larsson, Chemical vapour deposition of α-Al_2O_3, Thin Solid Films. 388 (2001) 50–61.

[96] M. Kathrein, W. Schintlmeister, W. Wallgram, U. Schleinkofer, Doped CVD Al_2O_3 coatings for high performance cutting tools, Surf. Coat. Technol. 164 (2003) 181–188.

[97] M. Halvarsson, H. Nordén, Microstructural investigation of CVD multilayer coatings, Surf. Coat. Technol. 61 (1993) 177–181.

[98] M. Halvarsson, H. Nordén, The microstructure of bonding layers for CVD alumina coatings, Surf. Coat. Technol. (1994) 266–273.

[99] M. Fallqvist, S. Ruppi, M. Olsson, M. Ottosson, T.M. Grehk, Nucleation and growth of CVD α-Al_2O_3 on Ti_xO_y template, (2012) 254–261.

[100] W. Schedler, Hartmetall für den Praktiker, VDI-Verlag GmbH, Düsseldorf, 1988.

[101] V.P. Astakhov, Metal cutting mechanics, CRC Press LLC, 1998.

[102] F.W. Taylor, On the art of cutting Metals, The American Society of mechanical engineers, New York, 1906.

[103] R. Storf, Drehen: Grundlagen und Anwendungstechnik, VDI-Verlag GmbH, 1987.

[104] H.K. Tönsdorff, Spanen, Springer-Verlag, 1995.

[105] V.P. Astakhov, J.P. Davim, Tools (Geometry and Material) and Tool Wear, in: Mach. Fundam. Recent Adv., 2008: p. 362.

[106] T. Teppernegg, P. Angerer, T. Klünsner, C. Tritremmel, C. Czettl, Evolution of residual stress in Ti-Al-Ta-N coatings on hard metal milling inserts, Int. J. Refract. Met. Hard Mater. 52 (2015) 171–175.

[107] Ceratizit, application, (n.d.). https://www.ceratizit.com/en/products/metal-cutting/application/] (accessed September 20, 2018)

[108] P.A. Dearnley, Introduction to Surface Engenieering, Cambridge University Press, Cambridge, 2017.

[109] M. Gassner, N. Schalk, M. Tkadletz, M. Pohler, C. Czettl, C. Mitterer, Influence of cutting speed and workpiece material on the wear mechanisms of CVD TiCN/α- Al_2O_3 coated cutting inserts during turning, Wear. (2018).

[110] I. Krajinovic, W. Daves, M. Tkadletz, T. Teppernegg, T. Klünsner, N. Schalk, et al., Finite element study of the influence of hard coatings on hard metal tool loading during milling, Surf. Coat. Technol. 304 (2016) 134–141.

[111] P.A. Dearnley, E.M. Trent, Wear mechanisms of coated carbide tools, Mater. Technol. 9 (1982) 60–75.

[112] P.A. Dearnley, R.F. Fowle, N.M. Corbett, D. Doyle, Wear mechanisms of physical and chemical vapour deposited ceramic coatings used in metal cutting applications, Surf. Eng. 9 (1993) 312–313.

[113] S. Ruppi, Enhanced performance of α-Al_2O_3 coatings by control of crystal orientation, Surf. Coat. Technol. 202 (2008) 4257–4269.

[114] J. García, T. Carvalho Miranda, H.C. Pinto, F. Soldera, F. Mücklich, 3D-FIB Characterization of Wear in WC-Co Coated Composites, Mater. Sci. Forum. 825-826 (2015) 995–1000.

[115] D.M. Mattox, Ion Plating Technology, in: Depos. Technol. Film. Coatings, Noyes Publ., New Jersey, 1982.

7. Publications

7.1 List of included publications

I. Energy consumption and material fluxes in hard coating deposition processes
M. Gassner, M. Rebelo de Figueiredo, N. Schalk, R. Franz, C. Weiß, H. Rudigier, H. Holzschuh, W. Bürgin, M. Pohler, C. Czettl, C. Mitterer
Surface & Coatings Technology 299 (2016) 49–55

II. Influence of Ar ion etching on the surface topography of cemented carbide cutting inserts
M. Gassner, N. Schalk, B. Sartory, M. Pohler, C. Czettl, C. Mitterer
International Journal of Refractory Metals & Hard Materials 69 (2017) 234–239

III. Thermal crack network on CVD TiCN/α-Al_2O_3 coated cemented carbide cutting tools
M. Gassner, N. Schalk, M. Tkadletz, C. Czettl, C. Mitterer
Manuscript submitted for publication

IV. Influence of cutting speed and workpiece material on the wear mechanisms of CVD TiCN/α-Al_2O_3 coated cutting inserts during turning
M. Gassner, N. Schalk, M. Tkadletz, M. Pohler, C. Czettl, C. Mitterer
Wear 398–399 (2018) 90–98

Publication I

Energy consumption and material fluxes in hard coating deposition processes

M. Gassner, M. Rebelo de Figueiredo, N. Schalk, R. Franz, C. Weiß,
H. Rudigier, H. Holzschuh, W. Bürgin, M. Pohler, C. Czettl, C. Mitterer

Surface & Coatings Technology 299 (2016) 49–55

Energy consumption and material fluxes in hard coating deposition processes

Martina Gassner[1], Marisa Rebelo de Figueiredo[1], Nina Schalk[1], Robert Franz[1], Christian Weiß[2], Helmut Rudigier[3], Helga Holzschuh[4], Werner Bürgin[4], Markus Pohler[5], Christoph Czettl[5], Christian Mitterer[1]

[1] Department of Physical Metallurgy and Materials Testing, Montanuniversität Leoben, Franz-Josef-Straße 18, 8700 Leoben, Austria

[2] Chair of Process Technology and Industrial Environmental Protection, Montanuniversität Leoben, Franz-Josef-Straße 18, 8700 Leoben, Austria

[3] Oerlikon Surface Solutions AG, Iramali 18, 9496 Balzers, Liechtenstein

[4] Sucotec AG, Aarwangenstrasse 92a, 4900 Langenthal, Switzerland

[5] CERATIZIT Austria GmbH, Metallwerk-Plansee-Straße 71, 6600 Reutte, Austria

Abstract

Hard coatings grown by physical vapor deposition (PVD) or chemical vapor deposition (CVD) on cutting tools are applied to considerably increase the tools' performance and lifetime. Besides differences in types, thicknesses, structures and properties of the coatings synthesized by PVD and CVD, the deposition processes differ significantly in their throughput of tools as well as their energy and material consumption. Within this work, a methodology to analyze the energy and material fluxes of typical PVD and CVD processes for the deposition of hard coatings on cutting tools is introduced. Three case studies are considered: *(i)* cathodic arc evaporation of TiCN, *(ii)* magnetron sputter deposition of TiN, and *(iii)* CVD of a TiCN/Al_2O_3 bilayer coating. The material fluxes and energy consumption for each process step of the respective deposition processes were monitored and are illustrated by individual Sankey diagrams. The visualization by Sankey diagrams allows to readily identify the main energy and mass consuming process steps. Finally, a normalization procedure enabling the comparison of different hard coating production routes is presented and discussed.

Keywords: CVD, PVD, hard coatings, material flux, energy consumption, Sankey diagram

1. Introduction

Thin hard coatings are commonly used for wear protection to improve the performance of tools, dies and molds [1,2]. Overall, about 75 % of all cutting tools and in particular more than 90 % of all cutting inserts made of cemented carbide are coated by chemical vapor deposition (CVD) or physical vapor deposition (PVD) techniques, with CVD being used in more than half and PVD in slightly less than a

quarter of the cases, while the remaining fraction is uncoated [1,3,4]. Table 1 summarizes the main characteristics of the two PVD techniques, i.e. cathodic arc evaporation (CAE) and magnetron sputter deposition (MSD), and the thermally activated CVD process which were analyzed in the current study. In addition to the different deposition temperatures, which determine possible substrate materials, also the typical coating thicknesses and sample loads vary among PVD and CVD, where significantly higher sample loads and coating thicknesses are common for the latter method. Further, CVD and PVD processes differ with respect to typical coating materials, structure and properties, but also in their energy and material consumption. However, a systematic evaluation of the efficiency of these coating processes is not available in literature.

Table 1: Overview of typical features of the different deposition techniques considered in the case studies [17,25–28]. *Values for the typical loads are given considering cemented carbide half-inch cutting inserts of 12.7 mm.*

process parameter	CAE	MSD	CVD
temperature	200 – 600 °C	350 – 600 °C	750 – 1150 °C
coating thickness	≤ 10µm	≤ 6 µm	≤ 30 µm
typical coating materials for cutting tools	TiN, TiCN, Ti(Al)N, Cr(Al)N	TiN, TiCN, Ti(Al)N, Cr(Al)N	TiCN, TiN, Al_2O_3
typical loads in industrial deposition plants	~2,000-10,000	~2,000 – 10,000	~10,000 – 20,000

The aim of the present work is to develop a methodology to analyze the energy and material fluxes for typical PVD and CVD processes used for the deposition of hard coatings on cutting tools. The material and energy fluxes for each deposition step have been recorded and Sankey diagrams were generated, where the main energy and material consuming process steps are readily identifiable. In 1898, Sankey suggested a diagram to illustrate the efficiency of steam engines, describing the energy flow graphically by the arrangement of arrows illustrating different contributions [5,6]. The advantage is that the quantity of all flows could be summed up and so the summed-up respective arrow width corresponds to the total flow within a defined system. Later on, Sankey diagrams were also used to compare different processes, like the efficiency of diesel and gas engines [7]. Today, they are used in very different fields like for monitoring biomass streams [8], the global water flow per annum [9] or

the efficiency limits of energy converting devices [10]. Sankey diagrams are an important tool in identifying inefficiencies and potential for savings when dealing with resources. They are typically used to visualize energy, material or cost transfers between processes.

Within this work, the Sankey diagrams are applied to visualize the mass throughput and the respective energy contributions of the process steps for three case studies based on exemplary lab deposition processes, i.e. arc evaporation of TiCN, magnetron sputter deposition of TiN and CVD of TiCN/α-Al_2O_3. Thereby, the energy contributions are quantified as electrical power per process time interval. These case studies have been chosen as typical processes for the deposition of hard coatings. The demonstrated quantification and visualization by Sankey diagrams allow to determine the fraction of the total material that is incorporated in the coating. To generalize the methodology, the determined mass and energy fluxes are normalized per micrometer coating thickness.

2. Deposition Techniques

In PVD methods, solid precursor materials, so-called cathodes or targets, are used. Depending on how the solid material is transferred into the (ionized) vapor phase, evaporation and sputtering can be distinguished [11]. Evaporation is based on the transfer of the solid target material into the vapor phase by applying heat. Using a cathodic arc, evaporation of the target material is realized using a high current, low voltage electrical discharge, the so-called arc. It is ignited between the anode, typically the grounded chamber wall, and the cathode to be evaporated [12]. Within the first case study, TiCN coatings were grown by arc evaporation. The TiCN coating was deposited at a substrate temperature of ~450 °C under a constant flow of Ar (700 sccm) and C_2H_2 (100 sccm) (see ref. [13] for more details on the deposition process), whereas the N_2 flow was adjusted in order to maintain a total pressure of 3 Pa. The arc current was set to 180 A for each of the four arc sources equipped with Ti targets. A bias voltage of -100 V was applied to the substrates.

Using MSD, the solid target material is transferred into the vapor phase by energy and momentum transfer from impinging ions. These ions, usually Ar^+, are provided by igniting a glow discharge between the target (cathode) and the chamber wall (anode) [14,15]. The TiN coatings considered within the second case study were grown using unbalanced pulsed direct current magnetron sputter deposition. The TiN coating was synthesized under a constant Ar flow (200 sccm) and the chamber

was backfilled with N_2 to a total pressure of 0.58 Pa. The four magnetrons equipped with Ti targets were operated in constant power mode set to 7 kW for each magnetron, applying bipolar pulses at a frequency of 50 kHz and a duty cycle of 50 %. The bias voltage was set to - 50 V with a pulse frequency of 350 kHz (bipolarily pulsed) and a reversal time of 1000 ns (for more details on the deposition process see ref. [16]).

In contrast to PVD, in thermally activated CVD gaseous precursors are introduced into the deposition reactor and form the desired chemical compound of the coating at elevated temperatures [17]. In the third case study considered here, TiCN/α-Al_2O_3 bilayer coatings were deposited. The α-Al_2O_3 layer was synthesized from $AlCl_3$-CO_2-H_2-H_2S precursors at a temperature of ~1000 °C [18] and a pressure of 7.5 kPa (for more details on the deposition process see ref. [19]). As base layer, TiCN was deposited via medium-temperature CVD at 900 °C using a gas mixture of $TiCl_4$-CH_3CN-H_2-N_2 at a pressure of 10 kPa (for more details on the deposition process see refs. [18,20–22]). The use of CH_3CN instead of CH_4 enables deposition of TiCN at lower temperatures, which prevents formation of the brittle η phase in cemented carbide substrates [20].

3. Methodology

For all deposition processes, the mass and energy fluxes were recorded and divided into steps. Fig. 1 gives an overview of the different deposition steps. The energy consumption was calculated from the nominal capacity and the effective utilization during the respective process steps for each component involved in the deposition plant (bias generator, heaters, pumps, cathodes, filament and coils, ventilators). For MSD and CVD, the calculation was based on the effective utilization during the process steps. For CAE all pumps are considered to run at full power during the deposition cycle, accepting the fact that this would lead to an overestimation in energy consumption. For the mass flux diagrams, the streamed-in gas fluxes were considered for each process step and the mass flux was determined by the read-out of the mass flow controllers and the respective gas density. In the two PVD processes, prior to mounting on the cathode holders or magnetrons, all targets were weighed to determine the initial mass. After deposition, the mass of the targets was measured again and the mass loss per coating deposition time was calculated. The amount of water for cooling was not considered in any case study, because all deposition systems are working with a closed cooling water circuit, with several coating units which makes a separation impossible. To provide a reference point for a rough

estimation, a typical chiller system for the two PVD processes considered here will consume an approximate energy of 6 kWh, contributing to about 6 % of the overall energy consumed. For the CVD process, the liquid components for neutralization of the reactions products were considered according to manufacturer's instructions.

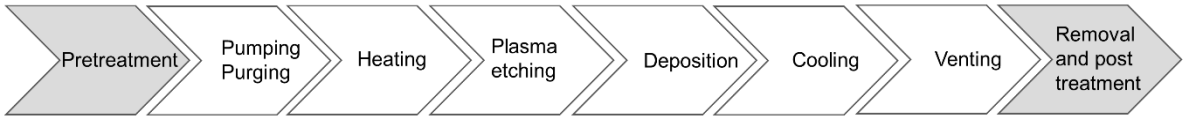

Fig. 1: Sequential steps of deposition processes. In the case of the PVD processes, the steps Pumping, Purging and Venting have been included into the steps Heating and Cooling, respectively. In the case of the CVD process, the step Pumping/Purging was included into the step Heating; the steps Plasma etching and Venting are absent.

For all processes, prior to mounting in the chamber, the substrates were cleaned in ethanol in an ultrasonic bath. They were weighed before and after the deposition process to determine the mass gain of the coated substrates. The mass loss according to the ion etching step prior to coating deposition in the two PVD processes could not be considered, because it was close or even below the resolution limit of high-precision mass balances. The coating thickness was determined by a spherical abrasion test, averaged for at least three substrates mounted on representative positons at the substrate holders. It should be noted that the remaining positions were filled by dummy substrates. Using the chemical composition of the synthesized coating, which was determined for the CVD and MSD processes by energy dispersive X-ray spectroscopy and for the CAE process by elastic recoil detection analysis, the mass fraction of each element in the deposited substrates was calculated. All other masses, which were not incorporated in the coating on the substrates, were assumed to be deposited on the carousel and/or substrate holder and the chamber walls or, in the case of gaseous components, left the process as outgoing gas.

For MSD, cemented carbide substrates in three different geometries were used. Three disks (∅ 30 mm × 4 mm) and three SNUN 120412 inserts (according to ISO 1832) were mounted on a substrate holder operating in twofold rotation. In addition, nine CNMG 120408 inserts (according to ISO 1832) were mounted to undergo threefold rotation. The material flux during CAE was recorded using three high-speed steel drills with threefold rotation. For CVD, CNMG 120408 substrates were used. To take into account the whole deposition batch, three samples were positioned in the top, middle and

bottom levels of the substrate holder, respectively. Within these levels, the substrates were placed in the center, on the half radius and close to the edge of the sample holder [23,24].

As the sample load in the respective deposition plants varies with the substrate geometry, it was assumed for our calculation that all three deposition plants were loaded with cemented carbide cutting inserts in CNMG 120408 geometry, which are rectangular and have an edge length of 12.7 mm, a thickness of 4.76 mm and a total coated area of approximately 6 cm^2. It should be mentioned that with this simplified assumption differences in batch runs and areas are neglected. The corresponding calculated loads are shown in Table 2. Based on these assumed sample loads, the total useful coated area of fully loaded deposition plants was extrapolated. Considering the respective chamber features (substrate holders, heaters, protective sheds, etc.), which are unintentionally coated, only a minor fraction of the coating flux is deposited on the tools.

Table 2: Process parameters for the deposition processes investigated within the three case studies. The sample load was estimated and given values extrapolated from the limited samples used in this study to the full capacity of the respective deposition chamber.

case study	sample load	process cycle time	coating material	layer thickness
CAE	3,500	3 h 27 min	TiCN	2.5 µm
MSD	1,920	4 h 55 min	TiN	2.9 µm
CVD	12,500	18 h 30 min	TiCN/Al_2O_3	2.5 µm + 7.5 µm

For the visualization of the main characteristics of the studied deposition processes in terms of energy and material consumption, individual Sankey diagrams were drawn. There, the consumption during different deposition steps in the process can be readily identified as the thickness of the individual arrows corresponds to the respective energy consumption or material contributions.

4. Case Studies

Nowadays a huge variety of coating deposition systems in terms of size and configuration is available on the market. Thus the following case studies exemplify frequently used processes for the deposition of hard coatings.

4.1. Case study 1: Cathodic arc evaporation of TiCN

Fig. 2 represents the energy consumption for the entire CAE process, where the coating step consumes with 52 kWh about half of the total energy of 101 kWh. The consumed energy for heating and etching is similar with 22 and 20 kWh, respectively. In both steps the main contributions are the heaters. The contribution of the cooling step is with about 8 kWh minor.

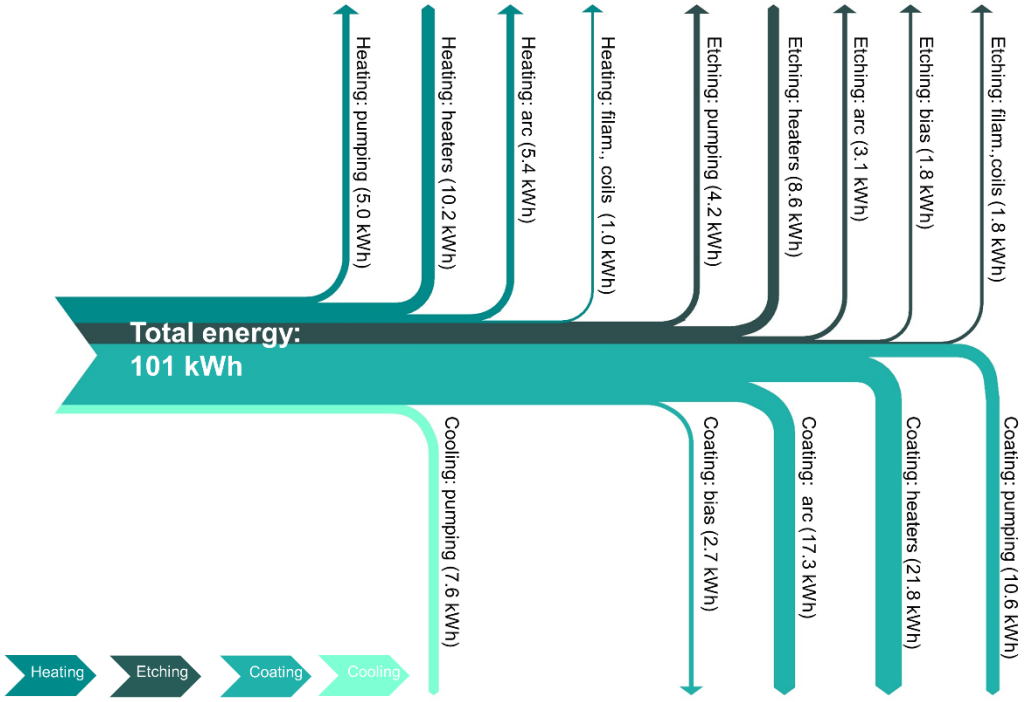

Fig. 2: Energy consumption for the case study 1: Cathodic arc evaporation process. The contributions are divided in the process steps: Heating, Etching, Coating and Cooling.

The material fluxes involved in the CAE process are presented in Fig. 3. The main gas contribution is Ar, which is present during the heating, etching and coating steps. While it is a necessary process gas, Ar is not incorporated in the coating. In fact, the majority of the incoming gases with 1.18×10^{-5} kg·s^{-1} (Ar, C_2H_2 and N_2) are pumped out (outgoing gas (including reactive gases that are incorporated in the coating on the chamber walls and carousel): 1.16×10^{-5} kg · s^{-1}). Considering the flux of solids, a mass

loss of 7.0×10^{-6} kg · s^{-1} for the four Ti targets was determined. The main contribution to the flux of solids are, however, the uncoated (incoming flux) and coated cutting inserts (outgoing flux). From the mass increase of the cutting inserts, the mass of the TiCN coating was calculated to be 7.20×10^{-7} kg · s^{-1}.

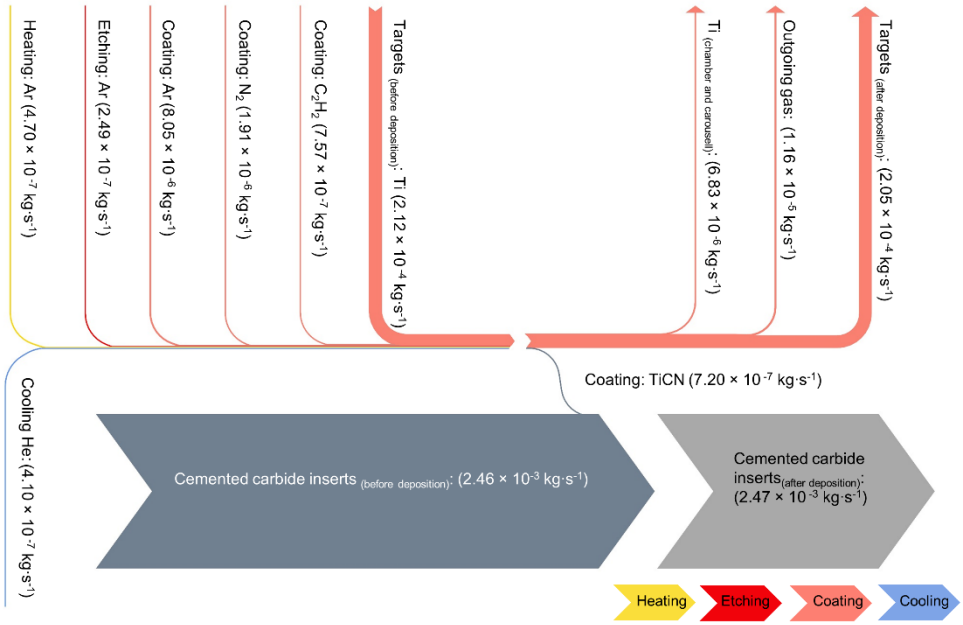

Fig. 3: Material fluxes for the case study 1: Cathodic arc evaporation process. The contributions are divided in the process steps: Heating, Etching, Coating and Cooling.

4.2. Case study 2: Magnetron sputter deposition of TiN

For the exemplary MSD process (see Fig. 4), the total consumed energy sums up to 112 kWh. The coating step consumes with 87 kWh more than three quarters of the total energy from which the consumption by the cathodes amounts to 60 kWh (more than half of the energy of the whole deposition). The contributions of heating (18 kWh), etching (6 kWh) and cooling (1 kWh) are minor.

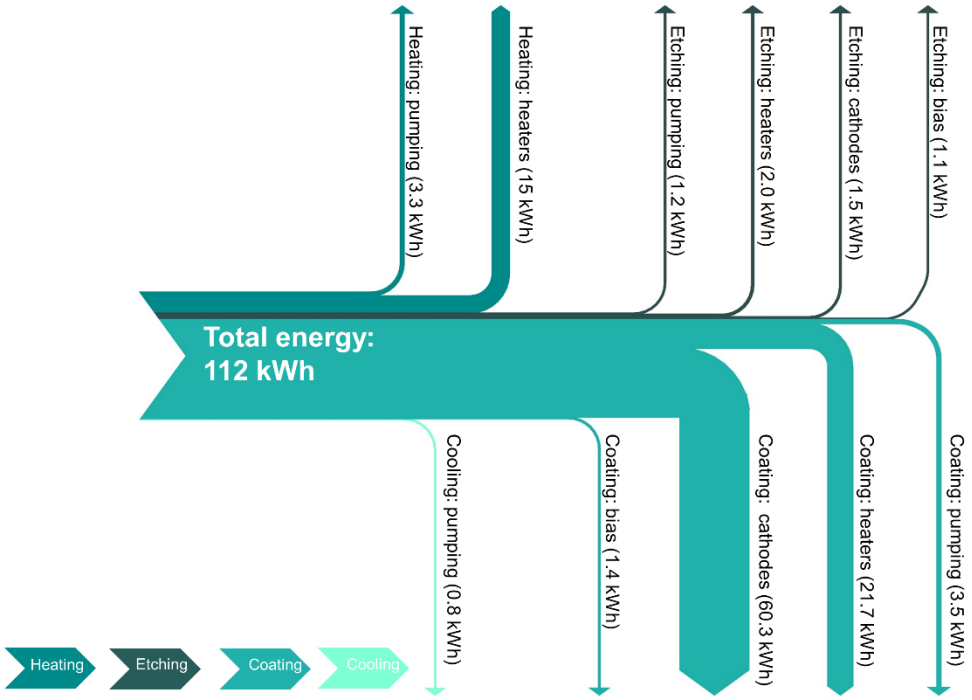

Fig. 4: Energy consumption for the case study 2: Magnetron sputter deposition process. The contributions are divided in the process steps: Heating, Etching, Coating and Cooling.

Fig. 5 shows the material fluxes involved in the MSD process. Similar to the CAE process in case study 1, the main gas flow, which is the Ar flow during etching and coating, is not incorporated in the coating and is directly pumped out. A fraction of the N_2 (9 %) is incorporated in the coating. The solid flux is represented by a mass loss of 1.3×10^{-6} kg· s^{-1} of the four rectangular Ti targets. A large fraction of the total Ti flux is deposited onto the carousel and chamber walls (9.64×10^{-7} kg · s^{-1}). Only 4.36×10^{-7} kg · s^{-1} of the total material flux (i.e., solid and gaseous) is directly incorporated into the coating.

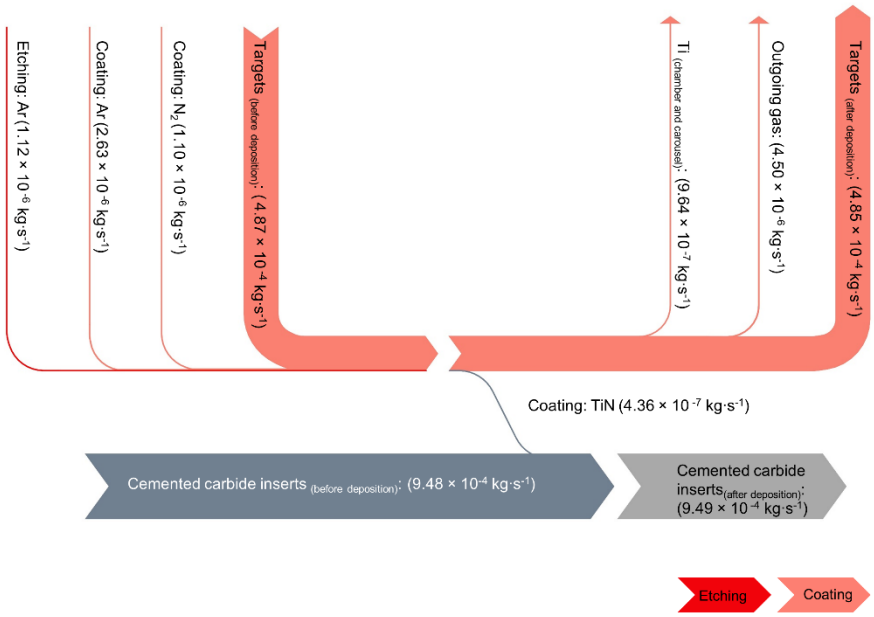

Fig. 5: Material fluxes for the case study 2: Magnetron sputter deposition process. The contributions are divided in the process steps: Etching and Coating.

4.3. Case study 3: Chemical vapor deposition of TiCN/Al_2O_3

The total energy consumption for the studied CVD process (see Fig. 6) sums up to 974 kWh. Within the CVD process, about half of the total energy contributes to the heating step (437 kWh), whereas the coating step accounts for about one third of the consumed energy (326 kWh). In CVD most of the energy during the heating and coating step is consumed by the furnace and auxiliary heaters (394 and 193 kWh, respectively). During the cooling step, energy for the ventilation, pumping and the auxiliary heaters is needed and the consumed energy constitutes 22 % of the total energy.

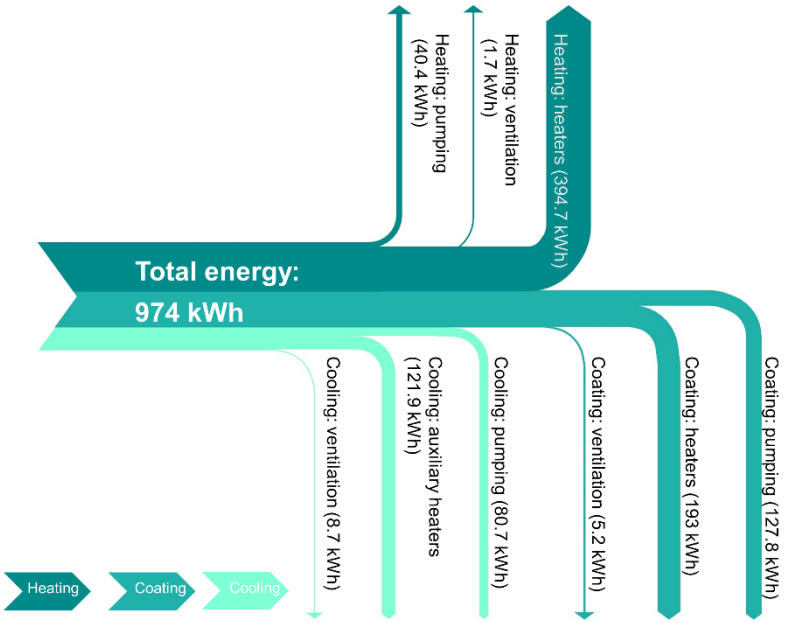

Fig. 6: Energy consumption for the case study 3: Chemical vapor deposition process. The contributions are divided in the process steps: Heating, Coating and Cooling. Scaling factor 1/10 with respect to the CAE and MSD processes.

In the CVD process analyzed, the N_2 flow with 1.99×10^{-4} kg · s^{-1} is the strongest gas flow (see Fig. 7). However, also several other gases have to be taken into account (CH_4, CO_2 and H_2). The total amount of streamed-in gases adds up to 2.99×10^{-4} kg · s^{-1}. Most of them are needed during the coating step as process gas, although they are not incorporated into the coating and leave the process chamber as outgoing gas. The liquid material is for both the incoming and the outgoing fluxes next to the coated and uncoated cemented carbide inserts the most intensive material flux. The water for the neutralization of the reaction products is with 1.05×10^{-3} kg · s^{-1} the main contribution within the liquid fluxes ($TiCl_4$, CH_3CN and NaOH). Al, which is in situ chlorinated, is the only solid material flux (except substrates). The fraction of material incorporated in the coating is 5.26×10^{-6} kg · s^{-1}. The remaining material is deposited onto substrate holders and the reactor wall or leaves the reactor unreacted. Therefore an off gas system is needed for the neutralization of the residual process gases using NaOH and water.

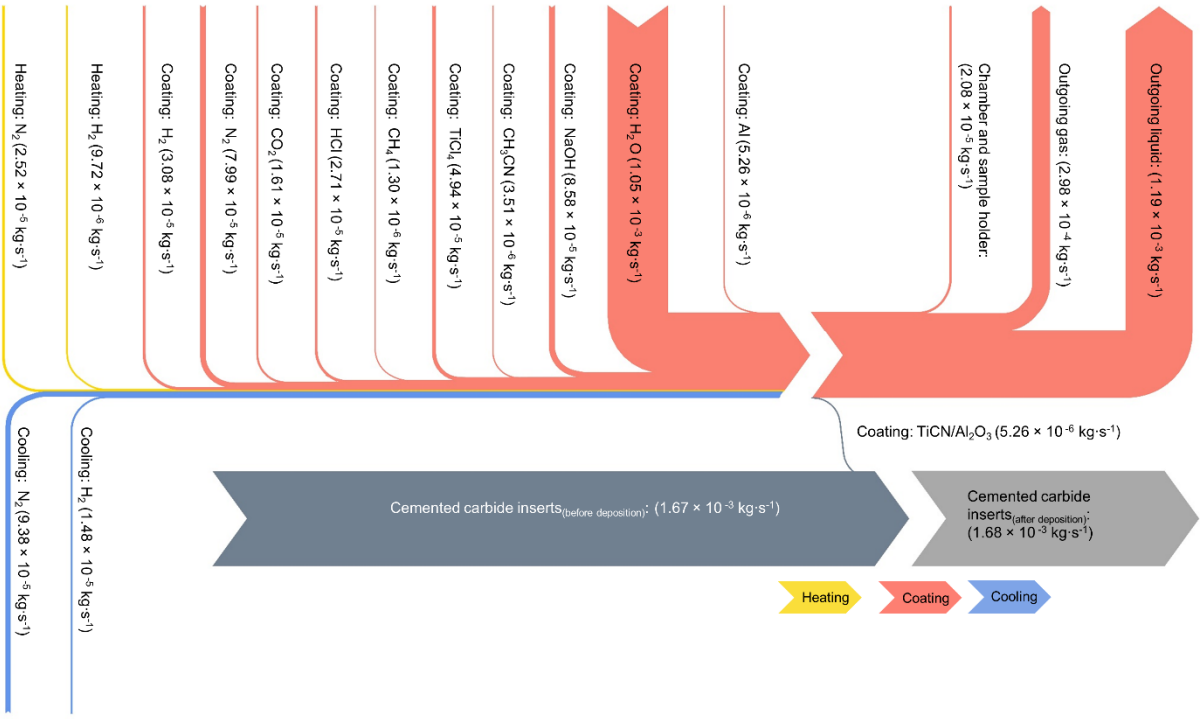

Fig. 7: Material fluxes for the case study 3: Chemical vapor deposition process. The contributions are divided in the process steps: Heating, Coating and Cooling. .

5. Potential use of methodology and indications for further work

Within this work, a concept to quantify the energies and masses involved in PVD and CVD processes of hard coatings on cutting tools was developed and successfully implemented for three case studies. The presented methodology can be applied to analyze and compare different production routes for hard coating materials. In order to do so, a normalization of the energy and mass data with respect to the achieved coating thickness and the sample load of the analyzed process needs to be performed.

In Table 3 the normalized energy contributions stemming from individual process components, e.g. pumps, heaters, cathodes or ventilators are summarized. For the MSD process, the cathodes consumed with 11.1×10^{-3} kWh · (µm · inserts)$^{-1}$ more than one half of the total energy of the process, while in the CAE process, the contribution of the cathodes amounts with 2.96×10^{-3} kWh · (µm · inserts)$^{-1}$ to only about one third of the total energy of the deposition process. In case of the CVD process, the energy needed for the heaters consumed with 5.68×10^{-3} kWh · (µm · inserts)$^{-1}$ nearly three quarters of the total energy used. Similarly, the main energy consumption within CAE is also

due to heating. Looking at the total used energy within the case studies, the energy consumption in the CVD process ($TiCN/Al_2O_3$) is almost one third lower than in the CAE process (TiCN) and even 62 % lower than in the MSD process (TiN). The high normalized energy consumption for the MSD process analyzed is related to the lower sample load of the considered deposition plant compared to the CAE plant (see Table 2). This is even more significant when looking at CVD, where the sample load and applied coating thickness is much higher. While the normalized energy consumption is considerably lower in the CVD process than in the PVD processes, the former is the most mass extensive of the analyzed deposition processes (see Table 4). The total gas consumption in the CVD process is nearly ten times the amount consumed in the PVD processes. In contrast to PVD, there are also liquid components needed in the CVD process, where the NaOH solution and water are necessary for neutralization of the reaction products significantly contributing to the high material flux (total liquid flux 6.34×10^{-4} kg · (µm · inserts)$^{-1}$).

Table 3: Overview of the normalized energy contributions of the deposition processes analyzed.

energy	**case study 1: CAE** **[kWh · (µm · inserts)$^{-1}$]**	**case study 2: MSD** **[kWh · (µm · inserts)$^{-1}$]**	**case study 3: CVD** **[kWh · (µm · inserts)$^{-1}$]**
pumps	3.13×10^{-3}	1.58×10^{-3}	1.99×10^{-3}
heaters	4.64×10^{-3}	6.98×10^{-3}	5.68×10^{-3}
cathodes	2.96×10^{-3}	$11.1. \times 10^{-3}$	-
substrate bias	5.07×10^{-4}	4.47×10^{-4}	-
filament+coils	3.22×10^{-4}	-	-
ventilators	-	-	1.25×10^{-4}
total energy	**11.56×10^{-3}**	**20.06×10^{-3}**	**7.79×10^{-3}**

Based on the total incorporated masses excluding the substrates, the material fraction deposited onto the substrates was calculated (see Table 4). It can be seen that only 0.35 % of the total material throughput involved for the CVD, 3.8 % for CAE and 7.1 % for MSD process are deposited on the substrates. In addition, the process cycle times differ considerably (see Table 2). Since in CVD half of the process time is used for heating and cooling, it is typically used for the deposition of thicker coatings to reduce the energy consumption per µm coating.

Table 4: Overview of the normalized masses actively involved in the deposition processes analyzed. The solid components in the PVD processes (CAE and MSD) are the mass losses of the targets.

mass	**case study 1: CAE** $[kg \cdot (\mu m \cdot inserts)^{-1}]$	**case study 2: MSD** $[kg \cdot (\mu m \cdot inserts)^{-1}]$	**case study 3: CVD** $[kg \cdot (\mu m \cdot inserts)^{-1}]$
gaseous components	1.68×10^{-5}	1.54×10^{-5}	1.59×10^{-4}
liquid components	-	-	6.34×10^{-4}
solid components	9.91×10^{-6}	4.13×10^{-6}	2.80×10^{-6}
total mass	$\mathbf{2.67 \times 10^{-5}}$	$\mathbf{1.96 \times 10^{-5}}$	$\mathbf{79.5 \times 10^{-5}}$
fraction incorporated into coating	**3.8 %**	**7.1 %**	**0.35 %**

Looking ahead, there are several aspects that still need to be considered before different deposition techniques can be compared objectively. The case studies presented here were single events, but more appropriate would be to compare typical processes of the respective deposition technique. This means an averaging over a sufficiently high number of single processes should be performed and further details would need to be considered. In the case of the PVD processes, e.g. the limited target or cathode utilization needs to be taken into account, which increases the average mass loss of the targets that is not incorporated into the coating.

Further adjustments to the energy consumption and mass fluxes can be made by considering possibilities of material recycling and energy recovery. This could be, e.g., the recycling of target materials for the PVD processes or worn cutting inserts to be reused in the production of new tools, which would be applicable to PVD and CVD. In addition, integration of a heat exchange module for waste heat recovery as additional part of the coating system might open a way to decrease their energy demand. If a comparison of different coating materials is desired, then it is advisable to include the coating performance as another normalization step of the data. Such a normalization could even be of interest, if the same coating material but different deposition techniques are compared.

6. Conclusions

Within this work, a concept to quantify the energies and masses involved in the deposition of hard coatings on cutting tools by PVD and CVD methods was developed and successfully implemented for three case studies, i.e. cathodic arc evaporation, magnetron sputter deposition and thermally activated CVD. The thorough determination of relevant process parameters describing the consumption of solid, liquid and gaseous masses as well as the energy needed to run the deposition process enables the visualization of energy consumption and mass fluxes of the whole deposition process by Sankey diagrams. While a basic evaluation of the individual deposition processes itself is possible by normalization per coated tool and coating thickness, a global comparison requires consideration of additional input parameters like target utilization, tool performance and recycling issues. For the future, the presented concept could contribute to a sustainable further development of deposition processes and coated tools, as it allows to identify possibilities to safe energy and material.

7. Acknowledgements

The authors gratefully acknowledge the financial support of the Christian Doppler Society, the Österreichische Forschungsförderungsgesellschaft FFG (grant number 845255) and PLANSEE Composite Materials GmbH, Lechbruck, Germany.

8. References

[1] P.H. Mayrhofer, C. Mitterer, L. Hultman, H. Clemens, Microstructural design of hard coatings, Prog. Mater. Sci. 51 (2006) 1032–1114.

[2] B. North, Six issues for the hard coatings community, Surf. Coatings Technol. 106 (1998) 129–134.

[3] Handbuch der Gewindetechnik und Frästechnik EMUGE-Franken, EMUGE-Franken, Erlangen, 2004.

[4] H. Holzschuh, Verschleißschutzschichten in der Werkzeugindustrie, in: Pulvermetallurgie für Hochpräzise Bauteile und dichte Hochleistungswerkstoffe, Fachverband Pulvermetallurgie, Hagen, 2007.

[5] H.P.R. Sankey, Minutes of Proceedings of the Institution of Civil Engineers, Minutes Proc. Inst. Civ. Eng. 125 (1896) 182–242.

[6] H.P.R. Sankey, Introductory Note on the Thermal Efficiency of Steam-Engines, Minutes Proc. Inst. Civ. Eng. 134 (1898) 278–283.

[7] A. Riedler, S. Löffler, Energiefluss der Maschine, in: Oelmaschinen, Berlin, 1916: pp. 124–127.

[8] G. Kalt, Biomass streams in Austria: Drawing a complete picture of biogenic material flows within the national economy, Resour. Conserv. Recycl. 95 (2015) 100–111.

[9] E. Curmi, K. Richards, R. Fenner, J.M. Allwood, G.M. Kopec, B. Bajželj, An integrated representation of the services provided by global water resources, J. Environ. Manage. 129 (2013) 456–462.

[10] J.M. Cullen, J.M. Allwood, Theoretical efficiency limits for energy conversion devices, Energy. 35 (2010) 2059–2069.

[11] R.F. Bunshah, J.M. Blocher, T.D. Bonifield, J.G. Fish, B.E. Jacobson, D.M. Mattox, et al., Deposition Technologies for Films and Coatings, Noyes Publications, New Jersey, 1982.

[12] A. Anders, Cathodic arcs: From fractal spots to energetic condensation, Springer, New York, 2008.

[13] M. Rebelo de Figueiredo, J. Neidhardt, R. Franz, C. Mitterer, Low-friction mechanisms active for carbon containing coatings: Ti-C-N as a model system, Berg- und Hüttenmännische Monatshefte. 153 (2008) 263–267.

[14] R.F. Bunshah, S.M. Rossnagel, Handbook of Hard Coatings, Deposition Techonologies, Properties and Applications, Noyes Publications, New Jersey, 2001.

[15] K.-P. Müller, Praktische Oberflächen-Technik, vorbehandeln, beschichten, prüfen, 3. Auflage, Vieweg, Braunschweig, 1999.

[16] N. Schalk, T. Weirather, C. Polzer, P. Polcik, C. Mitterer, A comparative study on $Ti_{1-x}Al_xN$ coatings reactively sputtered from compound and from mosaic targets, Surf. Coat. Technol. 205 (2011) 4705–4710.

[17] H.O. Pierson, Handbook of chemical vapor deposition (CVD), Park Ridge: Noyes Publications, 1999.

[18] E. Kübel, New developments in chemically vapor-deposited coatings from an industrial point of view, Surf. Coatings Technol. 49 (1991) 268–274.

[19] N. Schalk, C. Mitterer, C. Czettl, B. Sartory, M. Penoy, C. Michotte, Dry-blasting of α- and κ-Al_2O_3 CVD hard coatings: Friction behaviour and thermal stress relaxation, Tribol. Lett. 52 (2013) 147–154.

[20] S. Ruppi, Advances in chemically vapour deposited wear resistant coatings, Le J. Phys. IV. 11 (2001) 847–859.

[21] U. Schleinkofer, C. Czettl, C. Michotte, Coating Applications for Cutting Tools, in: Comprehensive Hard Materials, Volume 1, Elsevier, Oxford, 2014: pp. 453–469.

[22] R. Bonetti, H. Widprächtiger, E. Mohn, CVD of titanium carbonitride at moderate temperature: Properties and applicaton, Met. Powder Rep. 45 (1990) 837–840.

[23] C. Czettl, C. Mitterer, C. Michotte, M. Penoy, M. Kathrein, Homogeneity of industrial scale thermal CVD processes for TiCN hard coatings, in: 17th Int. Plansee Semin., 2009: pp. HM71/1–8.

[24] C. Czettl, C. Mitterer, U. Mühle, D. Rafaja, S. Puchner, H. Hutter, et al., CO addition in low-pressure chemical vapour deposition of medium-temperature TiC_xN_{1-x} based hard coatings, Surf. Coat. Technol. 206 (2011) 1691–1697.

[25] C. Mitterer, PVD and CVD Hard Coatings, in: Comprehensive Hard Materials, Volume 2, Elsevier, Oxford, 2014: pp. 449–467.

[26] D.M. Mattox, Handbook of Physical Vapor Deposition (PVD) Processing, Second edition, Oxford, 2010.

[27] W.D. Westwood, Sputter Deposition, AVS, New York, 2003.

[28] R.A. Haefer, Oberflächen- und Dünnschicht-Technologie, Springer-Verlag, Berlin, 1987.

Publication II

Influence of Ar ion etching on the surface topography of cemented carbide cutting inserts

M. Gassner, N. Schalk, B. Sartory, M. Pohler, C. Czettl, C. Mitterer

International Journal of Refractory Metals & Hard Materials 69 (2017)

234–239

Influence of Ar ion etching on the surface topography of cemented carbide cutting inserts

Martina Gassner[1], Nina Schalk[1], Bernhard Sartory[2], Markus Pohler[3], Christoph Czettl[3], Christian Mitterer[1]

[1] Department of Physical Metallurgy and Materials Testing, Montanuniversität Leoben, Franz-Josef-Straße 18, 8700 Leoben, Austria

[2] Materials Center Leoben Forschung GmbH, Roseggerstraße 12, A-8700 Leoben, Austria

[3] CERATIZIT Austria GmbH, Metallwerk-Plansee-Straße 71, 6600 Reutte, Austria

Abstract:

In situ substrate cleaning by ion etching prior to physical vapor deposition of hard coatings alters topography and composition of the surface to be coated. Within this work, the influence of Ar ion etching on the surface topography of cemented carbide cutting inserts with different geometries was investigated. The surface of cutting inserts before and after ion etching was evaluated by different scanning electron microscopy techniques to illuminate the effect of ion etching on both, the cutting edges and the flat surface. Additionally, profilometric measurements were carried out to determine changes of the surface roughness and to quantify the removed material by measuring the step height between the etched and un-etched surface. Surface roughness and thickness of the removed layer increased with etching time at constant bias voltage, while the applied voltage had only a minor influence. In addition, energy-dispersive X-ray spectroscopy mappings indicated changes of the surface composition by ion etching due to preferential sputtering of the cobalt binder phase.

Keywords: ion etching, cemented carbide, PVD, cutting inserts, hard coating

1. Introduction

Hard coatings grown by physical vapor deposition (PVD) are state-of-the-art for many industrial applications, for example to improve the performance and lifetime of cutting tools. In order to achieve sufficient adhesion between substrate and coating, mechanical, chemical and/or physical pretreatments of the substrates, such as grinding, sand-blasting, chemical and ultrasonic cleaning are necessary to remove surface contaminations caused by manufacturing as well as follow-up handling [1]. Substrate cleaning by ion etching* is another frequently used possibility to remove contaminations as well as surface oxides by physical sputtering and is typically applied in addition to one of the pretreatments mentioned above. The main advantage of surface cleaning by ion etching is that it is done *in situ* within the vacuum chamber immediately prior to coating deposition [3]. Due to its practicability and easy implementation into the PVD system and process used, it has evolved as the standard method for the deposition of well adherent hard coatings [4]. Generally, two different approaches are applied: inert gas ion etching using predominantly Ar and metal ion etching, e.g. using Cr ions [5,6]. Substrate surface cleaning by bombarding with energetic ions alters its surface chemistry, topography, microstructure and morphology by impulse and momentum transfer, causing sputtering of surface atoms, formation of defects in the surface near zone of the substrate, substrate heating, desorption of volatile species and implantation of energetic ions. While for Ar ion etching implanted Ar atoms constitute an undesired impurity in the substrate material, implanted Cr is considered as less harmful [7]. Preferential sputtering of multi-component materials may result in changes of surface composition and morphology [5,3]. Further, Ar ion etching at high substrate bias voltages and consequently high kinetic energy could lead to formation of a low density substrate surface region providing additional nucleation sites for film growth. There, randomly oriented grains nucleate, which promotes competitive growth and formation of fibrous columns separated by open grain boundaries, leading to low hardness of the coating and thus decreased tool performance and life time [3,7]. In contrast, Cr ion etching at high bias voltages has been reported to foster local epitaxial growth caused by Cr implantation [7]. Long exposure times to energetic ions - especially using metal ion etching on small tools - may lead to local substrate overheating depending on the tool

* According to [115], the term ion etching is used for the ion-assisted *in situ* cleaning process applied before the physical vapor deposition of coatings and thin films. In contrast, the term sputtering summarizes the physical mechanisms of ion-bombardment induced material removal from the surface of bombarded solids. Within this report, we follow this definition.

geometry [8]. The crucial regions of cutting tools are their cutting edges, where during etching (and also during coating deposition) increased ion flux densities compared to a flat surface occur, thus considerably affecting the properties of the edge region. However, the majority of the available literature concentrates on ion etching and subsequent coating deposition on flat substrates [9].

Thus, the present work focuses on Ar ion etching of cemented carbide cutting inserts to provide insights into bombardment-induced surface modifications. For different etching times and substrate bias voltages, the changes in surface topography of cemented carbide substrates and the geometry of the cutting edges were investigated in detail by scanning electron microscopy, energy-dispersive X-ray spectroscopy and profilometry. The observed changes are then related to modifications of the surface due to preferential sputtering of the cobalt binder phase of the cemented carbide inserts.

2. Experimental details

Etching by Ar ion bombardment of cemented carbide substrates was carried out in an industrial-scale Oerlikon Balzers Innova cathodic arc evaporation system using cutting inserts according to ISO 1832 in CCGT 120402FN-27 (see Fig. 1) and SNUN 120312EN geometry.

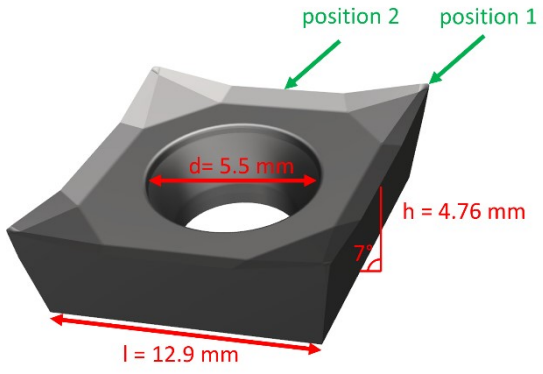

Fig. 1: Cutting insert in CCGT 120402FN-27 geometry. Dimensions: insert shape: rhombus 80°; clearance angle 7°, 12.9 mm cutting edge length, 4.76 mm insert thickness; 0.2 mm nose radius; cutting edge: sharp, cutting direction: two-sided. The two positions investigated are indicated by arrows.

The chemical composition was 94 wt% tungsten carbide, 6 wt% cobalt for the CCGT and 92 wt% tungsten carbide, 2 wt% mixed carbides and 6 wt% cobalt for the SNUN inserts. Prior to ion etching,

the CCGT substrates were ground on the flank face and ground and polished on the rake face according to industrial standards for cutting inserts, while the SNUN substrates were ground and polished on the rake face using a diamond suspension with a grain size of 1 µm. The inserts were mounted on representative positions on the substrate carrousel, enabling twofold rotation for the SNUN and threefold rotation for the CCGT inserts. The rotation of the sample holder during ion etching leads to a permanent variation of the angle of incident Ar ions impinging on the surfaces of the substrate. To achieve etching conditions relevant to industrial processes, the remaining positions were filled with dummy substrates. For the determination of the material removed by ion etching, a fraction of the surface of each SNUN insert was covered with a stainless steel platelet. Ion etching was done at a substrate temperature of 350 °C and an Ar pressure of ~2×10^{-3} mbar. The etching was performed in pure Ar plasma by applying a negative bias voltage to the substrate carousel. The process time was varied from 25 to 55 and 85 min, including a ramp-up time of 5 min for reaching the desired bias voltage and for igniting the plasma. Thus, the respective etching times with constant discharge conditions were 20, 50 and 80 min. A bias voltage of -185 V was applied for all etching times. Additional processes with -170 and -200 V were performed for a duration of 50 min.

For comparison with the ion etched condition, a ~4.0 µm thick TiAlN-based coating was deposited by cathodic arc evaporation in the same Oerlikon Balzers Innova system, following the approach reported by Pfeiler et al. [10]. Prior to deposition, the inserts were Ar ion etched for 50 min at a bias voltage of -185 V. Coating deposition was done in pure nitrogen atmosphere at a pressure of 3.2×10^{-2} mbar. The bias voltage was set to -40 V, the deposition time was 140 min and the substrate temperature ~550 °C.

All samples were investigated using a Zeiss Auriga Crossbeam field emission gun scanning electron microscope (FEG-SEM). 3D images were calculated by triple image photogrammetry applying the Alicona MeX software, using three SEM images collected with the secondary electron detector at different tilt angles (i.e., 35, 40 and 45°). An EDAX Apollo 40+ detector was utilized for the energy-dispersive X-ray spectroscopy (EDX) measurements. Roughness and step height on SNUN substrates were determined applying a Leica DCM 3D interferometer and confocal microscope.

3. Results

In Fig. 2a-f, SEM images of the flat surfaces of SNUN inserts in the polished condition and after ion etching for different times and at different bias voltages are displayed. Prior to ion etching, scratches stemming from surface preparation are present and the individual carbide grains can hardly be distinguished (see Fig. 2a). The etching process leads on the one hand to a decrease of density and depth of these scratches. On the other hand, after 20 min of etching, the edged carbide grains can be clearly distinguished compared to the un-etched sample (see Fig. 2a and b). This effect becomes more pronounced with etching time and the surface gains roughness, most probably due to preferential sputtering (see Fig. 2a, b, d and f). The variation of the bias voltage slightly affects the appearance of the surface, where especially the highest voltage applied results in a ragged topography (compare Fig. 2c-e).

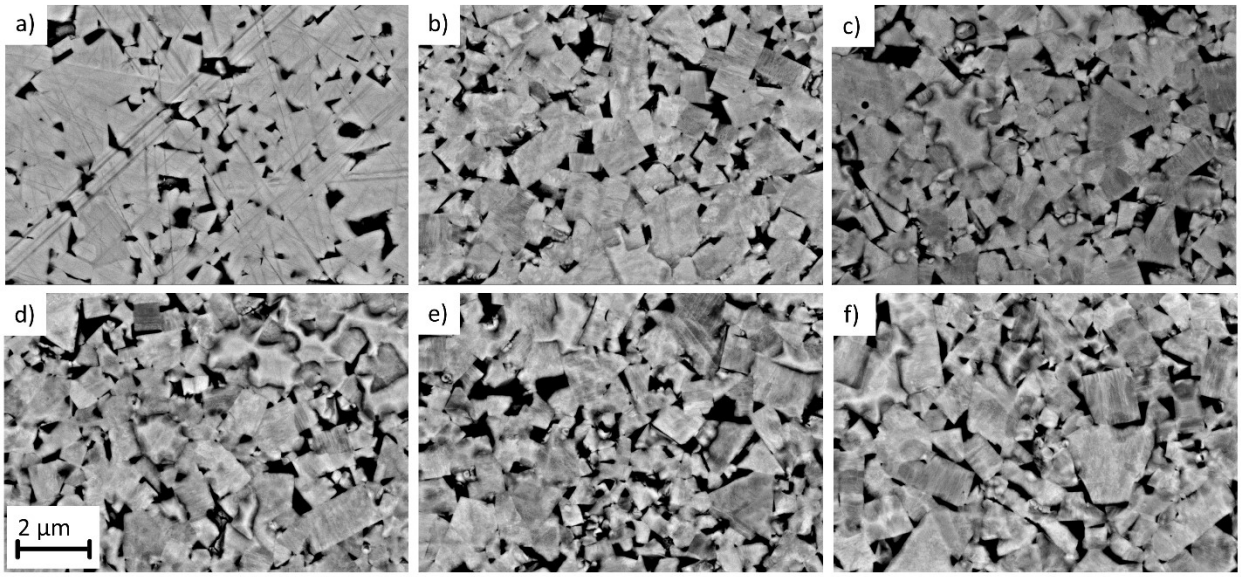

Fig. 2: Back-scattered electron SEM images the surface of cemented carbide substrates in SNUN geometry a) prior to ion etching and after ion etching for b) 20 min at -185 V, c) 50 min at -170 V, d) 50 min at -185 V, e) 50 min at -200 V, and f) 80 min at -185 V.

For the characterization of the influence of ion etching on the cutting edges, the positions marked in Fig. 1 on the CCGT insert, i.e. the nose of the cutting edge (position 1) and a side position (position 2 in the center of the cutting edge), were investigated by SEM. Fig. 3a shows a 3D SEM image of position

1 before etching. At this point it has to be mentioned that the appearance of the cutting edge can already be significantly affected by handling of the insert during grinding and polishing and care was taken within this work to prepare all samples investigated in the same way. The flank as well as the rake faces of the insert show scratches caused by preparation, which are clearly seen in the SEM image in Fig. 3b. Directly at the cutting edge, individual tungsten carbide grains may be distinguished, in contrast to the flat surface on the rake and flank face. Comparing the 3D images of the un-etched and the etched insert (see Fig. 3a and c), it is obvious that the surface has changed considerably. After ion etching, the scratches are not visible anymore (see Fig. 3b and d) and the individual grains at the edge and the edge itself appear blunter. On the flank face it seems that some grains, most probably tungsten carbide grains, protrude out of the surface (see Fig. 3d), which could be due to preferential sputtering of the surrounding cobalt binder areas.

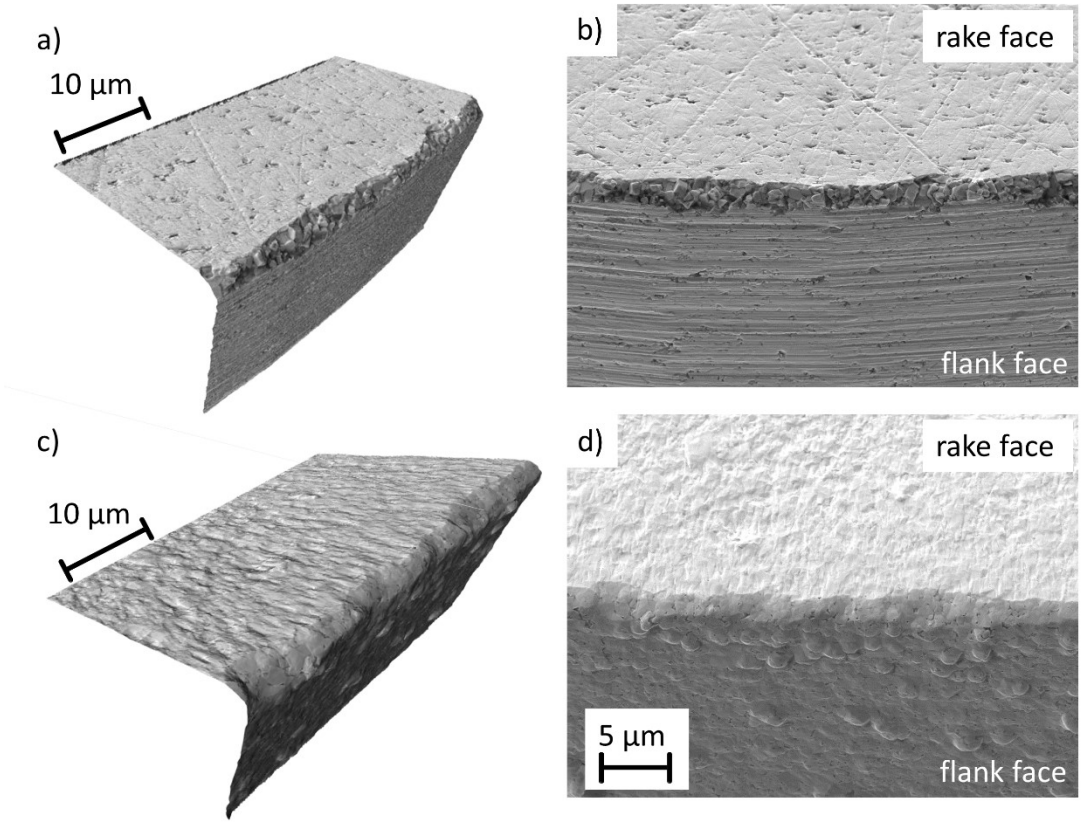

Fig. 3: Secondary electron SEM images of the cutting edge (position 1) of the cemented carbide inserts in CCGT geometry. 3D images of a) the un-etched and c) the insert ion etched for 80 min at -185 V. SEM images of b) the un-etched cutting insert and d) the insert ion etched for 80 min at -185 V.

Fig. 4a and c represent a 3D overview of the positions 1 and 2 after 20 min of etching at a substrate bias of -185 V. It is obvious that the effect of ion etching is more pronounced at the nose (position 1) than at the side of the cutting edge (position 2); the nose appears more rounded and blunter. Having a closer look on the SEM images of position 1 and 2, presented in Fig. 4b and d, respectively, scratches caused by grinding and polishing are still present, clearly visible on the flank phase and more pronounced for position 2 than for position 1, as evidenced by Fig. 4d. Further, some carbide grains on the edge are already partially etched off, which seems to be more pronounced at the nose (position 1, Fig. 4b) than at the side of the cutting edge (position 2, Fig. 4d). These observations corroborate the assumption that ion etching induced sputtering is more distinct on the most exposed areas of the insert. This is attributed to the concentration of the electrical field lines to exposed areas, which results in a higher local ion current density during etching leading to higher local temperatures and more pronounced material removal by sputtering [11,12].

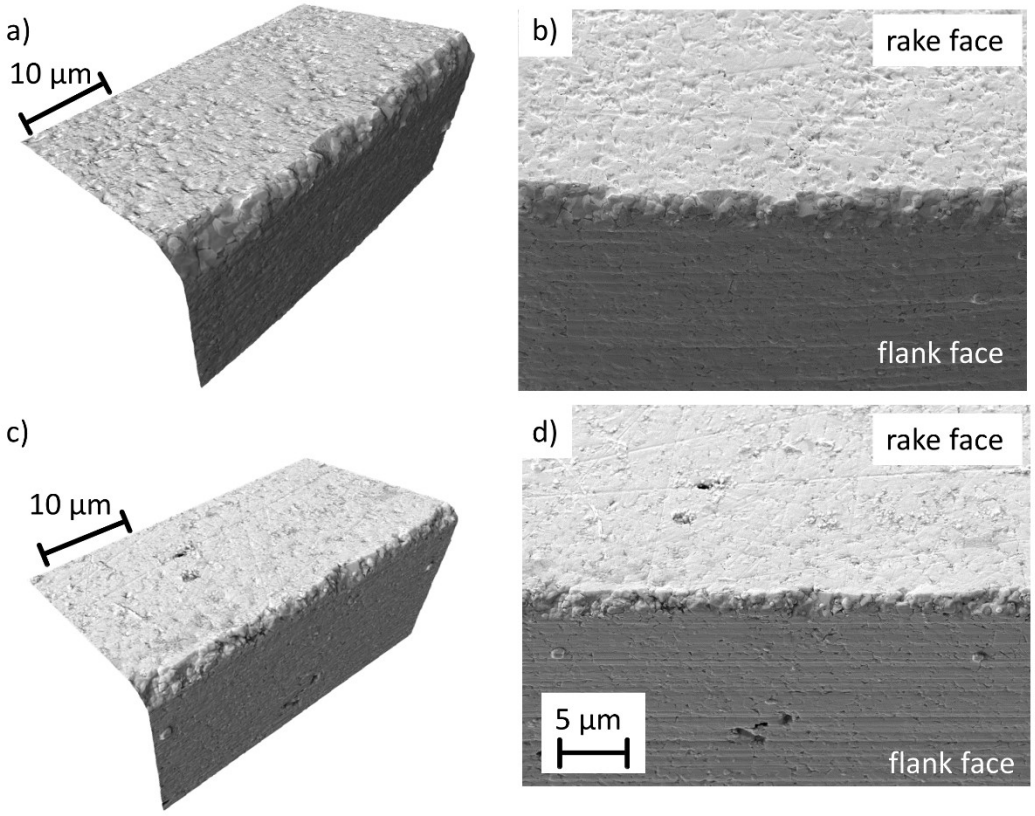

Fig. 4: Secondary electron SEM images of the cutting edge of the cemented carbide inserts in CCGT geometry after 20 min of ion etching at -185 V. 3D image of a) position 1 and c) position 2. SEM image of b) position 1 and d) position 2.

The etching efficiency has been quantified by measuring the step height between the etched and un-etched surface area of SNUN inserts and is summarized in Fig. 5a for all etching processes studied. The thickness of the removed layer increases almost linearly with time from 220 nm for 20 min to 930 nm for 80 min. Increasing the bias voltage at an etching time of 50 min results in a material removal increased by ~30 % for -185 V and by ~80 % for -200 V compared to -170 V. The etching rate, i.e. the thickness of the removed layer per time, raises with increasing voltage from ~7 to ~12 nm/min, whereas the etching rate for all samples treated at -185 V is rather constant at 8 ± 1 nm/min.

Complementary to the SEM investigations, profilometric measurements on SNUN substrates were performed to obtain the arithmetical surface area roughness (S_a) presented in Fig. 5b. The S_a values obtained for the polished sample agree with ~8 nm well to those presented in [1,13]. S_a increases with etching time at a bias voltage of -185 V from an initial value (after polishing) of ~8 nm up to ~31 nm for the surface treated for 80 min. These changes are in good agreement with the already mentioned surface changes observed by SEM and with the common roughness increase as a result of preferential sputtering of polycrystalline materials due to sputtering reported in literature [14]. The influence of the voltage on the roughness lies within the scattering of the S_a values and is thus only of minor significance.

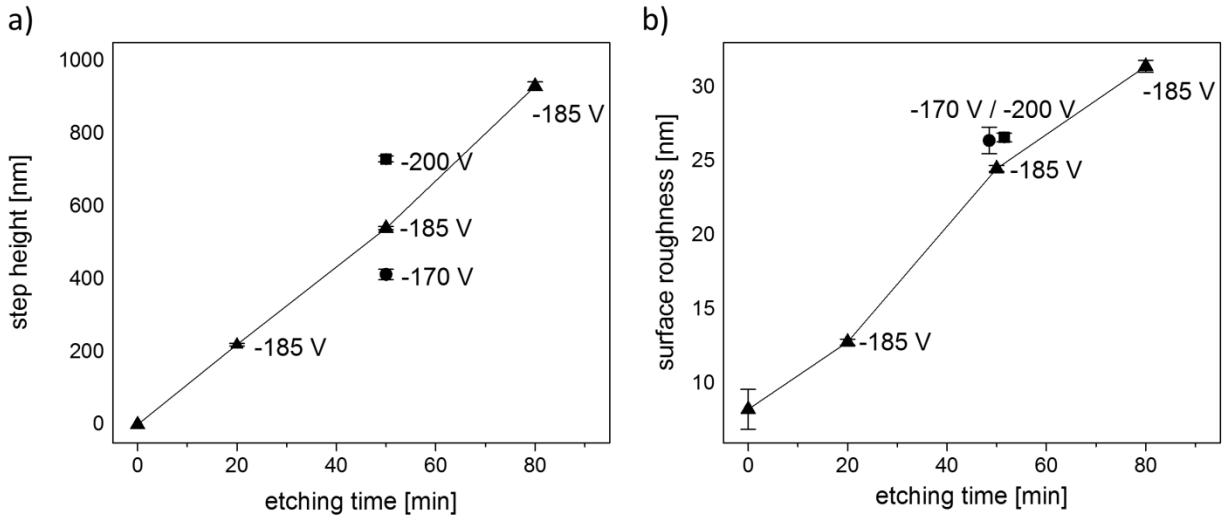

Fig. 5: a) Step height between the etched and the un-etched polished surface of the SNUN insert. b) Arithmetical surface area roughness S_a measured on SNUN inserts before and after ion etching with different times and bias voltages.

Fig. 6 presents 3D images of a cutting insert in CCGT geometry coated with a TiAlN-based hard coating to illustrate the contribution of the applied coating on blunting of the cutting edges. There, position 1 (see Fig. 6a) on the nose appears blunter than position 2 (see Fig. 6b), which agrees well to the observations on the uncoated inserts after etching. Comparing the uncoated and the coated inserts, the observed blunting effect on the edge of the coated tool increased. Further, the presence of randomly distributed macro-droplets typical for cathodic arc evaporation processes [15] contributes significantly to the blunting of the cutting edge.

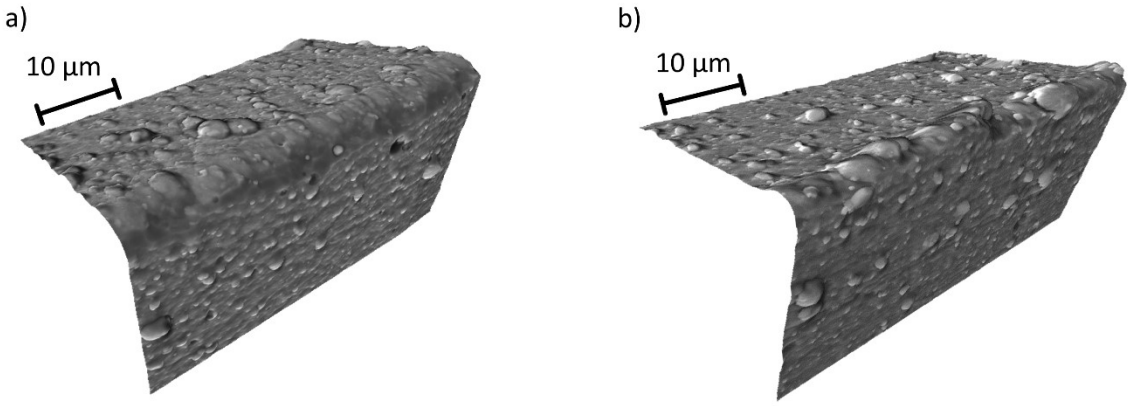

Fig. 6: 3D secondary electron SEM images of the cutting edge of a coated cemented carbide insert in CCGT geometry. a) position 1 b) position 2.

4. Discussion

Cleaning of cemented carbide substrates by Ar ion bombardment not only alters their surface topography, as already demonstrated by the observed changes in surface roughness (see Fig. 5), but also results in changes of the surface composition. This is corroborated by the EDX element mapping presented in Fig. 7.

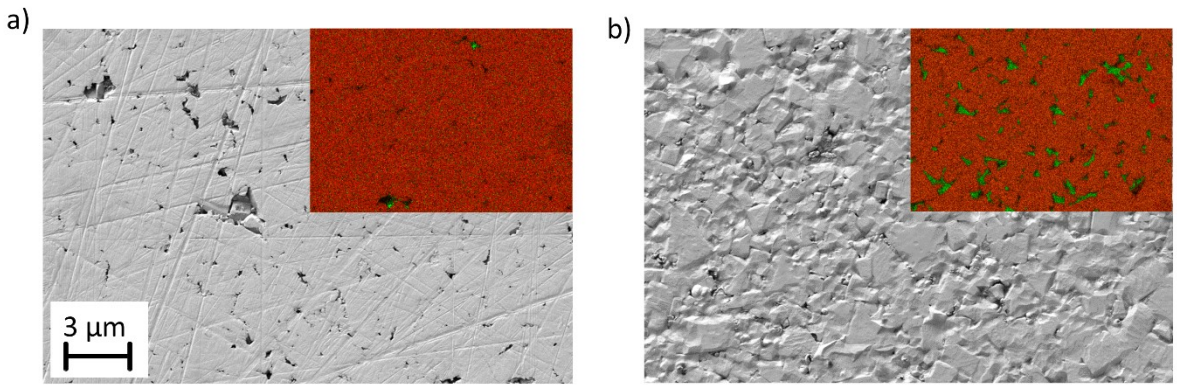

Fig. 7: Secondary electron SEM image of the SNUN substrates partially superimposed by an EDX elemental map, where the red sections represent WC and the green sections Co. a) After polishing, before etching and b) after etching at -185 V for 80 min.

After grinding and polishing, the cobalt binder between the carbide grains can only hardly be detected (see Fig. 7a). Essentially, cobalt seems to be only present within a few randomly distributed local defects, where most probably a carbide grain was mechanically removed during grinding and polishing. According to the existing literature, the absence of cobalt can be attributed to the following reasons: the pronounced surface deformation of the soft cobalt binder phase or so-called micro-cutting processes during grinding and polishing, where material is removed and the surface is plastically deformed [16–21]. In summary, the cobalt binder phase, which is considerably softer than the hard carbide phases, can be easily polished away and is thus only present within local areas below the surface of the cemented carbide, as outlined in the schematic in Fig. 8a [16].

Fig. 8: Scheme of a) the cemented carbide substrate after polishing and b) the polished cemented carbide substrate after ion etching. The arrows indicate the removal of material by Ar ion etching.

While consequently the cobalt binder is only visible locally within the EDX mapping in Fig. 7, the presence of very thin layers, not detectable by EDX, smeared over the surface during polishing cannot be excluded. This effect is known from literature as surface flow, where a thin film is formed by mobile solid species stemming from the material to be polished and from the polishing agent. This film is restrained similar to a liquid filling surface grooves and pits [22]. Furthermore, grinding is reported to lead to deformation of tungsten carbide grains covered by a deformed surface layer with low concentration of cobalt and a thickness of up to 500 nm [13]. Such surface layers stemming from grinding and polishing can be assumed to be completely removed by Ar ion etching at -185 V for more than 50 min, as evidenced by the measured step height between the etched and un-etched surface (see Fig. 5a).

In the SEM images of the etched SNUN substrates in Fig. 2b-f, the tungsten carbide grains can be easily distinguished. In contrast to the polished substrate before ion etching, also the cobalt binder phase is clearly visible and regularly distributed on the surface (see Fig. 7b). Ar ion etching is assumed to lead to a blunter appearance of the carbide grains, as schematically demonstrated by Fig. 8b, since after removal of the cobalt binder phase they are exposed to intense ion bombardment. This assumption is fostered by the differing sputter yield of tungsten and cobalt, which is defined as the number of atoms removed per incoming ion. In general, the sputter yield depends on the energy, the angle of incidence and the mass of the bombarding ions as well as on the material to be bombarded [5,23]. Within the ion energy range of 30 to 600 eV, a nearly linear raise of the sputter yields is reported for Ar ions, with values of 0.3 at 200 eV and 0.6 at 600 eV for tungsten. In contrast, the sputter yield reported for cobalt is 0.6 (at 200 eV) and 1.4 (at 600 eV) [5]. Thus, for Ar ion sputtering it can be concluded that cobalt is removed twice as efficiently as tungsten. The different sputter yields result in an irregular topography of the chemically inhomogeneous surface of a cemented carbide. This interpreation is corroborated by Fig. 5b, evidencing an increasing surface roughness due to preferential sputtering with rising etching time. The change in surface topography is also visible in the SEM images presented in Fig. 2b-f and in Fig. 4. Besides the changing surface topography, a further consequence of preferential sputtering is an altered surface composition. The preferential sputtering of cobalt results in a fast removal of smeared cobalt layers eventually formed during polishing and of the cobalt binder phase between the carbide grains, as demonstrated in Fig. 8b. Consequently, after prolonged bombardment the surface is enriched in carbides, which are then more efficiently sputtered compared to the cobalt hidden between the carbide grains [24]. This assumption is

corroborated by the improved visibility of cobalt islands surrounded by blunter carbide grains, as evidenced in Fig 7b.

5. Conclusions

Within this work, cemented carbide inserts were Ar ion etched for various etching times at different bias voltages. Ion etching prior to the deposition of hard coatings leads to a change in topography as well as chemical composition of the surface of the cemented carbide substrates. Both, surface roughness and thickness of removed layer increase with etching time. Also the increasing bias voltage results in a rise of the removed layer thickness; however, only a minor change in surface roughness could be observed. Special emphasis was also laid on ion bombardment induced changes of the cutting edges. The noses of the cutting inserts being exposed to intense ion bombardment became blunter compared to less exposed positions of the cutting edge. The observed changes in chemical composition and topography are related to preferential sputtering of cobalt. In conclusion, this study contributes to the understanding of ion bombardment induced changes of surface composition and topography of both, the flat and the crucially exposed areas of cemented carbide inserts. The experimental approach and the observed findings might contribute to the optimization of ion etching processes for tools with fragile geometries like drills for printed circuit boards or sharp inserts for grooving and parting.

6. Acknowledgements

Financial support of the Österreichische Forschungsförderungsgesellschaft FFG (grant number 851894) is gratefully acknowledged.

7. References

[1] W. Schedler, Hartmetall für den Praktiker, VDI-Verlag GmbH, Düsseldorf, 1988.

[2] D.M. Mattox, Ion Plating Technology, in: Depos. Technol. Film. Coatings, Noyes Publ., New Jersey, 1982.

[3] R.F. Bunshah, S.M. Rossnagel, Handbook of Hard Coatings, Deposition Techonologies, Properties and Applications, Noyes Publications, New Jersey, 2001.

[4] E. Taglauer, Surface cleaning using sputtering, Appl. Phys. A. 51 (1990) 238–251.

[5] R.F. Bunshah, J.M. Blocher, T.D. Bonifield, J.G. Fish, B.E. Jacobson, D.M. Mattox, et al., Deposition Technologies for Films and Coatings, Noyes Publications, New Jersey, 1982.

[6] C. Schönjahn, M. Bamford, L.A. Donohue, D.B. Lewis, S. Forder, W.D. Münz, The interface between TiAlN hard coatings and steel substrates generated by high energetic Cr^+ bombardment, Surf. Coat. Technol. 125 (2000) 66–70.

[7] C. Schönjahn, D.B. Lewis, W.D. Münz, I. Petrov, Substrate ion etching in combined steered cathodic arc–ubm deposition system: effects on interface architecture, adhesion, and tool performance, Surf. Eng. 16 (2000) 176–180.

[8] C. Schönjahn, A.P. Ehiasarian, D.B. Lewis, R. New, W.D. Münz, Optimization of in situ subtrate surface treatment in a cathodic arc plasma: A study by TEM and plasma diagnostics, J. Vac. Sci. Technol. A. 19 (2001) 1415–1420.

[9] E.B. Macak, W.D. Münz, J.M. Rodenburg, Electron microscopy studies of hard coatings deposited on sharp edges by combined cathodic arc / unbalanced magnetron PVD, Surf. Coat. Technol. 152 (2002) 349–354.

[10] M. Pfeiler, G.A. Fontalvo, J. Wagner, K. Kutschej, M. Penoy, C. Michotte, et al., Arc evaporation of Ti-Al-Ta-N coatings: The effect of bias voltage and Ta on high-temperature tribological properties, Tribol. Lett. 30 (2008) 91–97.

[11] G. Nayal, D.B. Lewis, M. Lembke, W.D. Münz, J.E. Cockrem, Influence of sample geometry on the effect of pulse plasma nitriding of M2 steel, Surf. Coat. Technol. 111 (1999) 148–157.

[12] S. Grigoriev, A. Metel, Plasma- and beam-assisted depsition methods, in: A.A. Voevodin, D. V. Shtansky, E.A. Levashov, J.J. Moore (Eds.), Nanostructured Thin Films and Nanodispersion Strengthened Coatings, Kluwer Academic Publishers, Dordrecht, 2004: pp. 147–154.

[13] J. Yang, M. Odén, M.P. Johansson-Jõesaar, L. Llanes, Grinding effects on surface integrity and mechanical strength of WC-Co cemented carbides, Procedia CIRP. 13 (2014) 257–263.

[14] D. Marton, J. Fine, On the development of increasing surface roughness during ion sputtering, Thin Solid Films. 151 (1987) 433–439.

[15] D. Sanders, A. Anders, Review of cathodic arc deposition technology at the start of the new millennium, Surf. Coat. Technol. 133–134 (2000) 78–90.

[16] S. Rebeggiani, On Polishability of Tool Steels, 2013. http://www.diva-portal.org/smash/record.jsf?searchId=1&pid=diva2:621848 (accessed November 4, 2016).

[17] J.R. Davis, Microstructural Analysis of Cemented Carbides, in: J.R. Davis (Ed.), ASM Spec. Handb. Tool Mater., ASM International, Ohio, 1995: pp. 415–419.

[18] R. Mitsche, ed., Fortschritte in der Metallographie, Riederer Verlag, Stuttgart, 1972.

[19] B.L. Bramfitt, A.O. Benscoter, Metallographer's guide: practices and prcedures for irons and steels, ASM International, Ohio, 2002.

[20] C.M. Cotrell, A. Sprague, James, F.A. jun. Smidt, ASM handbook: Volume 5: Surface Engineering, ASM International, Ohio, 1994.

[21] A.T. Santhanam, Metallography of cemented carbides, in: G.F. Vander Voort (Ed.), ASM Handb. Vol. 9 Metallogr. Microsturctures, ASM International, Ohio, 2004.

[22] G.T. Beilby, Aggregation and flow of solids, McMillan & Co., London, 1921.

[23] D. Depla, Magnetrons, reactive gases and sputtering, 3rd ed., Diederik Depla, Gent, 2015.

[24] P. Sigmund, Sputtering by Ion Bombardment: Theoretical Concepts, in: R. Behrisch (Ed.), Sputtering by Part. Bombard. I, Springer-Verlag, 1981.

Publication III

Thermal crack network on CVD TiCN/α-Al_2O_3 coated cemented carbide cutting tools

M. Gassner, N. Schalk, M. Tkadletz, C. Czettl, C. Mitterer

Manuscript submitted for publication

Thermal crack network on CVD TiCN/α-Al_2O_3 coated cemented carbide cutting tools

Martina Gassner[1,†‡], Nina Schalk[1], Michael Tkadletz[1], Christoph Czettl[2], Christian Mitterer[1]

[1] Department of Physical Metallurgy and Materials Testing, Montanuniversität Leoben, Franz-Josef-Straße 18, 8700 Leoben, Austria

[2] CERATIZIT Austria GmbH, Metallwerk-Plansee-Straße 71, 6600 Reutte, Austria

Abstract

TiCN/α-Al_2O_3 coatings grown by thermally activated chemical vapor deposition (CVD) on cemented carbide cutting inserts typically exhibit a thermal crack network. Although these coated inserts are frequently industrially used for various cutting operations, there is still a lack in understanding of formation and characteristics of these cracks. Thus, the present work focuses on the investigation of the crack network observed on the surface as well as within the layers of CVD TiCN/α-Al_2O_3 coated cemented carbide cutting inserts. The samples were investigated in different conditions, i.e. in the as-deposited state, after post-treatment by wet-blasting, after annealing, after wet-blasting and annealing, and after face turning, by scanning electron microscopy. Cross-sections of cracked areas were prepared by focused ion beam milling to evaluate crack formation and opening. Further, diffusion processes within the cracks were investigated by energy-dispersive X-ray spectroscopy. While wet-blasting results in closure of thermal cracks near the coating surface due to the introduction of compressive stresses, this effect is equalized after annealing and after turning; cracks are filled with TiO_2 caused by oxidation of the TiCN base-layer and reaction with Al_2O_3 and – in the case of turning – by workpiece material.

Keywords: turning, α-Al_2O_3, TiCN, cemented carbide, hard coatings, cracks, CVD

† Corresponding author
e-mail address: martina.gassner@stud.unileoben.ac.at

‡ Present address: voestalpine Tubulars GmbH & Co. KG, Alpinestraße 17, 8652 Kindberg, Austria

1. Introduction

Due to their excellent properties, such as chemical inertness, mechanical and thermal stability, low thermal conductivity and high hardness, Al_2O_3 coatings deposited on cemented carbide cutting inserts are widely used for turning of steel [1–7]. For industrial applications, predominantly thermally activated chemical vapor deposition (CVD) is applied to produce thick and uniform Al_2O_3 coatings [2,8,9]. Al_2O_3 exists in several metastable modifications, such as γ, δ, η, θ, κ, as well as the stable α phase. For commercial use, mainly the metastable κ-Al_2O_3, and the thermodynamically stable α-Al_2O_3 phase are of importance [6,10–12]. In the past years, considerable effort focused on further development of microstructure, phase and texture control as well as adhesion of Al_2O_3 coatings to further improve their mechanical properties [2,6,9]. Commonly, an Al_2O_3 top-layer is combined with a TiCN base-layer providing mechanical support to maximize tool life and to improve cutting behavior [9]. However, the substrate, the base- and the top-layer exhibit significantly different thermal expansion coefficients: cemented carbide substrate with $4.5 – 6.5 \times 10^{-6}$ K^{-1} depending on the content and composition of the mixed carbide and the Co-content, TiCN with $7 – 8 \times 10^{-6}$ K^{-1} depending on the C/N ratio, and α-Al_2O_3 top-layer with 8.3×10^{-6} K^{-1} [13–15]. Consequently, the high deposition temperature of ~1,000 °C necessary for CVD of α-Al_2O_3 results in tensile residual stress and the formation of a crack network in the coating [3]. Technically, the application-related limitations imposed by the tensile stresses are overcome by post-deposition treatments like dry- or wet-blasting [16,17].

The aim of this study is to contribute to the understanding of thermal crack formation and to the characteristics of the crack network in TiCN/α-Al_2O_3 coated cemented carbide cutting inserts. Consequently, the influence of a blasting post-treatment, annealing and turning on the thermal crack network was investigated. The crack network as well as diffusion processes through these cracks were characterized by scanning electron microscopy (SEM) on the coating surface and on focused ion beam (FIB) polished cross-sections. Energy-dispersive X-ray spectroscopy (EDX) was used to investigate the species found within the cracks.

2. Experimental details

The deposition of a TiCN/α-Al_2O_3 coating with a total thickness of 15 µm (10 µm TiCN base-layer, 5 µm α-Al_2O_3 top-layer) was carried out in a Sucotec SCT600TH industrial-scale CVD plant, as described in

ref. [16]. The α-Al_2O_3 has a (0001) preferred orientation, as evidenced in an earlier work by X-ray diffraction [18]. Cutting inserts in CNMG 120408EN-M50 geometry (according to ISO 1832) with a chemical composition of 93.4 wt% tungsten carbide, 0.6 wt% mixed carbides and 6.0 wt% cobalt, were used as substrates. The coated samples were investigated in the as-deposited state, after post-treatment by wet-blasting using an Al_2O_3 suspension following the procedure reported in ref. [19], after annealing, after wet-blasting and annealing, and after turning, respectively. The as-deposited α-Al_2O_3 top-layer exhibits tensile residual stresses in the range of several hundred MPa [16]. Blasting has been reported to introduce compressive stresses in the range of ~2 GPa and to yield a smoothed surface finish [16,19,20]. The annealing treatments of the as-deposited and wet-blasted inserts were carried out in ambient air using a Nabertherm N 11/HR furnace, where the samples were heated with a rate of 10.5 °C/min up to 1,000 °C and held constant for 15 minutes.

Face turning operations were performed using the wet-blasted inserts in a HEYNUMAT 15U/800 slant-bed turning machine in dry condition without cooling. 42CrMo4 (DIN 1.7225), an alloyed quenched and tempered steel (according to EN 10083-3), was used as workpiece material. The turning parameters were set to a feed rate of 0.35 mm/rev, a cutting depth of 2 mm and a cutting speed of 220 m/min. The diameter of the workpiece material was 58 mm at the beginning and the cut was set straight into the center. For observation of wear on the cutting insert, inspections by light optical microscopy were conducted recurrently after 25 cuts. The inserts were tested until reaching the end of tool life, defined by a flank wear of 0.3 mm, which was reached after ~15 minutes. Thus, the time for the annealing treatment mentioned above was also set to 15 minutes to achieve a comparable time of temperature exposure of the inserts.

The rake face of cutting inserts in as-deposited, wet-blasted, annealed, wet-blasted and annealed state as well as after face turning was examined using a Zeiss EVO MA 25 SEM. Prior to the SEM investigations of the inserts used for turning tests, adhered workpiece material was removed by exposing the inserts to an aqueous solution of 30 wt% HCl for 30 minutes at ~30 °C. Investigation of cross-sections showing the crack extension through the coating down to the substrate was done with a Zeiss Auriga Crossbeam field emission gun SEM, after prior preparation by FIB-milling with an Orsay Physics Cobra Z-05 extension. An EDAX Apollo 40+ detector was utilized for EDX analysis within the cross-section of the wet-blasted and annealed insert and the insert after face turning to determine eventual chemical modifications within the cracks.

3. Results

SEM investigations confirm that cracks are present within the α-Al_2O_3 top-layer in all observed conditions, i.e. in the as-deposited state, after post-treatment by wet-blasting, after annealing, after wet-blasting and annealing, and after face turning. Fig. 1 gives an overview of the TiCN/α-Al_2O_3 coated inserts right after deposition (Fig. 1a and c) and after wet-blasting (Fig. 1b and d). While on the macro-scale no cracks are visible (Fig. 1a and b), their formation is clearly evident in the SEM images in Fig. 1c and d taken at higher magnification. After coating deposition, the insert has a faceted surface (Fig. 1c), which is significantly smoothened after wet-blasting (Fig. 1d).

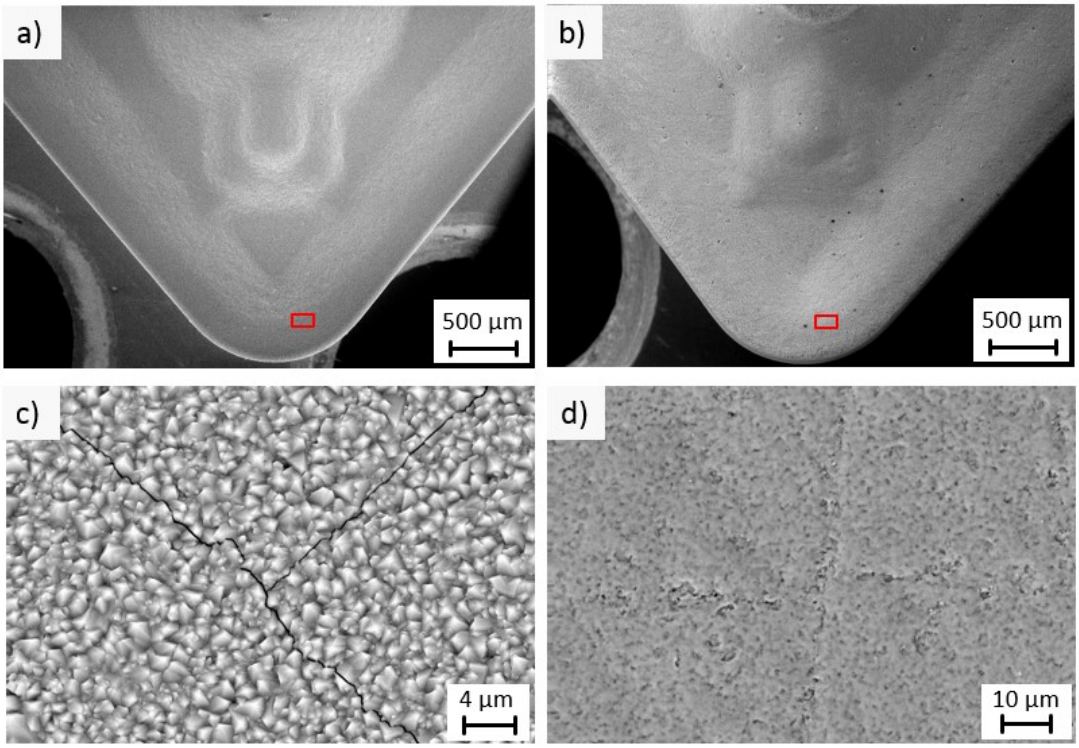

Fig. 1 Secondary electron SEM images of the rake face of the TiCN/α-Al_2O_3 coated cutting inserts showing an overview of the cutting edge in a) as-deposited and b) wet-blasted state. SEM micrographs of the rake face in higher magnification as indicated by the red rectangles in a) and b) in backscattered mode: c) as-deposited and d) wet-blasted state.

The insert displayed in Fig. 2a was annealed directly after deposition, whereas the insert shown in Fig. 2b was annealed after wet-blasting. Both samples were annealed under the same conditions, i.e. in ambient air at 1,000 °C for 15 minutes. Compared to the as-deposited sample shown in Fig. 1c, the cracks appear brighter after annealing (Fig. 2c). The bright appearance of the cracks is caused by an increased negative electrical charge and increased emission of secondary electrons at the edges of

the cracks of the nonconductive Al_2O_3 layer during SEM. This observation leads to the assumption that the atmosphere during annealing and possible contaminations enhance the emission of secondary electrons at exposed sample regions like the rims of cracks. In contrast to the inserts presented in Fig. 1, which were not annealed, the crack network of the as-deposited and annealed (Fig. 2a) and the wet-blasted and annealed (Fig. 2b) inserts can be visualized already at low magnifications in the SEM. Wet-blasting leads to an apparent closure of the cracks on the surface, as visualized in Fig. 1d. After annealing, these cracks appear open again as can be seen by comparing the inserts before wet-blasting, i.e. in the as-deposited state (Fig. 1c), and after wet-blasting and annealing (Fig. 2d), where the crack opening is comparable. For the as-deposited and annealed insert (Fig. 2c), no change in crack opening is observable compared to the as-deposited state (Fig. 1c).

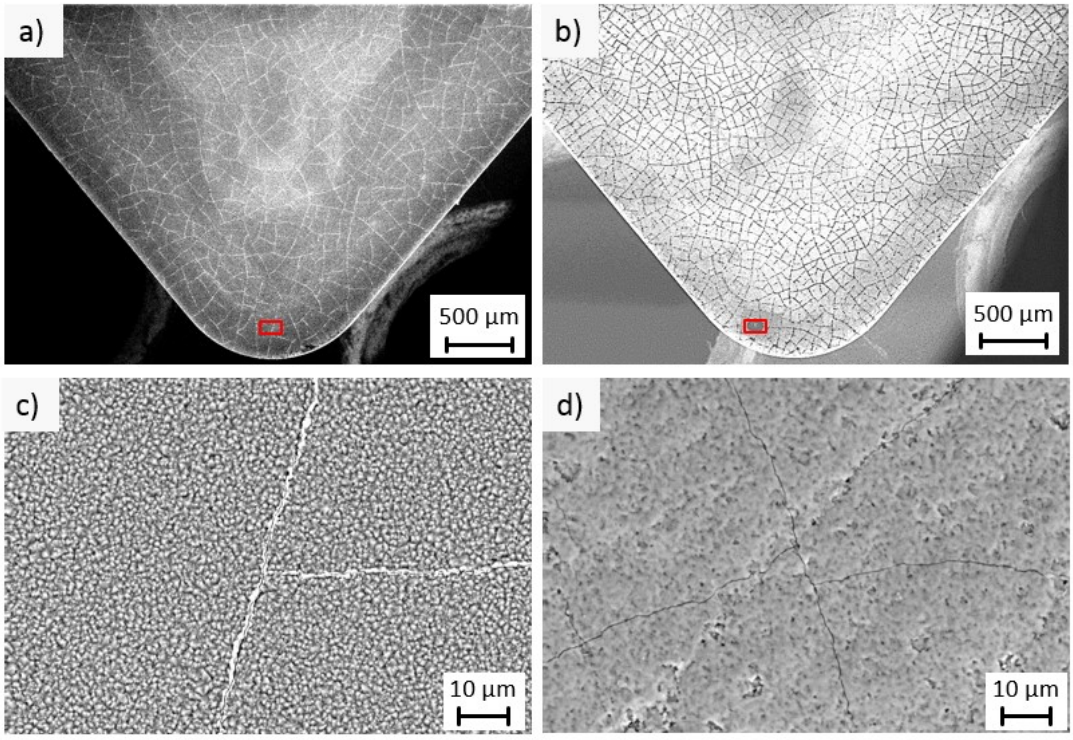

Fig. 2 Secondary electron SEM images of the rake face of the TiCN/α-Al_2O_3 coated cutting inserts after a) annealing and (b) after wet-blasting and annealing at 1,000 °C for 15 min. SEM micrographs of the rake face in higher magnification as indicated by the red rectangles in a) and b) in backscattered mode: c) annealed and d) wet-blasted and annealed.

Investigations of FIB-milled cross-sections of the inserts in the as-deposited, wet-blasted, wet-blasted and annealed state, and after face turning allow to observe the crack extension through the TiCN/α-Al_2O_3 coating. For the as-deposited insert shown in Fig. 3a, thermal cracks with a uniform crack opening within the α-Al_2O_3 layer can be observed. Wet-blasting results in a closure of the crack in the

upper ~3 µm of the Al_2O_3 layer, as evidenced by Fig. 3b (the closed crack is indicated by red arrows). After annealing of the wet-blasted insert, a crack with an opening comparable to the as-deposited state is visible in Fig. 3c. These observations are in good agreement with the appearance of the crack network on the surface of the inserts shown in Fig. 1c and Fig. 2d. For the wet-blasted and annealed sample (Fig. 3c), an additional crack apparently reaching from the α-Al_2O_3 interface to ~3 µm below the coating surface can be observed. This crack seems to be filled with material, while the crack which reaches the surface appears more open, comparable to those cracks observed on the as-deposited insert. EDX measurements yielded an increased Ti content within the filled crack compared to the crack-free Al_2O_3 layer (Fig. 3c, spots 1 and 2 as well as Fig. 3d). This leads to the assumption that during annealing diffusion of Ti stemming from the TiCN base-layer occurs at the crack surfaces.

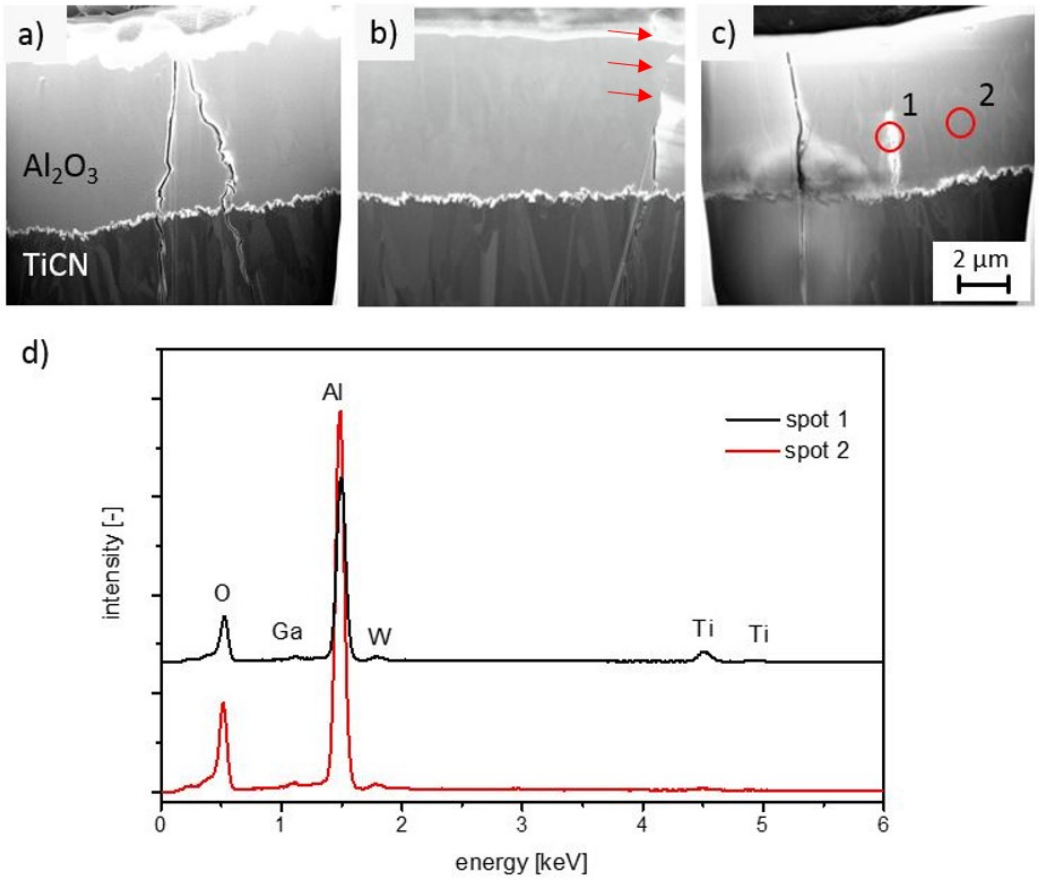

Fig. 3 a-c) Secondary electron SEM images of FIB-milled cross-sections: a) as-deposited, b) wet-blasted (the red arrows indicate the position of the now closed crack) and c) wet-blasted and annealed. d) EDX spectra of the areas indicated by red cycles in c). EDX spectra show also peaks stemming from FIB preparation; Ga from the primary ion beam hitting the surface and W originating from removed and redeposited substrate material.

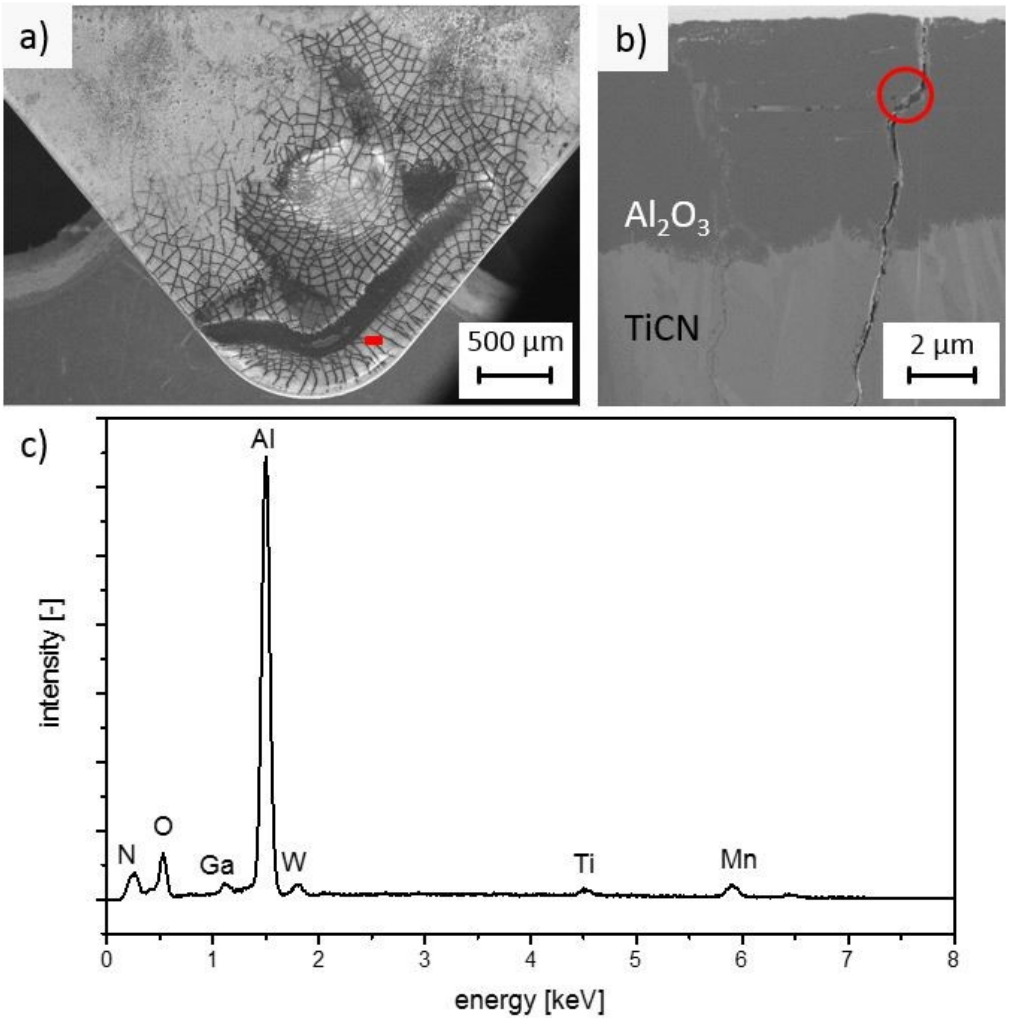

Fig. 4 a) Secondary electron SEM image of the rake face of the cutting insert after face turning. b) SEM cross-section obtained at the section indicated by the red bar in a) in backscattered mode. c) EDX spectrum of the area indicated by the red cycle in b). EDX spectra also show peaks stemming from FIB preparation; Ga from the primary ion beam hitting the surface and W originating from removed and redeposited substrate material.

Fig. 4a depicts the rake face of the investigated cutting insert after face turning until the end of tool life is reached after ~15 minutes. In the region where the insert was in direct contact with the steel chip, the visibility of the crack network – cracks appear dark in the SEM – is very similar to the wet-blasted and annealed insert (Fig. 2b). The cross-section prepared by FIB-milling at the position marked in Fig. 4a is displayed in Fig. 4b and exemplifies the crack extension within the Al_2O_3 layer. In contrast to the as-deposited samples, the crack seen in Fig. 4b appears to be partially filled. The crack opening is similar to that observed for both the as-deposited and the wet-blasted and annealed insert. No

evidence of plastic deformation of the cemented carbide substrate, e.g. by displacement of the two opposite crack rims [18], was found in the FIB cross-section. EDX analysis of the material visible within the crack at the position marked in Fig. 4b indicates that beside the coating material also Ti originating from the TiCN base-layer and Mn stemming from the 42CrMo4 workpiece material is present.

4. Discussion

As evidenced by the presented SEM investigations, post-treatment by wet-blasting and subsequent annealing affects the visual appearance of the crack network and the crack opening of CVD TiCN/α-Al_2O_3 coatings on cemented carbide cutting inserts. Inserts without post-treatment by wet-blasting (Fig. 1c) are characterized by open thermal cracks stemming from cooling down after deposition. Crack formation is caused by the mismatch of thermal expansion coefficients of cemented carbide, TiCN and α-Al_2O_3, resulting in tensile residual stress within the coating layers and in further consequence, when the fracture strength is reached, in cracks. Within the coating fragments between the formed cracks, the stresses are retained as long as the fracture strength is not reached [9,16,21]. Post-treatment by wet-blasting introduces compressive stresses into the α-Al_2O_3 top-layer in the range of ~2 GPa [16,20], which significantly reduces crack opening and, consequently, the cracks appear almost closed on the surface of the cutting insert, as evidenced by Fig. 1d. In addition, wet-blasting results in a removal of coating material, causing surface smoothening by abrasion of surface asperities and cone-shaped Al_2O_3 grains. Depending on the blasting parameters such as pressure, grain size and shape, the introduced residual stresses as well as the surface roughness can be tailored [16,22–24]. A transfer of Al_2O_3 wet-blasting material to the coating surface, as reported for metal-blasting, could not be completely excluded [25].

Depending on the follow-up treatment (i.e., post-treatment by wet-blasting and/or annealing, turning tests), additional thermal and/or mechanical stresses lead to changes of the opening of the thermal cracks. SEM investigations of the FIB-prepared cross-section of the wet-blasted insert (Fig. 3b) evidence that the stresses introduced by wet-blasting affect the Al_2O_3 layer to a depth of ~3.5 µm. This is in good agreement with the findings reported in ref. [16], where the affected zone for the α-Al_2O_3 coating reaches ~4 µm beneath the surface, as determined by cross-sectional synchrotron X-ray nanodiffraction. At sufficiently high temperatures, e.g. during annealing, stresses undergo relaxation due to recovery of defects [16,20,24]. Consequently, it can be argued that the change of the crack

opening of the wet-blasted sample after annealing (Fig. 3c) is caused by relaxation of the stresses introduced by wet-blasting. As reported earlier by Schalk *et al.*, annealing at temperatures below the deposition temperature does not significantly affect the stresses within the coating in the as-deposited state, i.e. without further blasting treatment [24]. Vacuum annealing at 900 °C for 15 min has been reported in our earlier work to result in a complete relaxation of the introduced compressive stress [16]. This is also in good agreement with the present observations on the as-deposited and annealed samples, where no indication of a change in the crack network could be detected (Fig. 2c).

At elevated temperatures also diffusion has to be considered. Annealing of TiCN/α-Al_2O_3 coated inserts in air at a temperature of 950 °C has been reported to yield no effect on the chemical composition of the top-layer [26]. Within this work, after 15 minutes of annealing at 1,000 °C no evidence of diffusion within the coating on the as-deposited annealed sample was detected by SEM, as visualized in Fig. 3a; thus obviously the exposure time was too short for noticeable diffusion. Beside the change in crack opening, also cracks which are filled with Ti as evidenced by EDX (Fig. 3d) - most probably TiO_2 caused by oxygen exposure and reaction with Al_2O_3 [27] - could be observed after annealing (Fig. 3c). Oxidation of the TiCN layer is known to start at temperatures between 500 and 600 °C [28]. Both, these filled cracks and cracks closed after wet-blasting are partially only visible in the cross-section of the cutting insert. Thus, the sole investigation of the coating surface is not sufficient for the determination of the actual density of the crack network within the Al_2O_3 layer.

In turning, the contact of the coating surface to the chip leads besides the exposure to elevated temperature as a result of friction at high cutting speeds [29,30] to wear. Recent publications suggest that Al_2O_3 coatings with (0001) orientation, as used within the present study, are characterized by a beneficial wear resistance compared to those with other textures [9,31]. As reported by M'Saoubi *et al.,* the TiCN/α-Al_2O_3 coating system shows no evidence of plastic deformation after turning within the Al_2O_3 grains, even though the chip flow direction within the sliding/abrasive zone is clearly visible [31]. In contrast, Ruppi reported on grains within an (0001) orientated α-Al_2O_3 coating, which were smoothed out and deformed at the surface along the chip flow direction. He assumed that facets protruding the coating surface compensate the stress by plastic flow [9]. Besides this ability, abrasive wear is dominating on the rake face leading to the formation of a wear crater as evidenced in Fig. 4a, due to the exposure to high temperatures and mechanical stresses introduced by the chip/tool contact during turning. The initial thermal cracks, which origin from coating deposition and are

present in all observed conditions, can foster diffusion from the cemented carbide substrate to the coating surface, but can also represent weak spots for plastic deformation. In contrast to previous studies, with exposure times of 50 minutes and longer during annealing in ambient air at temperatures above 900 °C [24,26], no pronounced diffusion of WC out of the substrate could be observed within the present work. This is evidenced by the W EDX peak in Fig. 3d, which is similar within the crack and for the bulk coating, pointing towards its origin from sample preparation. Exposure to mechanical stresses and high temperatures during turning can lead to broadening of existing cracks, where workpiece material is pressed into these cracks. In particular, Mn, which is present in the workpiece material in the form of MnS, was found, as evidenced by Fig. 4b and c. Even though nonmetallic inclusions and low melting components originating from the workpiece material like MnS have no impact on abrasive wear at the prevalent cutting temperatures [32–34], Mn can be found on the rake face of the insert [34].

In summary, the wet-blasted and annealed insert and the wet-blasted insert after turning show similar crack networks on the rake face. However, while the thermal cracks present in wet-blasted and annealed inserts are filled with TiO_2 caused by oxygen exposure and reaction with Al_2O_3, additional workpiece material, in particular MnS, is found within the cracks present in wet-blasted inserts after the turning test. In addition to our earlier work on relaxation of compressive stresses during annealing [16,24], the presented investigations indicate that a similar relaxation occurs at the applied turning conditions, as evidenced by the comparable crack opening of the wet-blasted and annealed inserts and the wet-blasted inserts after turning. Thus, it has to be concluded that in continuous turning under dry conditions studied within this work the main benefit of wet-blasting is the smoothening of the coating surface. It can be assumed that in intermitted cutting processes, as demonstrated by Teppernegg *et al.* [35], for dry milling, the introduced compressive stress plays a much more decisive role in determining the lifetime of the coated cutting insert than in turning.

5. Conclusions

Investigations of the crack network on CVD TiCN/Al_2O_3 coated cemented carbide cutting inserts were done in the as-deposited state, after post-treatment by wet-blasting, after annealing, after wet-blasting and annealing, and after face turning. In all conditions, thermal cracks stemming from cooling down after coating deposition are formed. Wet-blasting results in smooth coating surfaces, where thermal cracks are closed by the introduced compressive stresses and apparently do not reach the coating surface. This crack closure is not permanent, since at elevated temperatures stresses relax and the cracks open again. Further, cracks filled with TiO_2 are observed after annealing or turning. Both, the crack closure after wet-blasting and the filling of cracks after annealing or turning prevent determination of the actual crack density via surface inspection. The crack network on annealed inserts and on inserts after turning appears similarly. For the latter, the thermal cracks are in addition to TiO_2 filled with low melting components from the steel workpiece material.

In summary, the observed findings contribute to a better understanding on the appearance of thermal cracks on CVD TiCN/Al_2O_3 coated cemented carbide cutting inserts and their behavior during application.

6. Acknowledgements

The authors thank Bernhard Sartory (Materials Center Leoben) for SEM, EDX and FIB investigations. Financial support of the Österreichische Forschungsförderungsgesellschaft mbH FFG (grant number 851894) is gratefully acknowledged.

7. References

[1] C. Mitterer, PVD and CVD Hard Coatings, in: V.K. Sarin (Ed.), Compr. Hard Mater., Elsevier, Oxford, 2014: pp. 449–467.

[2] S. Ruppi, Deposition, microstructure and properties of texture-controlled CVD α-Al_2O_3 coatings, Int. J. Refract. Met. Hard Mater. 23 (2005) 306–316.

[3] D. Hochauer, C. Mitterer, M. Penoy, C. Michotte, H.P. Martinz, M. Kathrein, Titanium doped CVD alumina coatings, Surf. Coat. Technol. 203 (2008) 350–356.

[4] A. Osada, E. Nakamura, H. Homma, T. Hayahi, T. Oshika, Wear mechanism of thermally transformed CVD Al_2O_3 layer, Int. J. Refract. Met. Hard Mater. 24 (2006) 387–391.

[5] U. Schleinkofer, C. Czettl, C. Michotte, Coating Applications for Cutting Tools, in: V.K. Sarin (Ed.), Compr. Hard Mater., Elsevier, Oxford, 2014: pp. 453–469.

[6] S. Ruppi, Advances in chemically vapour deposited wear resistant coatings, J. Phys. IV. 11 (2001) 847–859.

[7] J. Garcia, R. Pitonak, The role of cemented carbide functionally graded outer-layers on the wear performance of coated cutting tools, Int. J. Refract. Met. Hard Mater. 36 (2013) 52–59.

[8] A. Larsson, M. Halvarsson, S. Ruppi, Microstructural changes in CVD κ-Al_2O_3 coated cutting tools during turning operations, Surf. Coat. Technol. 111 (1999) 191–198.

[9] S. Ruppi, Enhanced performance of α-Al_2O_3 coatings by control of crystal orientation, Surf. Coat. Technol. 202 (2008) 4257–4269.

[10] S. Vuorinen, L. Karlsson, Phase transformation in chemically vapour-deposited κ-alumina, Thin Solid Films. 214 (1992) 132–143.

[11] S. Ruppi, A. Larsson, A. Flink, Nanoindentation hardness, texture and microstructure of α-Al_2O_3 and κ-Al_2O_3 coatings, Thin Solid Films. 516 (2008) 5959–5966.

[12] S. Ruppi, A. Larsson, Chemical vapour deposition of α-Al_2O_3, Thin Solid Films. 388 (2001) 50–61.

[13] H.O. Pierson, Handbook of chemical vapor deposition (CVD), second edi, Noyes Publications, Park Ridge, 1999.

[14] J.R. Davis, ed., ASM Specialty Handbook - Nickel, Cobalt, and Their Alloys, Ohio, 2000.

[15] F.-W. Bach, Modern Surface Technology, Wiley-VCH, Weinheim, 2006.

[16] M. Tkadletz, J. Keckes, N. Schalk, I. Krajinovic, M. Burghammer, C. Czettl, et al., Residual stress gradients in α-Al_2O_3 hard coatings determined by pencil-beam X-ray nanodiffraction: The influence of blasting media, Surf. Coat. Technol. 262 (2015) 134–140.

[17] N. Schalk, Synthesis and Post-treatment of Hard Coatings for Cemented Carbide Cutting Tools, Montanuniversität Leoben, 2013.

[18] M. Gassner, N. Schalk, M. Tkadletz, M. Pohler, C. Czettl, C. Mitterer, Influence of cutting speed and workpiece material on the wear mechanisms of CVD TiCN/α-Al_2O_3 coated cutting inserts during turning, Wear. (2018).

[19] S. Ruppi, Texture-hardened α-alumina coated tool, EP 1 953 258 A1, 2008.

[20] J. Garcia, M.F. Moreno, J. Östby, J. Persson, H.C. Pinto, Design of coated cemented carbides with improved comb crack resistance, 19th Plansee Semin. 2017. (2017) 1–8.

[21] C. Czettl, C. Mitterer, M. Penoy, C. Michotte, M. Kathrein, Stress state of CVD TiCN/κ-Al_2O_3 hard coatings, in: Surf. Modif. Technol. 24, Dresden, 2010.

[22] K.-D. Bouzakis, G. Skordaris, G. Gerardis, G. Katirzoglou, S. Makrimallakis, F. Klocke, et al., The Effect of Micro-Blasting on the Cutting Performance of Coated Tools, FME Trans. 37 (2009) 71–82.

[23] K.D. Bouzakis, E. Bouzakis, G. Skordaris, S. Makrimallakis, A. Tsouknidas, G. Katirtzoglou, et al., Effect of PVD films wet micro-blasting by various Al_2O_3 grain sizes on the wear behaviour of coated tools, Surf. Coat. Technol. 205 (2011) 128–132.

[24] N. Schalk, C. Mitterer, C. Czettl, B. Sartory, M. Penoy, C. Michotte, Dry-blasting of α- and κ-Al_2O_3 CVD hard coatings: Friction behaviour and thermal stress relaxation, Tribol. Lett. 52 (2013) 147–154.

[25] A. Riedl, N. Schalk, C. Czettl, B. Sartory, C. Mitterer, Tribological properties of Al_2O_3 hard coatings modified by mechanical blasting and polishing post-treatment, Wear. 289 (2012) 9–16.

[26] X. Chen, H. Liu, Q. Guo, S. Sun, Oxidation behavior of WC-Co hard metal with designed multilayer coatings by CVD, Int. J. Refract. Met. Hard Mater. 31 (2012) 171–178.

[27] D. Hochauer, C. Mitterer, M. Penoy, S. Puchner, C. Michotte, H.P. Martinz, et al., Carbon doped α-Al_2O_3 coatings grown by chemical vapor deposition, Surf. Coat. Technol. 206 (2012) 4771–4777.

[28] J. Wagner, C. Mitterer, M. Penoy, C. Michotte, W. Wallgram, M. Kathrein, Structure and

properties of TiN coatings, in: 16th Int. Plansee Semin., 2005: pp. 917–931.

[29] W. Grzesik, Experimental investigation of the cutting temperature when turning with coated indexable inserts, Int. J. Mach. Tools Manuf. 39 (1999) 355–369.

[30] W. Grzesik, M. Bartoszuk, P. Nieslony, Finite element modelling of temperature distribution in the cutting zone in turning processes with differently coated tools, J. Mater. Process. Technol. 164-165 (2005) 1204–1211.

[31] R. M'Saoubi, O. Alm, J.M. Andersson, H. Engström, T. Larsson, M.P. Johansson-Jõesaar, et al., Microstructure and wear mechanisms of texture-controlled CVD α-Al_2O_3 coatings, Wear. 376-377 (2017) 1766–1778.

[32] N. Ånmark, A. Karasev, P.G. Jönsson, The Influence of Microstructure and Non-Metallic Inclusions on the Machinability of Clean Steels, Steel Res. Int. 88 (2016) 1–8.

[33] A. Nordgren, A. Melander, Deformation behaviour of different types of inclusion during chip formation turning of quenced and tempered steels, Mater. Sci. Technol. 5 (1989) 940–951.

[34] A. Larsson, S. Ruppi, Structure and composition of built-up layers on coated tools during turning of Ca-treated steel, Mater. Sci. Eng. A. 313 (2001) 160–169.

[35] T. Teppernegg, T. Klünsner, P. Angerer, C. Tritremmel, C. Czettl, J. Keckes, et al., Evolution of residual stress and damage in coated hard metal milling inserts over the complete tool life, Int. J. Refract. Met. Hard Mater. 47 (2014) 80–85.

Publication IV

Influence of cutting speed and workpiece material on the wear mechanisms of CVD TiCN/α-Al_2O_3 coated cutting inserts during turning

M. Gassner, N. Schalk, M. Tkadletz, M. Pohler, C. Czettl, C. Mitterer

Wear 398–399 (2018) 90–98

Influence of cutting speed and workpiece material on the wear mechanisms of CVD TiCN/α-Al_2O_3 coated cutting inserts during turning

Martina Gassner[1], Nina Schalk[1], Michael Tkadletz[1], Markus Pohler[2], Christoph Czettl[2], Christian Mitterer[1]

[1] Department of Physical Metallurgy and Materials Testing, Montanuniversität Leoben, Franz-Josef-Straße 18, 8700 Leoben, Austria

[2] CERATIZIT Austria GmbH, Metallwerk-Plansee-Straße 71, 6600 Reutte, Austria

Abstract

Although several studies are available discussing wear of coated cutting inserts during turning, there is still a lack in understanding of the dominating wear mechanisms. Thus, the present work focuses on investigation of wear mechanisms after longitudinal turning with CVD TiCN/α-Al_2O_3 coated cemented carbide cutting inserts. Three different steels, 42CrMo4, Ck60 and 100Cr6, were used as workpiece materials. In addition, the cutting speed was varied between 150 and 250 m/min. The used cutting inserts were investigated by optical microscopy after different stages of lifetime. Cross-sections within the crater region were prepared to evaluate the crater wear as well as the contribution of plastic deformation of the cemented carbide to the blunting of the cutting edge. Scanning electron microscopy was applied for a detailed investigation of the worn regions. Significant differences in tool life could be observed for the different workpiece materials and cutting speeds, ranging from 3 min for turning of 42CrMo4 to 26 min for 100Cr6 at the highest cutting speed and from 46 min for 42CrMo4 to 94 min for Ck60 at the lowest cutting speed. The differing tool life could be correlated with the microstructure and mechanical properties of the respective workpiece materials.

Keywords: turning, wear, cemented carbide, hard coatings, cutting inserts, workpiece material

1. Introduction

The demands for hard coated cemented carbide cutting tools are wide spread with respect to their huge range of applications. One main requirement that has to be fulfilled is a high, reliable and stable performance during cutting and a maximized tool lifetime [1]. Hard coatings are widely applied to provide wear and thermal protection of cemented carbide tools, both contributing to enhanced cutting performance and an extended tool life [2,3]. For turning applications, the industrially dominating coating system is TiCN/Al_2O_3 grown via chemical vapor deposition (CVD). There, an α-Al_2O_3 top-layer providing chemical inertness, thermal stability and hardness is combined with a TiCN base layer, which matches the properties of the cemented carbide substrate and provides mechanical support for the top-layer [4,5]. Coatings with a total thickness of up to 20 µm can be grown, offering a huge wear reservoir for continuous cutting applications. A tailored post treatment of the tool after deposition by blasting processes to decrease surface roughness and for the introduction of compressive residual stresses is state of the art [6–8]. Cemented carbide inserts with a cobalt content of 5 – 12 wt% and a cobalt-enriched surface zone are commonly used for turning applications [2,9]. Tool life of coated cemented carbide cutting tools is determined by the following two criteria: *(i)* flank wear and *(ii)* crater wear defined as the wear on the rake face of the insert. Flank wear is caused by direct workpiece contact, whereas crater wear is induced by the chip sliding over the rake face. Both wear phenomena are caused by abrasive and adhesive wear [10]. The addressed wear mechanisms strongly depend on, among others, tool material, tool shape, coating, machined workpiece material, and cutting parameters like cutting speed, feed rate and applied coolants. Within the majority of the available literature, only the influence of one chosen workpiece material [11–14] and/or the influence of different applied coatings, coating microstructures [15,16] or substrate compositions [1,9] has been investigated. There is a lack of studies on the effect of different workpiece materials on tool performance and wear. Thus, the aim of this study was to investigate the influence of different cutting speeds and workpiece materials on tool life during turning with TiCN/Al_2O_3 coated cemented carbide cutting inserts. Special emphasis was laid onto the evolution of flank and crater wear, including cobalt diffusion and plastic deformation of the cemented carbide, at different stages of lifetime.

2. Experimental details

Longitudinal turning tests were performed using cemented carbide cutting inserts in CNMG 120408EN-M50 geometry (according to ISO 1832, see Fig. 1a). The chemical composition of the inserts was 84.9 wt% tungsten carbide, 8.1 wt% mixed carbides and 7.0 wt% cobalt, with a ~20 µm thick cobalt-enriched surface zone. The cemented carbide inserts were coated by CVD without any further surface pre-treatment. A TiCN/α-Al_2O_3 coating with a total thickness of 15 µm (10 µm TiCN base-layer, 5 µm α-Al_2O_3 top-layer) was deposited in a Sucotec SCT600TH industrial-scale CVD plant, as described earlier by Tkadletz et al. [6]. Since the α-Al_2O_3 layer is in the as-deposited state under tensile residual stress [6]; post-treatment was done by wet-blasting to introduce compressive stresses and to smoothen the surface, following the procedure reported in [17]. The investigation of the crystallographic structure was carried out using a Bruker-AXS D8 Advance diffractometer. Coating microstructure was investigated using a Zeiss Auriga Crossbeam field emission gun scanning electron microscope (FEG-SEM) after focused ion beam (FIB) milling of cross-sections with an Orsay Physics Cobra Z-05 extension. Turning tests were performed using a HEYNUMAT 15U/800 slant-bed turning machine and a tool of type DCLNL2525-M12 with a work angle of 95° and a tilt of 6° in radial and axial direction. All longitudinal turning tests were carried out in dry conditions without cooling. Parameters were set to a feed rate of 0.35 mm/rev; cutting depth of 2 mm; cutting speeds (v_c) of 150, 200 and 250 m/min, respectively.

Turning tests were conducted using three different workpiece materials: *(i)* 42CrMo4 (DIN 1.7225, provided by Istil (Ukraine)), an alloyed quenched and tempered steel with a tensile strength of 860 N/mm² (according to EN 10083-3), *(ii)* Ck60 (DIN 1.1221, provided by Metallurgical Works Petrostal (Russia)), an unalloyed quenched and tempered steel with a tensile strength of 820 N/mm² (according to EN 10083-2:2006), and *(iii)* 100Cr6 (DIN 1.3505, provided by Stauber Metalltechnologie (Germany)), an unalloyed quenched and tempered steel, soft annealed with a tensile strength of 660 N/mm² (according to EN ISO 683-17). The compositions according to manufacturers' test certificates are displayed in Table 1.

Table I: Chemical composition (wt%) of the used workpiece materials, according to manufacturers' test certificates.

Work-piece material	C	Si	Mn	S	P	Cr	Ni	Cu	Al	Mo	others
42CrMo4	0.430	0.210	0.690	0.030	0.012	0.960	0.100	0.180	0.027	0.170	0.007
Ck60	0.590	0.290	0.670	0.028	0.018	0.140	0.200	0.190	0.040	0.020	0.017
100Cr6	1.000	0.250	0.350	0.024	0.009	1.420	-	0.150	0.020	0.040	0.025

The diameter of the workpiece material was 138 mm at the beginning and 58 mm at the end of testing. To ensure a constant workpiece quality and surface condition, a dummy tool was used prior to the turning test. For observation of the wear on the cutting insert by light optical microscopy, inspections were conducted in one minute intervals at the beginning, while after four minutes the intervals of the subsequent inspection were set to three minutes. For the evaluation of the lifetime, the flank wear (0.3 mm) on the clearance flank face ($VB_{H(max)}$) and on the nose ($VB_{R(max)}$) as well as the wear on the rake face (i.e. the crater wear) of the insert have been evaluated (see Fig. 1b). For every combination of workpiece material and cutting speed, three inserts have been used, enabling to investigate the wear progress after 1 minute, at the end of tool life and at an intermediate stage. For further investigations, cutting inserts were cleaned from adhered workpiece material by exposing them to an aqueous solution of 30 wt% HCl for 30 minutes at ~30 °C.

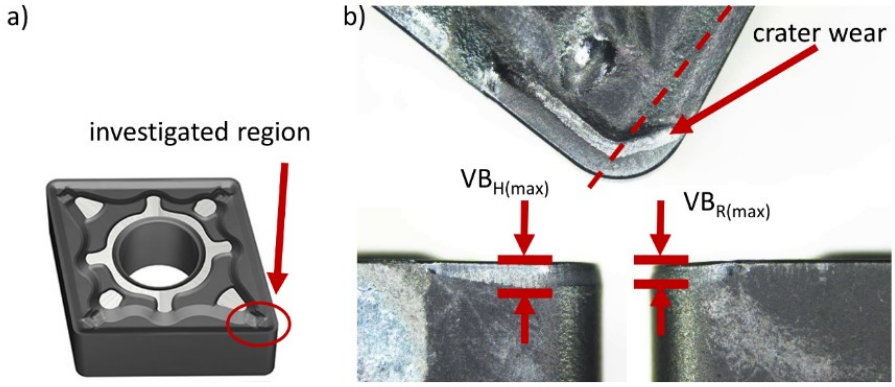

Fig. 1 a) The position investigated on the cutting insert in CNMG 120408-M50 geometry (indicated by the red ellipsis). Insert shape: rhombus 80°; clearance angle 0°; 12.9 mm cutting edge length; 4.76 mm insert thickness; 0.8 mm nose radius; cutting edge: sharp; cutting direction: two-sided. b) The investigated positions for studying crater and flank wear, indicated by red arrows. The red dotted line indicates the position of the cross-section prepared for further light optical/SEM investigations.

Cross-sections, rake and flank face were investigated using a Keyence VHX-5000 digital microscope equipped with VH-Z250R/W/T and VH-Z20R/W/T objectives. For the investigation of the crater wear, flank wear and plastic deformation by means of light optical and scanning electron microscopy (SEM), the cutting inserts were embedded into resin and subsequently grinded and mirror polished. The cross-sections of the cutting inserts were prepared perpendicular to the flank face of the cutting insert, as indicated in Fig. 1b. SEM investigations on the cross-sections were performed using a Zeiss EVO 50 microscope. The investigations of the microstructure of the respective workpiece material were carried out with a Reichert-Jung Polyvar Met optical microscope on embedded, mirror-like polished cross-sections etched with Nital (3 vol% HNO_3 in ethylene). Hardness measurements according to Vickers HV5 were carried out with an Emcotest M4C 025 G3M hardness testing device using a load of 49.03 N.

3. Results

Fig. 2 shows the SEM micrograph of a FIB milled cross-section of a TiCN/α-Al_2O_3 coated cutting insert after wet-blasting. At the interface between the cemented carbide substrate and the coating, the fine grained nucleation zone of the TiCN base-layer is visible, which evolves during the subsequent growth into a columnar structure with a column diameter of ~1 µm. XRD evidences the (0001) orientation of the α-Al_2O_3 top-layer, which displays in the SEM micrograph with a nucleation zone at the interface to the TiCN base-layer, followed by a coarse-grained structure with a grain size of ~2 - 3 µm.

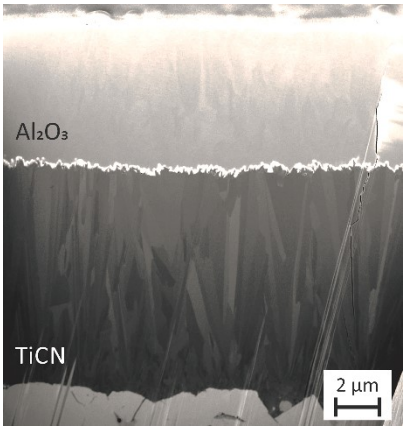

Fig. 2: SEM micrograph taken in backscattered electron mode of a FIB milled cross-section of a TiCN/α-Al_2O_3 coated cutting insert after wet-blasting.

The optical micrographs of the cross-sections of the turned workpiece materials shown in Fig. 3 give an overview of their different microstructures. The 42CrMo4 workpiece material has a martensitic microstructure typical for quenched and tempered steels (Fig. 3a). The Ck60 in Fig. 3b is characterized by a ferritic-pearlitic microstructure, whereas the third investigated workpiece material, i.e. the 100Cr6, has a soft annealed ferritic microstructure with finely dispersed cementite spheroidites (Fig. 3c). The measured Vickers hardness was 221, 220 and 187 HV5 for the 42CrMo4, Ck60 and 100Cr6 steels, respectively, corresponding well to tensile strength defined within the respective EN standards (see section 2).

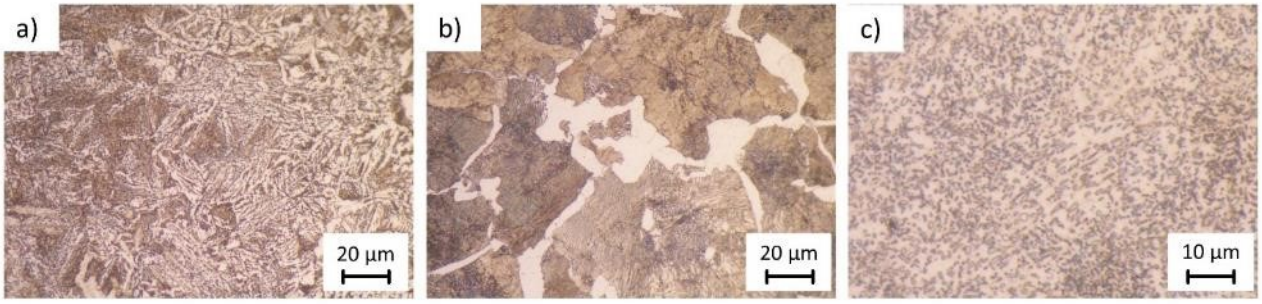

Fig. 3: Light optical micrographs of the three workpiece materials a) 42CrMo4, b) Ck60 and c) 100Cr6.

When comparing the effect of the different applied cutting speeds on tool performance, Fig. 4 shows clearly - considering the different x-axis scales of the three diagrams - that the tool lifetime increases with decreasing cutting speed for all of the used workpiece materials. For all applied cutting speeds, the workpiece material 42CrMo4 resulted in the shortest tool lifetime. For both 100Cr6 and Ck60, very similar lifetimes were observed, except for turning at a speed of 250 m/min. Fig. 4 indicates that the tool life end criteria differ for the given cutting speed and the three workpiece materials. At v_c = 150 m/min, the end of tool life criterion was the extensive crater wear for Ck60, which is in contrast to the other two workpiece materials where the flank wear (reaching the 0.3 mm flank wear criterion) was dominating. After a short ascending slope in the first five minutes of turning, for all three workpiece materials the curves reached a constant slope of the flank wear (see Fig. 4a). At v_c = 200 m/min, for all inserts the end of tool life criterion of 0.3 mm flank wear was fulfilled. For the workpiece materials 100Cr6 and Ck60, after a quick rise of the flank wear within the first 15 minutes, a constant linear wear could be observed until approximately ten minutes before reaching the end of tool life (see Fig. 4b). For turning of 42CrMo4 at the highest cutting speed studied within our investigations of 250 m/min, a nearly linear rise of flank wear without reaching a constant level occurred. This is in

contrast to the other two workpiece materials, where at least for one wear criterion on the flank (i.e. clearance face or nose) a constant behavior could be observed (see Fig. 4c). These observations corroborate the assumption that one reason for the different behavior could be the higher tensile strength and hardness of the workpiece material. Turning of 42CrMo4, i.e. the workpiece material with the highest tensile strength and consequently also hardness, results in about half of the tool life at a speed of 150 m/min, about a fifth for 200 m/min and only about a fifth to a tenth for the highest cutting speed of 250 m/min, compared to cutting of 100Cr6 and Ck60. It can also be stated that the end of tool life criterion differs for the chosen cutting speeds. While at a cutting speed of 150 m/min the end of tool life criterion for 42CrMo4 and 100Cr6 is $VB_{H(max)}$, it is crater wear for turning of Ck60 (see Fig. 4a). At a cutting speed of 200 and 250 m/min for 42CrMo4 and 100Cr6, the criterion is the same as for 150 m/min; however, for cutting of Ck60 it has changed to $VB_{R(max)}$ for 200 m/min and to flank wear on both positions ($VB_{H(max)}$ and $VB_{R(max)}$) of the insert at 250 m/min (see Fig. 4b and c).

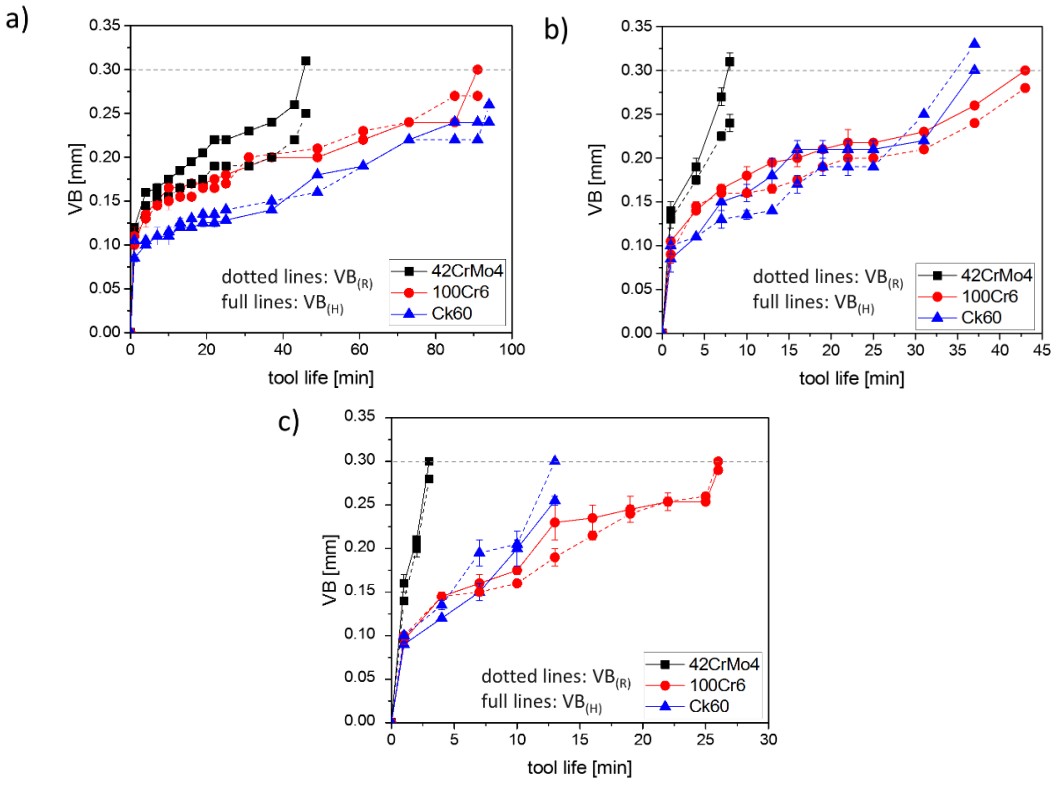

Fig. 4: Flank wear vs. tool life diagrams for the three different cutting speeds v_c and workpiece materials: a) v_c = 150 m/min, b) v_c = 200 m/min, c) v_c = 250 m/min. The dashed horizontal line indicates a flank wear of 0.3 mm. Please note the different x-axis scales.

Fig. 5 provides an overview of the removed workpiece volume depending on the applied cutting speed. At the lowest cutting speed, the highest amount of material was removed. Compared to the results obtained for cutting at 250 m/min, the value at least doubles. The amount of removed material is significantly lower for turning of 42CrMo4 than for the other two workpiece materials, where the volume was very similar at 150 and 200 m/min. Only at the highest cutting speed, the removed workpiece volume differs significantly between all three workpiece materials (see Fig. 5).

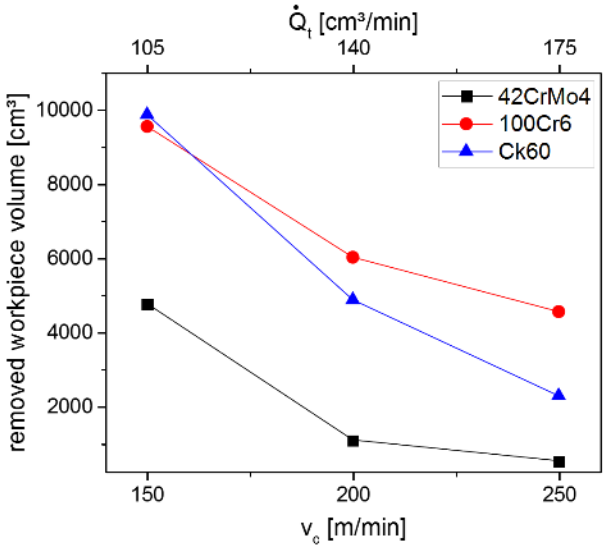

Fig. 5: Volume of removed workpiece material vs. cutting speed.

Although crater wear was only for one insert the dominant end of tool life criterion, in the following a closer look on the respective appearance of the inserts is presented in order to provide insights into the wear mechanisms. Fig. 6 gives an overview of all tested inserts at the end of their respective lifetime. It is evident that the wear crater width increases with increasing lifetime. For the inserts with longer tool life and tested at lower cutting speeds, the width of the wear crater evolves with time. During turning of 42CrMo4 at a cutting speed of 250 m/min, essentially only the Al_2O_3 top-layer is damaged in the contact zone of the worn insert. There, due to abrasive wear caused by the sliding chip, a wear crater mainly in the Al_2O_3 top-layer is formed, whereas the TiCN layer is still partially intact. For 100Cr6 and Ck60, also an increase of the crater width for cutting speeds decreasing from 250 to 200 m/min was observed, while the inserts tested at 200 and 150 m/min are characterized by similar crater widths.

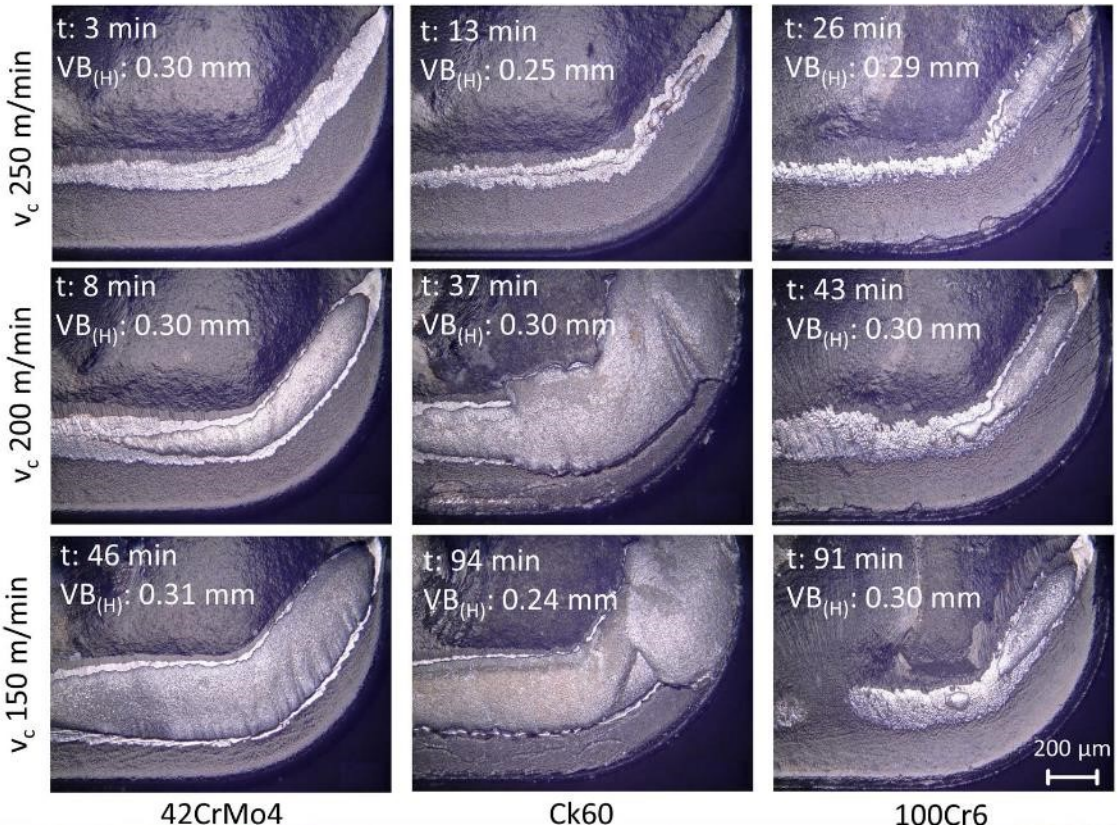

Fig. 6: Light optical micrographs of the rake face of the tested cutting inserts at the end of their respective lifetime t for the different workpiece materials and cutting speeds investigated, after removal of the adhered material.

Fig. 7 gives an overview of the worn cutting inserts after 22 minutes of turning at a speed of 150 m/min. For this condition, none of the tested inserts had reached its end of tool life yet, although the zone of fast wear progress during run-in has already been passed (see Fig. 4). At this point of tool life, the evolution of wear differs between the inserts as expected, since for the 42CrMo4 already Fig. 4 evidences a remarkably shorter tool life than for the other two materials. Additionally, when cutting the 100Cr6 workpiece in the first 10 minutes of turning, wear progresses faster than when cutting the Ck60. After 22 minutes of turning, the length of the wear mark on the flank is wider for 100Cr6 than for Ck60 and even the Al_2O_3 layer is still covering the TiCN layer underneath.

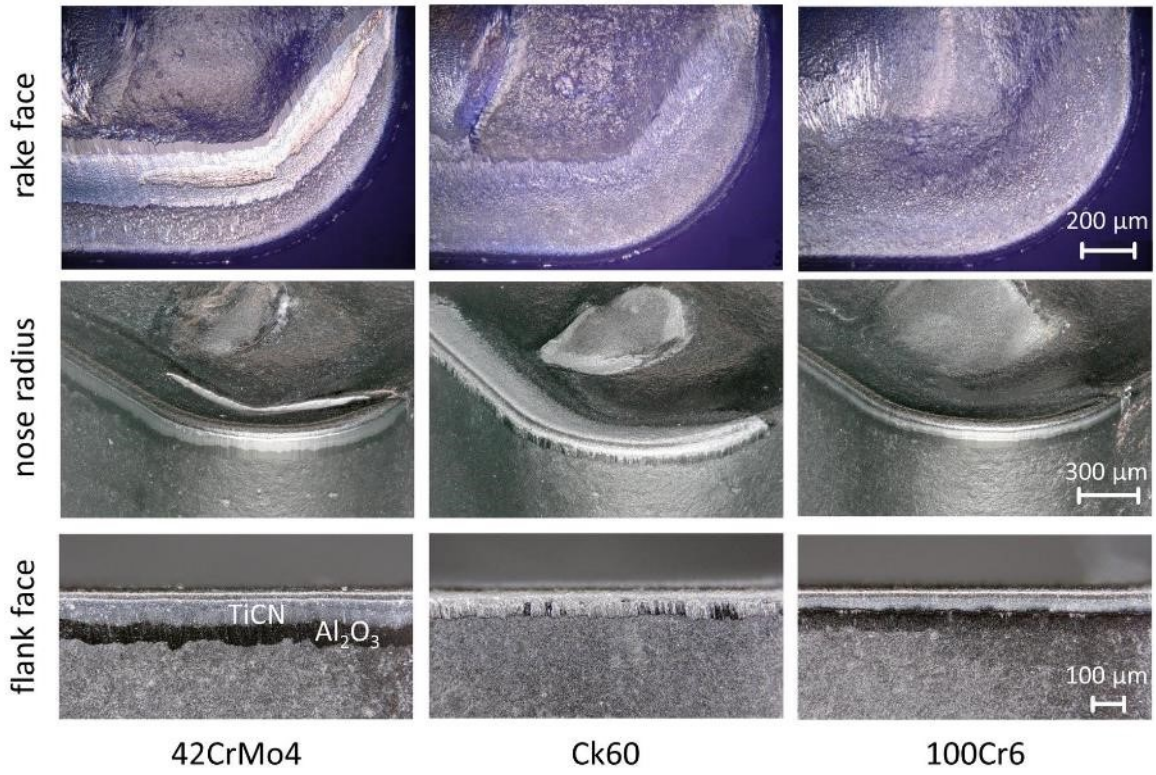

Fig. 7: Light optical micrographs of the worn cutting inserts after 22 min of turning at a speed of 150 m/min for the different workpiece materials.

A comparison of cross-sections of the worn tool at the end of tool lifetime is presented in Fig. 8. Here, it can be observed that on the flank face, where the tool was in contact with the workpiece material, the TiCN layer is still partially intact after turning of 42CrMo4 and Ck60 at all applied cutting speeds. For the insert cutting the 100Cr6, not only both the Al_2O_3 and TiCN layer are removed due to abrasive wear, but also the cemented carbide is locally worn. This effect becomes more pronounced with raising cutting speed. In contrast, for the 100Cr6 the crater wear was not as pronounced as for the other two workpiece materials. Furthermore, with increased cutting speed the crater width decreases for all workpiece materials. Also plastic deformation of the nose of the insert is observable.

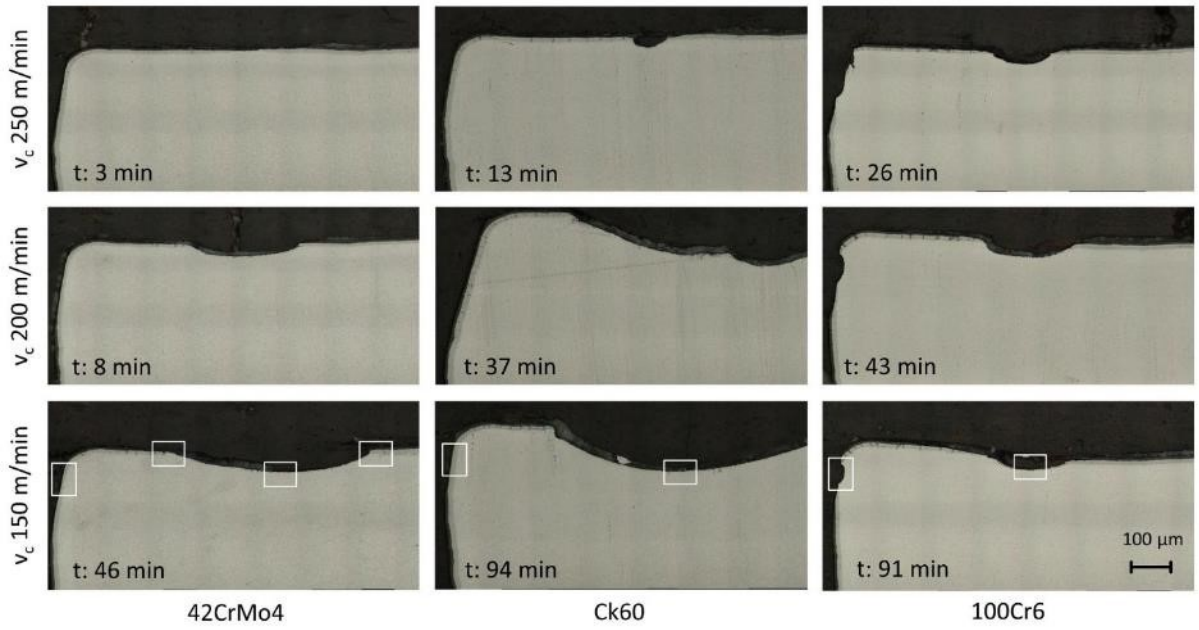

Fig. 8: Light optical micrographs of the cross-sections of the worn cutting inserts at the end of their respective lifetime t for the different workpiece materials and cutting speeds investigated. Positions investigated by SEM are indicated by white frames.

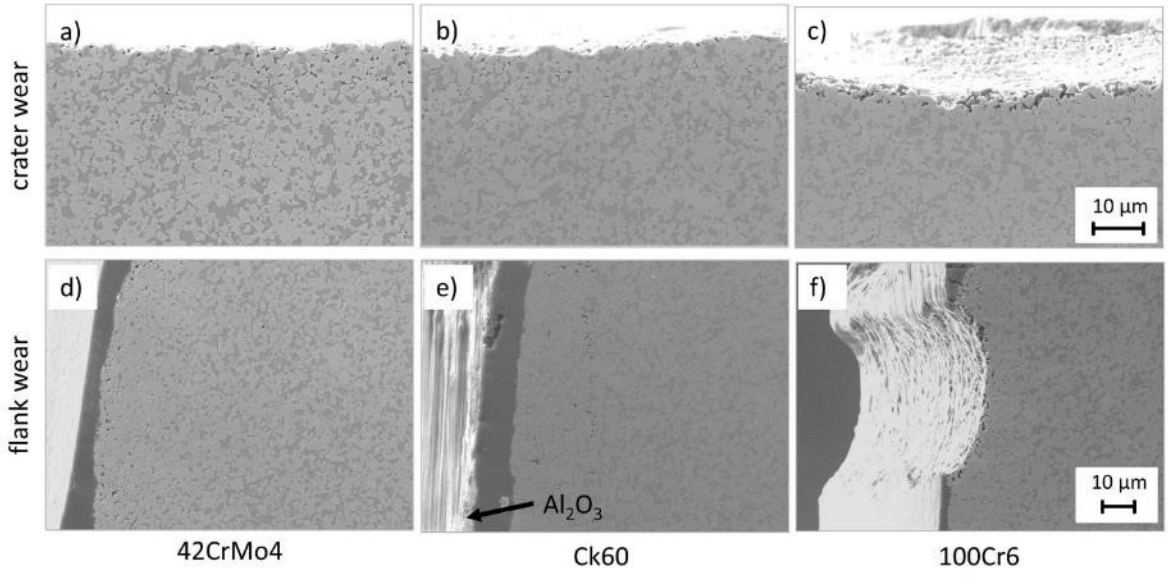

Fig. 9: Secondary electron SEM micrographs of the cross-sections of the worn cutting inserts after turning with a cutting speed of 150 m/min at the end of their tool lifetime for the different workpiece materials. The micrographs illustrating the crater wear were taken in the center of the wear crater for a) 42CrMo4, b) Ck60, and c) 100Cr6. Flank wear for d) 42CrMo4, e) Ck60 and f) 100Cr6.

It is obvious that inserts with similar lifetime are characterized by a different wear pattern. The SEM images of the worn inserts presented in Fig. 9 provide more detailed information on flank and crater wear. After cutting the 42CrMo4, only the TiCN layer is present on the position investigated on the flank face of the insert. This remaining TiCN layer appears smooth, while the cemented carbide underneath shows some pores in the surface-near region, which indicates cobalt binder diffusion towards the insert surface caused by the high temperatures reached during turning (see the dark areas in Fig. 9d). The same effect was observed on the crater wear position in the outer 10 µm, as the investigated cemented carbide insert displays pores (see the dark areas in Fig. 9a). For the insert tested after turning of Ck60, the wear scar appearance is different. There, the TiCN layer seems to be almost intact and also a fraction of the Al_2O_3 top-layer is still present. The remaining coating shows a quite rough surface and at the interface between cemented carbide and coating hardly any voids can be found. However, pores deeper in the cemented carbide at the intersection between cobalt-enriched zone and bulk are observable (see the dark areas in Fig. 9e). Below the wear crater the appearance is similar. There, only some voids could be observed in the bulk material (see Fig. 9b). In contrast to the 42CrMo4 and Ck60, for turning of the 100Cr6 also on the flank face of the insert a wear crater could be found. Within both wear craters, i.e. on the flank and on the rake face, pores where the cobalt binder was removed due to high temperatures and the consequently activated diffusion could be noticed (see Fig. 9f and c).

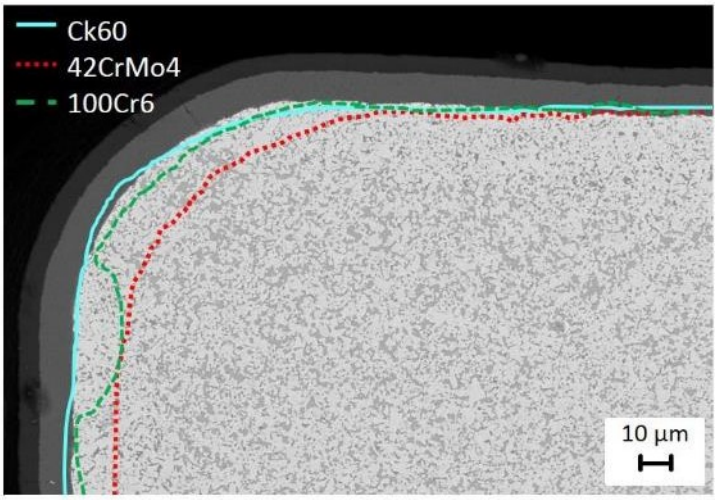

Fig. 10: SEM micrograph taken in backscattered electron mode of the cross-section of an unused cutting insert. The full, dotted and broken lines indicate the shape of the used inserts at the interface between cemented carbide and coating at the end of lifetime at v_c = 150 m/min.

For a more detailed evaluation of the plastic deformation due to turning, SEM images of an unused insert and the three inserts used for turning at a speed of 150 m/min until the end of tool life were recorded. A superposition of the profiles of the used inserts is presented in Fig. 10, evidencing that the insert after cutting the Ck60 only shows slight plastic deformation. For the 100Cr6, hardly any deformation could be found on the rake face, but the wear crater on the flank face already shown in Fig. 9f can be identified. The most pronounced deformation of the three tested inserts could be found for turning the 42CrMo4; there, the edge of the insert deviates by ~15 µm with respect to the unused insert. Further evidence of the occurring plastic deformation is derived from the surface area right before the wear crater develops. There, cracks within the coating and even a terraced surface of the cemented carbide insert, unambiguously visible in Fig. 11a, could be observed. At the trailing edge of the wear crater, no indications for such intense deformation are visible (see Fig. 11b).

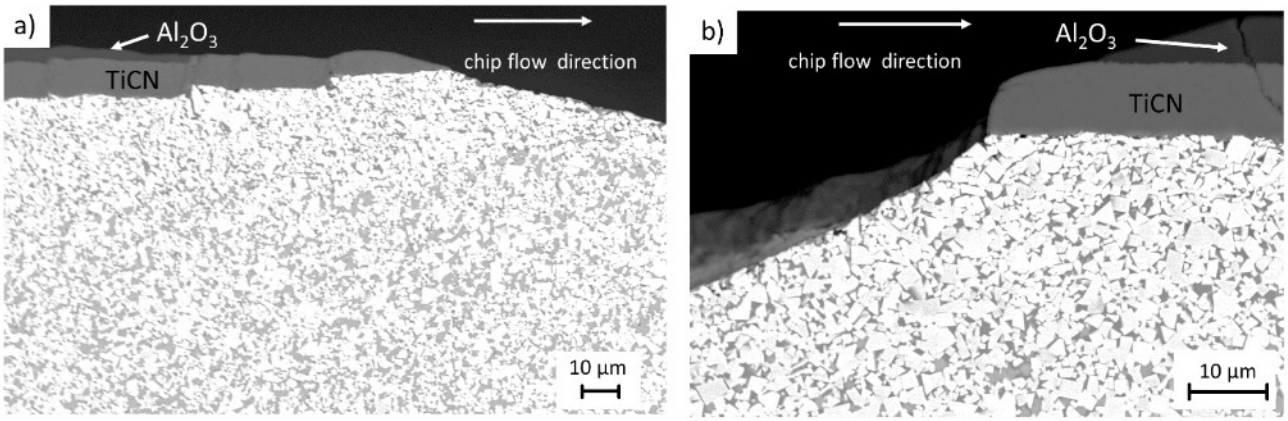

Fig. 11: SEM micrographs taken in backscattered electron mode of the cutting insert after turning of 42CrMo4 at v_c = 150 m/min at the end of lifetime. a) Rake face at the leading edge of the wear crater and b) trailing edge of the wear crater.

4. Discussion

Our investigations show that workpiece material as well as cutting speed considerably affect tool wear and lifetime. A correlation between cutting speed and tool life similar to Fig. 4was already found by Taylor [18]. There, a model that enables to calculate the optimized cutting speed for a certain cutting system based on the crater and flank wear occurring during turning tests was introduced for uncoated steel tools [19,20]. This model needs to be extended, since for coated cemented carbide cutting tools also feed rate and depth are of major impact, as stated by Astakhov et al. [21]. Furthermore, a rise of

temperature at the interface between cutting tool and workpiece material, when increasing the cutting speed, is documented in literature [22,23]. The investigations presented within this study were made under dry conditions; however, it has to be mentioned that the presence and the type of cutting fluid is also of valuable impact with respect to tool life [24], and consequently demands a further extension of the Taylor model [18]. Furthermore, a rise of temperature at the interface between cutting tool and workpiece material, when increasing the cutting speed, is documented in literature [22,23]. To minimize the effect of statistical variability on wear data, additionally turning test runs and observations of the inserts during different stages of tool life were carried out (see Fig. 7 obtained after 22 min of turning). Within this study both, the Ck60 and the 42CrMo4 are characterized by similar hardness and tensile strength; however, their turning results in remarkably different tool life, evidencing that not only the hardness of the workpiece material has a major impact on tool life. An unambiguous correlation of the microstructure (presented in Fig. 3) of the workpiece material to the wear progress could be observed. Workpiece materials like the investigated 42CrMo4 with a tempered martensitic microstructure and the characteristic high hardness and strength lead to a reduced cutting tool life during turning. Thus, the increased abrasive wear can be assumed to stem from the high mechanical and thermal stresses imposed onto the cutting insert during turning of such workpiece materials.

Workpiece materials like the Ck60 with a dominating pearlitic microstructure are known to have a less pronounced adhesion tendency compared to workpiece materials with a dominating ferritic microstructure like the 100Cr6. Furthermore, cutting of pearlitic steels has been reported to result in an increased temperature within the contact zone with respect to ferritic steels [25,26]. Thus, we can conclude that during cutting of Ck60 lower temperatures occur and less adhered material sticks to the tool surface, which improves the cutting performance at low cutting speeds (see Fig. 4a).

The soft annealed 100Cr6 features a ferritic microstructure with cementite spheroidites. The ferrite phase is on the one hand characterized by low hardness and strength, but on the other hand it has a high adhesion tendency to the surface of the cemented carbide inserts [25]. After cutting the 100Cr6, we observed a huge quantity of adhered workpiece material on the cutting edge prior to removal in the aqueous HCl solution. Such adhered material could lead to tearing of highly loaded coating fragments and promotes chipping of the cemented carbide insert at the flank face (see Figs. 8 and 9). This is comparable to the formation of build-up edges, where the workpiece material sticks on the

cutting tool and tears out. This interpretation also explains the observed comparable tool life of the ferrite-dominated 100Cr6 and the harder pearlite-dominated Ck60.

Further, the microstructure characteristics of steels can be modified by heat treatments such as annealing, aging, quenching and tempering [14]. Also the content of inclusions within the steel matrix has to be considered. For workpiece materials rich in nonmetallic inclusions, a reduction of flank and crater wear by a wear protective layer has been reported [11,14]. In addition, the type of inclusion has a major impact on abrasive wear and in consequence on tool life. For example, at typical cutting temperatures, MnS inclusions soften and have no impact on abrasive wear, which is in strong contrast to typical oxide inclusions [14]. Abrasive wear has been found to yield a major impact on the flank as well as on the rake face of the tool. On the tool flank, pronounced abrasive wear leads to a fast increase of flank wear (see Fig. 7) and thus to a decreased tool life. Further, the formation of a build-up layer on the flank face was not observed, which is in agreement with the available literature [27]. On the rake face, crater wear promoted by temperature-driven diffusion and further plastic deformation progresses quickly (see Figs. 6 and 7).

Due to its excellent thermal stability and low thermal conductivity and high hardness at elevated temperatures [15,28,29], deterioration of the α-Al_2O_3 top-layer during continuous turning is mainly controlled by abrasive and adhesive wear. No evidence of diffusion or even dissolution or chemical reaction between workpiece material and Al_2O_3 was reported so far [12,30]. It is more likely that the Al_2O_3 top-layer is worn by a discrete plastic deformation resulting in ductile fracture of the coating [31]. The influence of the crystallographic structure of the Al_2O_3 top-layer on the performance in turning was studied by Ruppi et al. [30]. Tests suggested that the best wear resistance was obtained when the (0001) planes were nearly parallel to the coating surface [30]. While bulk diffusion of workpiece elements or cobalt from the binder of the cemented carbide through the Al_2O_3 top-layer at the given cutting conditions is unlikely, surface diffusion of cobalt was suggested by Hörling et al. [32]. There, the cobalt diffuses out of the cemented carbide on positions where defects within the coating are present. Inserts coated with TiCN/α-Al_2O_3 by CVD show a typical network of thermally formed cracks. These cracks serve as diffusion paths and consequently foster diffusion wear and oxidation [6,33,34]. Generally, using these cracks as diffusion paths through the coating, the following phenomena are possible: *(i)* diffusion of Fe from the workpiece material into the cobalt binder phase and *(ii)* formation of Fe-Co mixed carbides either in the workpiece material or on the surface of the cutting insert. Further, also carbon diffusion from the steel workpiece material into the insert is

possible and results in the formation of Fe-W mixed carbides [19]. Evidence of diffusion between those areas of the cemented carbide, where the coating has worn through, and the workpiece material at cutting speeds of 200 m/min and higher was also reported in [13]. At the leading edge of the rake face (i.e., the position in chip flow direction where the wear crater initiates), the coating is worn through gradually (see Fig. 11a), whereas at the trailing edge (i.e., the end of the wear crater) coating fragments break away, as evidenced by Fig. 11b [16,31]. Once the coatings are worn through, the exposed cemented carbide surface is quickly covered by workpiece material and diffusion between adhered layers and cemented carbide occurs at the elevated contact temperatures. This phenomenon is valid for all cutting inserts, where the coatings are totally worn through, except for turning of 42CrMo4 at a cutting speed of 250 m/min. It can be assumed that with higher cutting speeds less time for the mentioned diffusion phenomena between chip and insert is available. Thus, with increasing cutting speed the wear crater is less pronounced (see Fig. 8). In the case of turning the 42CrMo4, even the TiCN coating is still intact on the rake face.

Plastic deformation of the cemented carbide is promoted by the high contact temperatures. Also workpiece rotation is promoting the increase of contact temperature and further plastic deformation; however, the applied coating is assumed to be able to accommodate plastic deformation without additional fracture [35]. Further, previously out-diffused cobalt binder would lead not only to plastic deformation, but also to fracture of the substrate. The highest temperatures have been reported for those areas on the flank and rake face, which are in direct contact to the workpiece material [6,16]. More extended hot areas have been observed for uncoated compared to coated tools, probably due to the missing thermal isolation by the Al_2O_3 top-layer and the increasing contact zone between chip and uncoated tool surface as a result of the progressing wear. Obviously, the high temperatures lead to softening of the cemented carbide, thus facilitating its plastic deformation [15]. Thus, we conclude that after removal of the thermally isolating and mechanically protecting Al_2O_3 top-layer during turning the temperature on the cemented carbide surface is raising considerably, which promotes cobalt diffusion and plastic deformation. The thermal cracks stemming from coating deposition and the consequently locally initiated wear can be assumed to also contribute to plastic deformation of the cemented carbide. This is clearly evidenced by the change of the radius of the cutting edge (see Fig. 10) and the terrace formation on the rake face at the leading edge of the wear crater (see Fig. 11a).

5. Conclusions

Within this work, turning tests with CVD TiCN/α-Al_2O_3 coated cemented carbide cutting inserts using three different steel workpiece materials (42CrMo4, Ck60 and 100Cr6) at three different cutting speeds (150, 200 and 250 m/min) were carried out. The major findings on the influence of cutting speed and workpiece material on wear mechanism and tool life can be summarized as follows:

- Influence of cutting speed: A decrease of tool life and removed workpiece volume with increasing cutting speed was observed. High cutting speeds reduce crater wear, while in contrast flank wear decreases for lower cutting speeds.
- Influence of workpiece material: Turning of different workpiece materials results in a varying tool life and in different wear pattern on rake and flank face. For all investigated workpiece materials, crater wear evolves with time. Further, the level of plastic deformation of the cutting inserts differs:
    - Turning of 42CrMo4 yields the most pronounced plastic deformation and shortest tool life.
    - Turning of Ck60 causes minor plastic deformation. Tool life lies between 42CrMo4 and 100Cr6 except for the lowest cutting speed, where tool life is comparable to 100Cr6.
    - Turning of 100Cr6 results again in minor plastic deformation but formation of a wear crater on the flank face. The two highest cutting speeds yield the longest tool life observed within this study.

In conclusion, the demonstrated extension of our knowledge of wear mechanisms during cutting by further parameter variations could in the future lead to optimized wear behavior and improved tool performance.

6. Acknowledgements

Financial support of the Österreichische Forschungsförderungsgesellschaft FFG (grant number 851894) is gratefully acknowledged.

7. References

[1] J. Garcia, R. Pitonak, The role of cemented carbide functionally graded outer-layers on the wear performance of coated cutting tools, Int. J. Refract. Met. Hard Mater. 36 (2013) 52–59.

[2] U. Schleinkofer, C. Czettl, C. Michotte, Coating Applications for Cutting Tools, in: V.K. Sarin (Ed.), Compr. Hard Mater., Elsevier, Oxford, 2014: pp. 453–469.

[3] S. Ruppi, Advances in chemically vapour deposited wear resistant coatings, J. Phys. IV. 11 (2001) 847–859.

[4] C. Mitterer, PVD and CVD Hard Coatings, in: V.K. Sarin (Ed.), Compr. Hard Mater., Elsevier, Oxford, 2014: pp. 449–467.

[5] S. Ruppi, Deposition, microstructure and properties of texture-controlled CVD α-Al_2O_3 coatings, Int. J. Refract. Met. Hard Mater. 23 (2005) 306–316.

[6] M. Tkadletz, J. Keckes, N. Schalk, I. Krajinovic, M. Burghammer, C. Czettl, et al., Residual stress gradients in α-Al_2O_3 hard coatings determined by pencil-beam X-ray nanodiffraction: The influence of blasting media, Surf. Coat. Technol. 262 (2015) 134–140.

[7] N. Schalk, C. Mitterer, C. Czettl, B. Sartory, M. Penoy, C. Michotte, Dry-blasting of α- and κ-Al_2O_3 CVD hard coatings: Friction behaviour and thermal stress relaxation, Tribol. Lett. 52 (2013) 147–154.

[8] H. Holzschuh, M. Klaus, C. Genzel, Influence of the residual stress state on the toughness of CVD - Coated cemented carbide cutting tools, in: Adv. Powder Metall. Part. Mater. Mater. PowderMet 2008, Washington D.C., 2008: p. 100

[9] W. Lengauer, K. Dreyer, Tailoring hardness and toughness gradients in functional gradient hardmetals (FGHMs), Int. J. Refract. Met. Hard Mater. 24 (2006) 155–161.

[10] W. Schedler, Hartmetall für den Praktiker, VDI-Verlag GmbH, Düsseldorf, 1988.

[11] A. Nordgren, A. Melander, Deformation behaviour of different types of inclusion during chip formation turning of quenced and tempered steels, Mater. Sci. Technol. 5 (1989) 940–951.

[12] S. Ruppi, B. Högrelius, M. Huhtiranta, Wear characteristics of TiC, Ti(C,N), TiN and Al_2O_3 coatings in the turning of conventional and Ca-treated steels, Int. J. Refract. Metals Hard Mater. 16 (1998) 353–368.

[13] M. Nouari, A. Molinari, Experimental verification of a diffusion tool wear model using a 42CrMo4 steel with an uncoated cemented tungsten carbide at various cutting speeds, Wear. 259 (2005) 1151–1159.

[14] N. Ånmark, A. Karasev, P.G. Jönsson, The Influence of Microstructure and Non-Metallic Inclusions on the Machinability of Clean Steels, Steel Res. Int. 88 (2016) 1–8.

[15] I. Krajinovic, W. Daves, M. Tkadletz, T. Teppernegg, T. Klünsner, N. Schalk, et al., Finite element study of the influence of hard coatings on hard metal tool loading during milling, Surf. Coat. Technol. 304 (2016) 134–141.

[16] P.A. Dearnley, E.M. Trent, Wear mechanisms of coated carbide tools, Mater. Technol. 9 (1982) 60–75.

[17] S. Ruppi, Texture-hardened α-alumina coated tool, EP 1 953 258 A1, 2008.

[18] F.W. Taylor, On the art of cutting Metals, The American Society of mechanical engineers, New York, 1906.

[19] H.K. Tönsdorff, Spanen, Springer-Verlag, 1995.

[20] R. Storf, Drehen: Grundlagen und Anwendungstechnik, VDI-Verlag GmbH, 1987.

[21] V.P. Astakhov, J.P. Davim, Tools (Geometry and Material) and Tool Wear, in: Mach. Fundam. Recent Adv., 2008: p. 362.

[22] W. Grzesik, Experimental investigation of the cutting temperature when turning with coated indexable inserts, Int. J. Mach. Tools Manuf. 39 (1999) 355–369.

[23] W. Grzesik, M. Bartoszuk, P. Nieslony, Finite element modelling of temperature distribution in the cutting zone in turning processes with differently coated tools, J. Mater. Process. Technol. 164–165 (2005) 1204–1211.

[24] D.A. Axinte, W. Belluco, L. De Chiffre, Reliable tool life measurements in turning - an application to cutting fluid efficiency evaluation, Int. J. Mach. Tools Manuf. 41 (2001) 1003–1014.

[25] G. Vieregge, Zerspanung der Eisenwerkstoffe, Verlag Stahleisen m.b.H., Düsseldorf, 1959.

[26] F. Klocke, K. Gerschwiler, Zerspanen von Stahl, Stahl-Informations-Zentrum. (2008).

[27] A. Larsson, S. Ruppi, Structure and composition of built-up layers on coated tools during turning of Ca-treated steel, Mater. Sci. Eng. A. 313 (2001) 160–169.

[28] D.G. Cahill, S.-M. Lee, Thermal conductivity of κ-Al_2O_3 and α-Al_2O_3 wear-resistant coatings, J. Appl. Phys. 83 (1998) 5783–5786.

[29] M. Rebelo De Figueiredo, J. Neidhardt, R. Franz, C. Mitterer, Low-friction mechanisms active for carbon containing coatings: Ti-C-N as a model system, Berg- und Hüttenmännische Monatshefte. 153 (2008) 263–267.

[30] S. Ruppi, Enhanced performance of α-Al_2O_3 coatings by control of crystal orientation, Surf. Coat. Technol. 202 (2008) 4257–4269.

[31] P.A. Dearnley, Rake and flank wear mechanisms of coated and uncoated cemented carbides, Surf. Eng. 1 (1985) 43–58.

[32] A. Hörling, L. Hultman, M. Odén, J. Sjölén, L. Karlsson, Thermal stability of arc evaporated high aluminum-content $Ti_{1-x}Al_xN$ thin films, J. Vac. Sci. Technol. A. 20 (2002) 1815.

[33] D. Hochauer, C. Mitterer, M. Penoy, S. Puchner, C. Michotte, H.P. Martinz, et al., Carbon doped α-Al_2O_3 coatings grown by chemical vapor deposition, Surf. Coat. Technol. 206 (2012) 4771–4777.

[34] X. Chen, H. Liu, Q. Guo, S. Sun, Oxidation behavior of WC-Co hard metal with designed multilayer coatings by CVD, Int. J. Refract. Met. Hard Mater. 31 (2012) 171–178.

[35] P.A. Dearnley, Introduction to Surface Engenieering, Cambridge University Press, Cambridge, 2017.